ANGULAR TRAPPING OF A MIRROR USING RADIATION PRESSURE

By

David B. Kelley

B.S. Massachusetts Institute of Technology, Cambridge, MA, 2010
M.S. Syracuse University, Syracuse, NY, 2013

Dissertation
Submitted in Partial Fulfillment of the Requirements
for the degree of
Doctor of Philosophy in Physics

Syracuse University
September 2015

ANGULAR TRAPPING OF A MIRROR USING RADIATION PRESSURE

By

David B. Kelley

B.S. Massachusetts Institute of Technology, Cambridge, MA, 2010
M.S. Syracuse University, Syracuse, NY, 2013

Dissertation
Submitted in Partial Fulfillment of the Requirements
for the degree of
Doctor of Philosophy in Physics

Syracuse University
September 2015

Approved : _____
Prof. Stefan Ballmer

Date : _____

ABSTRACT

Alignment control in gravitational-wave detectors has consistently proven to be a difficult problem due to the stringent noise contamination requirement for the gravitational wave readout and the radiation-pressure induced angular instability in Fabry-Perot cavities (Sidles-Sigg instability). I present the development, implementation, and measurement of a dual-carrier control scheme which uses radiation pressure to control a suspended mirror, trapping it in the longitudinal degree of freedom and one angular degree of freedom.

Contents

List of Tables

List of Figures

Preface

The work presented in this thesis stems from my participation in the LIGO Scientific Collaboration (LSC). This work does not reflect the scientific opinion of the LSC and it was not reviewed by the collaboration.

The theory of optical trapping in two degrees of freedom in chapter 2 is based on

A. Perreca *et al.*, "Multi-dimensional optical trapping of a mirror," *Phys. Rev. D* **89** (2014) 122002.

Chapter 5 is based on material from

D. Kelley *et al.*, "Observation of photo-thermal feed-back in a stable dual-carrier optical spring," *Phys. Rev. D* **92** (2014) 062003.

Chapter 6 is based on

D. Kelley *et al.*, "Angular Trap Demonstration," to be submitted to *Phys. Rev. D*

Acknowledgments

Thank you for the music.....

to

my parents and Emma

Chapter 1

Introduction

The Advanced Laser Interferometer Gravitational-Wave Observatory (aLIGO) is part of an international effort to detect gravitational waves. The search will resume later this year with the two aLIGO sites in Washington and Louisiana, which will ramp up to full design sensitivity over the following few years.

1.1 Basic layout of aLIGO

In its simplest form, aLIGO is a Michelson interferometer with Fabry-Pérot cavities for arms (see figure 1). In each Fabry-Pérot cavity, the mirror closer to the Michelson beam splitter is called the input test mass (ITM) and the other mirror is called end test mass (ETM).

When a gravitational wave passes through the detector, it causes changes in the distance between the ETM and ITM in each cavity. Because the wave is quadrapolar, the changes in the x direction will have the opposite sign of the changes in the y direction. This causes a relative phase shift in each of the arms in opposite directions. When they recombine at the beam splitter, the phase shifts cause changes in the interference between the two beams, changing the amount of power at the the output port. We can detect these power fluctuations to reconstruct the phase shift and thus the strain, $h = \Delta L/L$ experienced by the interferometer due to the gravitational wave. We then use techniques like matched filtering to compare the strain signal from the interferometer to models of expected signals to search for events hidden in the noise background of the interferometer.

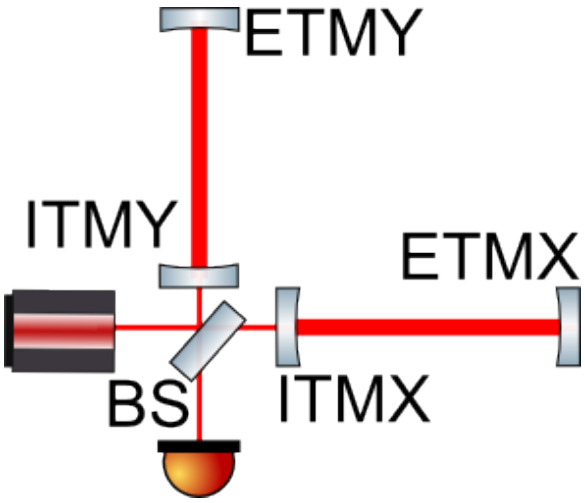

Figure 1 : In its simplest form, aLIGO is a Michelson interferometer with Fabry-Pérot cavities for arms. Light from the laser is split by the beam splitter (BS), then enters the arm cavities through the input test masses (ITMX and ITMY). Power builds up in the cavity between input and end test masses (ETMX and ETMY). When a gravitational wave passes through the detector, it shifts the phases of light in the two arms in opposite directions. Because the cavity is over-coupled ($r_{ITM} < r_{ETM}$), light leaves the arm cavities and goes back to the BS. The phase-shifted light from the two cavities interferes at the BS, producing the error signal that we measure with a photodiode.

With the goal of suppressing the noise and improving the signal, many changes have been made to the initial simple interferometer. The masses have been upgraded to 40 Kg and suspended from quadruple pendulum systems to reduce seismic noise. Mirrors have been installed for power and signal recycling to maximize the laser power in the arms. This has already led us to an increase in range by a factor of almost 3. In addition, aLIGO plans to upgrade the current input laser power from 25 watts to 125 watts, which should bring the final range of the detectors over 200 MPc.

However, an increase in laser power includes several challenges. One such effect that will scale with power is the Sidles-Sigg instability. In simple terms, the Sidles-Sigg instability comes from angular or spot location displacements that cause torques on the mirrors and gets stronger as the intra-cavity power increases. One mode is called the "Hard mode" and the other is called the "soft" mode. They are described in more detail in Chapter 7. This effect must be dealt with by using active controls on the angular degrees of freedom of the test masses.

We want to develop a method to control the angular motion and damp the Sidles-Sigg instability of the ITMs and ETMs as we increase the laser power. We know

that increasing the gain of the current angular control system will result in more sensing noise being injected into the system, which may limit the sensitivity of the instrument. We think that optical springs can offer a robust control system that is not subject to sensing noise, which would be a very good solution.

1.2 Optical Springs

Optical spring is a term used to describe the linear region of the interaction between cavity length and radiation pressure force in a detuned Fabry-Pérot cavity.

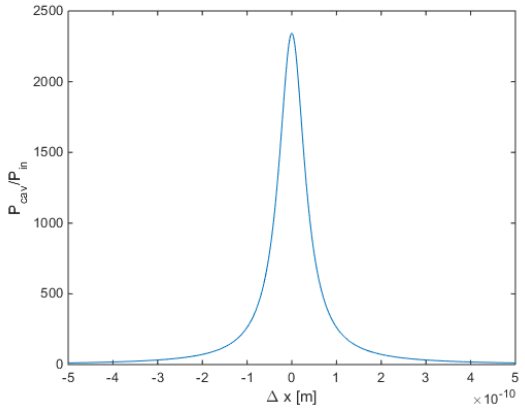

Figure 2 : Optical power in a critically coupled cavity near resonance. The height of the peak is determined by the reflectivities of the two mirrors and the

Radiation pressure force is given by

$$F = \frac{P_{cav}}{2c} \tag{1.1}$$

In a cavity sweeping position, we expect the cavity power P_{cav} to follow (see figure 2):

$$P_{cav} = P_{in} \left| \frac{t_1}{1 - r_1 r_2 e^{\frac{-4i\pi\Delta x}{\lambda}}} \right|^2 \tag{1.2}$$

Where t_1 and r_1 are the amplitude transmisivity and reflectivity of the input mirror and r_2 is the reflectivity of the end mirror. λ is the wavelength and Δx is the displacement from the cavity resonance.

We can see that there are approximately linear regions on both sides of resonance. This is the basis of a pragmatic explanation of optical spring behavior, demonstrated in figure 3. In this demonstration, we see the effects of "red" and "blue" detuning, where the cavity resonant length is longer and shorter, respectively, than cavity itself. The color association of these detunings comes from the laser frequency shift that could accomplish this detuning: red is a negative frequency detuning and blue is a positive frequency detuning.

In figure 3, we explore four different situations. For each one, I have drawn the resonant power (radiation pressure force) buildup in the cavity as a function of position. I have also shown an effectively static force due to a mechanical spring. It is important to note that we treat this as constant over position and time scales that we are dealing with.

In the first case, we address a red-detuned cavity in the adiabatic, or essentially stationary, case. As the mirror moves away from its equilibrium point, it experiences more force in the direction of displacement. In the blue-detuned case, we see that the net force is pushing the mirror back to its equilibrium position. Thus the red-detuned cavity is statically unstable, while the blue-detuned cavity is statically stable.

In the other case, we address a mirror that is in motion. This cavity will experience the radiation pressure force due to the position of the mirror in the recent past, determined by light storage time. In the red-detuned case, we see that the time-delayed force has an overall damping effect on the motion of the mirror. In the blue-detuned case, we get the opposite, anti-damping behavior.

In summary, we see that a blue-detuned cavity is statically stable and dynamically unstable, while a red-detuned cavity is statically unstable and dynamically stable.

We can describe an optical spring as having a spring constant that follows Hook's law ($F = -kx$) in this case, we treat damping as an imaginary component to the spring constant. Thus, a blue-detuned optical spring has a positive real part and a negative imaginary part, while a red-detuned optical spring has a negative real part and a positive imaginary part. However, since these optical springs behave like normal springs, you can add the spring constants of two of them together to arrive at a stable spring (see figure 4).

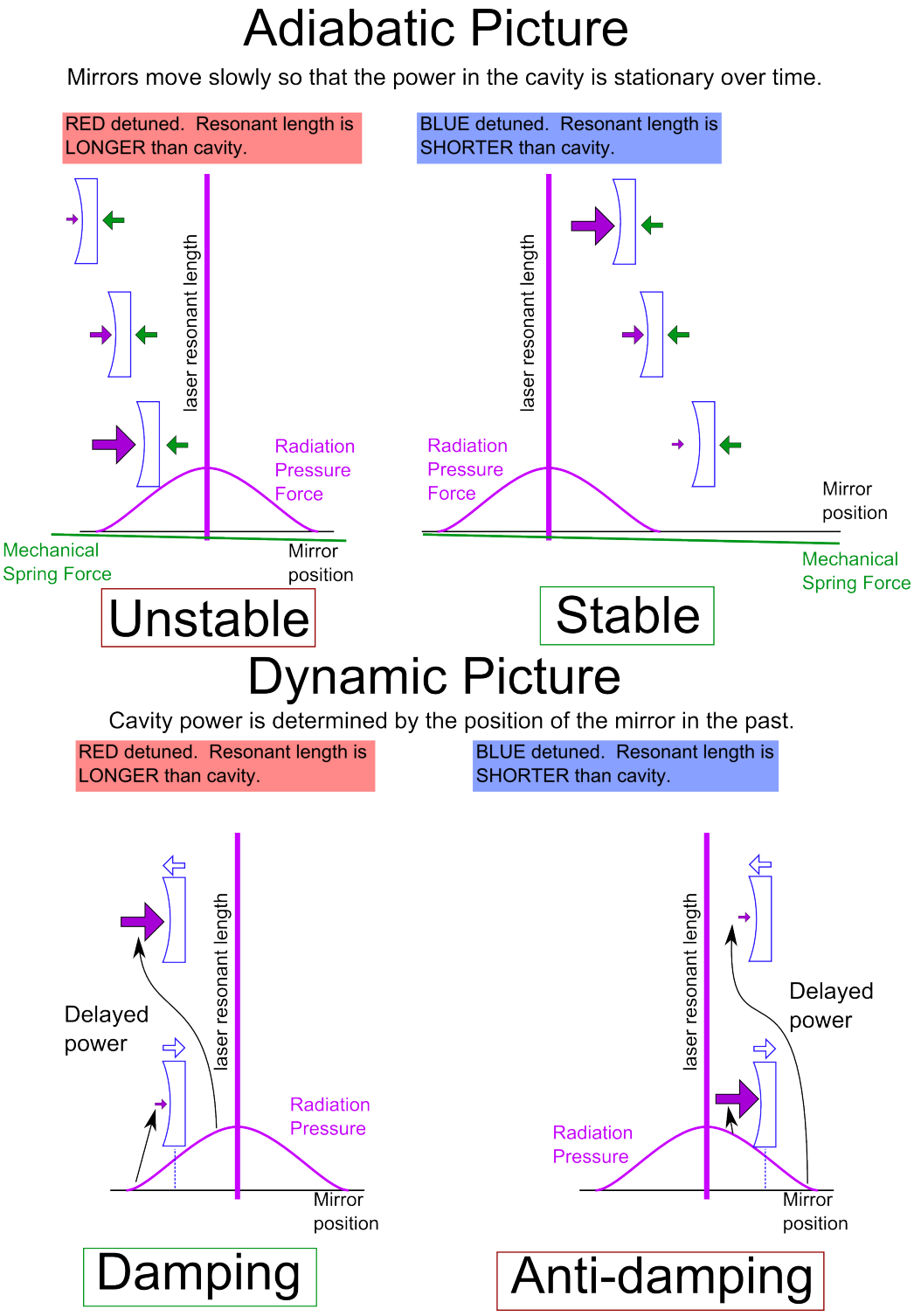

Figure 3 : Stability behavior of detuned cavities (optical springs). It is important to note that we rely on a constant force exerted on the mirror to choose the equilibrium point of the optical spring.

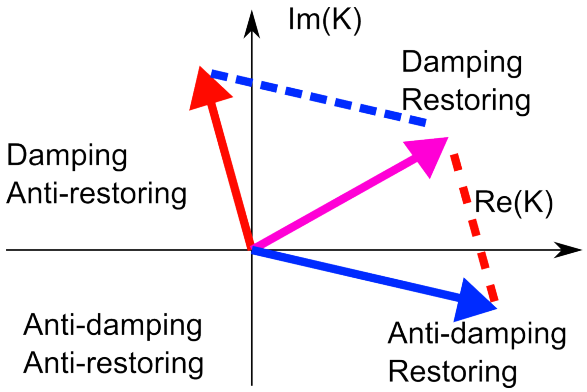

Figure 4 : We can add two unstable optical springs to make a system that is statically and dynamically stable. Note: this picture only makes sense in the low-frequency regime.

1.3 Summary

In the rest of this thesis, we will discuss the implementation and use of optical spring systems to investigate and control optomechanical systems. Chapter 3 discusses the suspensions and control loops required to isolate, reposition, and damp the optics. Chapter 4 covers the feedback systems used to generate the frequency-detuned beam and lock the optical spring cavities. Chapter 5 details the single-dimensional trap and the measurement of the photo-thermal effect. Chapter 6 demonstrates the angular trap.

1.4 Goal

We seek to demonstrate Angular damping using optical springs.

Chapter 2

Theory (from Perreca 2014)

2.1 Introduction

The Laser Interferometer Gravitational-Wave Observatory (LIGO) is part of a worldwide effort to detect gravitational waves and use them to study the Universe [1]. Construction of LIGO's advanced detectors is underway. The installation is expected to finish in 2014. The goal of Advanced LIGO (aLIGO) is the first direct detection of gravitational waves from astrophysical sources such as coalescing compact binaries and core-collapse supernovae. These detections will open a new spectrum for observing the Universe and establish the field of gravitational-wave astronomy. These initial observations will also show the potential science gain of further increasing the state-of-the-art sensitivity of gravitational-wave detectors [2, 3, 4]. Such detectors operate near the standard quantum limit, meaning that the contributions from quantum radiation pressure and shot noise are about equal in the observation band [5, 6].

To design a successor to aLIGO, techniques to operate gravitational-wave interferometers below the standard quantum limit need to be developed [7, 8]. Dual carrier control systems and angular control using stable optical springs are promising methods for evading quantum-mechanical limitations on detector sensitivity [9, 10, 11, 12, 13, 14]. In 2007 Corbitt *et al.* at the LIGO Laboratory at the Massachusetts Institute of Technology demonstrated a one-dimensional optical trap of a one gram mirror using a novel two-carrier scheme [15]. Their work clearly demonstrated the potential of this technique. Extended to angular degrees of freedom, it has the prospect of opening a completely new approach to the angular control problem in future generation

gravitational-wave detectors [16]. Sidles and Sigg have shown that, for a Fabry-Perot cavity with a single resonating laser field, the radiation pressure force will couple the two end mirrors, always creating one soft (unstable) and one hard (stable) mode [17]. This sets a lower limit on the required angular control bandwidth, which inevitably results in higher noise contamination by angular control noise and limits the angular control performance in the first and second generation gravitational-wave interferometers [9, 18, 19, 20]. As we will show in Sec. 2.4, angular optical trapping can bypass the Sidles-Sigg instability. Its fundamental noise limit is quantum radiation pressure noise. By design it is not affected by sensing noise, making it a promising candidate for low-noise angular control. Additionally, optical trapping can be used to cool a mechanical degree of freedom. Radiation pressure-based cooling is the preferred approach for cooling to the quantum ground state in the limit where the cavity line width is smaller than the mechanical frequency (good cavity limit)[21]. It can enable the manipulation of a macroscopic object at the quantum level [22, 23, 24, 25, 26]. However reaching the quantum ground state requires reducing the total rms motion, rather than the spectral density in the frequency band above the mechanical suspension resonance, as desired for a low-noise angular control system. We therefore will not further explore reaching the quantum ground state.

In this paper we present a prototype of a position and yaw optical trap for a suspended test mirror using a double dual-carrier control scheme. With mechanical suspension frequencies around 1 Hz such a system is, in virtually all cases, in the bad cavity limit; i.e., the cavity line widths are larger than the mechanical frequencies. We propose a system with two longitudinal traps acting on different spots of a single mirror; together, these traps will constrain both the position degree of freedom and one angular degree of freedom of the mirror. This essentially replaces the current magnetic drives with optical traps. The idea is promising and will be easy to apply to the other angular degree of freedom. The model includes two optical cavities with the trapped end-mirror in common. Each cavity is illuminated with two overlapping laser beams at different frequency detunings: one is positive detuned (blue detuning) and the other is negative detuned (red detuning). The two dual beams form two statically and dynamically stable optical springs with different lever arms and different power, designed such that the static (commonly named DC) radiation pressure torques of the two dual beams cancel each other while DC radiation pressure force is canceled

by displacing the position pendulum.

As a result, by picking the right parameters, we can obtain a system that is stable in the longitudinal and angular degrees of freedom with a mirror displacement range of the order of picometers.

The outline of this paper is as follows. In Sec. 2.2 we review the idea of an optical spring. We then couple optical springs to a mechanical system and analyze the stability of the resulting optomechanical system. Section 2.3 extends the stability analysis to more than one dimension. In Sec. 2.4 we show that such a two-dimensional optical spring is necessarily stronger than the Sidles-Sigg instability. In Sec. 2.5 we calculate the radiation pressure noise, which is the fundamental limiting noise for radiation pressure control. Finally, in Appendix 2.7, we derive the approximation-free expression for the optical spring in a Fabry-Perot cavity, which to our knowledge has not been published yet.

2.2 Stability principle

An optically detuned Fabry-Perot cavity naturally leads to a linear coupling between intracavity power and mirror position. Depending on the sign of the detuning, this coupling creates an optical spring which is either statically stable or unstable. Due to the time delay in the optical field build-up, the optical spring restoration force is slightly delayed. This leads to a dynamically unstable spring for the statically stable case and a dynamically stable spring for the statically unstable case. Corbitt *et al.* [15] demonstrated that by adding a second, frequency-shifted optical field (subcarrier) with a different detuning and power, a statically and dynamically stable optical spring can be achieved. The dual-carrier scheme has been used to optically trap a gram-scale mirror, controlling its longitudinal degree of freedom. Moreover, the damping of the optical spring can be controlled by adjusting the detuning of both carrier and subcarrier and their relative amplitudes. This naturally allows for efficient cooling of the degree of freedom seen by the optical spring. In contrast to a mechanical spring, this damping does not introduce intrinsic losses, and thus does not contribute to the thermal noise.

This technique can be extended to alignment degrees of freedom. By duplicating the Corbitt *et al.* approach for trapping with a second, different, optical axis and

a different beam spot on the controlled mirror, it is possible to control the angular degree of freedom with radiation pressure alone.

To be able to understand the stability of multidimensional optomechanical systems, we first recall the simple driven damped mechanical oscillator. From there we will stepwise increase the complexity by adding optical springs and additional degrees of freedom.

2.2.1 Damped mechanical oscillator stability

Although the damped mechanical oscillator is a well known system, we will take it as a starting point to make the reading clearer. Our goal is to describe the mechanical oscillator in the language of control theory, which allows us to understand the stability of the system from a different point of view. This approach can then be naturally extended to include the effect of additional optical springs.

The motion of a harmonic oscillator of mass m, spring constant k_m and velocity damping b, driven by the external force F_{ext}, can be expressed as [27]

$$m\ddot{x} = -k_m x - b\dot{x} + F_{ext} \tag{2.1}$$

where b is also called the viscosity coefficient. Often the damping rate $\Gamma = b/(2m)$ is used instead. Traditionally the Eq. (2.1) is directly used to get the system's position response x when applying the external force F_{ext}. The resulting transfer function is

$$G = \frac{x}{F_{ext}} = \frac{1}{-m\Omega^2 + k_m + ib\Omega} \tag{2.2}$$

where Ω is the angular frequency of the motion.

Alternatively we can describe a damped mechanical oscillator as a feedback system, with the plant being just a free test mass described by the transfer function $M = x/F_{ext} = -1/m\Omega^2$, obtained directly from the equation of motion of a free test mass. The control filter of the feedback loop is the mechanical spring, which takes the mass displacement x as input and acts on the plant with the control signal, or force, F_K, which is subtracted from the external force F_{ext}. The transfer function of the control filter is $K_M = F_K/x = k_m + ib\Omega$. In this picture we can now calculate the closed loop transfer function and obtain the same expression as in Eq. (2.2),

$$G = \frac{M}{1 + K_M M} = \frac{1}{-m\Omega^2 + k_m + ib\Omega} \tag{2.3}$$

where $OL_M = -K_M M = (k_m + ib\Omega)/m\Omega^2$ describes the open loop transfer function of the system.

Stability

We can now check for the stability of the system in both pictures. We recall from literature that the stability of a system described by its transfer function G can be evaluated looking at the poles of its transfer function in the s-plane ($s = i\Omega$) [28]. In particular a system is stable only if its transfer function's poles have a negative real part, and the multiplicity of poles on the imaginary axis is at most 1. The transfer function in Eq. (2.2) has the following poles:

$$i\Omega = -\frac{b}{2m} \pm \sqrt{\frac{b^2}{4m^2} - \omega_0^2}, \tag{2.4}$$

where $\omega_0^2 = k_m/m$ is the resonant frequency of the pendulum. The value of the damping rate $\Gamma = b/2m$ compared to ω_0 determines whether the system is overdamped, underdamped or critically-damped. But since Γ (or b) is always positive, the real part of the poles is always negative. The system is thus always stable.

From the control theory point of view, the stability can also be evaluated with no loss of generality by considering the open loop transfer function $OL_M = (k_m + ib\Omega)/m\Omega^2$ and applying, for example, the Bode stability criterion [29]. The positivity of b guarantees an always positive phase margin and therefore stability. In the reminder of this work, for simplicity, we will test the stability of the control scheme using the Bode graphical method.

2.2.2 Optical spring: A classical model

Next, we look at an optical spring. We start with a Fabry-Perot cavity of length L_0, frequency detuning δ (rad/Hz), amplitude transmittance coefficients t_1, t_2 and amplitude reflectance coefficients r_1, r_2 of the input and output cavity mirror respectively. The light field inside the cavity builds up and exerts a radiation pressure force on both mirrors.

We define the propagator $X = r_1 r_2 e^{-2i\delta\tau}$ and phase factor $Y = e^{-i\Omega\tau}$, with $\tau = L_0/c$ the one-way travel time of the photon inside the cavity, k is the wave vector of the light field and Ω is the mechanical frequency of the pendulum. From this we

can obtain an elastic force-law for small displacement values x, but potentially large detuning from resonance:

$$F_{rad} = F_0 - K_{OS} \cdot x + O(x^2), \tag{2.5}$$

where

$$K_{OS} = K_0 \left[\frac{Y^2}{(1 - Y^2 X)(1 - Y^2 \overline{X})} \right] \tag{2.6}$$

is the optical spring constant and $\overline{X}$ is the complex conjugate of X. Here K_0 is the (mechanical) frequency-independent part of the spring constant:

$$\begin{aligned} K_0 &= F_0 \cdot 2ik \cdot (X - \overline{X}), \quad \text{with} \\ F_0 &= P_0 \cdot \frac{2r_2^2}{c} \cdot \frac{t_1^2}{(1 - X)(1 - \overline{X})} \end{aligned} \tag{2.7}$$

The expression in Eqs. (2.6) and (2.7) is the general expression for K_{OS} up to linear order in x. While approximations for this formula have been published before [30], we are not aware of a previous publication providing the full expression. We address the complete derivation of the optical spring constant K_{OS} in Appendix 2.7. There we also show that with the approximations $2\Omega\tau \ll 1$ and $2\delta\tau \ll 1$ Eq. (2.6) is equivalent to the expressions already existing in literature [30, 15].

We note that K_0 is a real number. Its sign is determined by the imaginary part of X. A positive sign is associated with positive detuning ($\delta > 0$) and a restoring force (statically stable), while a negative sign is due to negative detuning ($\delta < 0$) and leads to a antirestoring force (statically unstable). Also, for small (positive) frequencies $\Omega\tau \ll 1$, the sign of the imaginary part of Eq. (2.6) is opposite to its real part, leading to positive dynamic feedback for the statically stable case and negative dynamic feedback for the statically unstable case.

Our next step is to couple the optical spring to a mechanical pendulum. We can treat this as either a damped mechanical oscillator with transfer function G, controlled by an optical spring K_{OS}, or as a free mass with transfer function M, controlled by the total feedback filter $H = K_M + K_{OS}$, see Fig. 5. In both cases we obtain the same closed-loop transfer function, equivalent to the one we would have obtained by rewriting the equation of motion of a damped mechanical oscillator with an optical

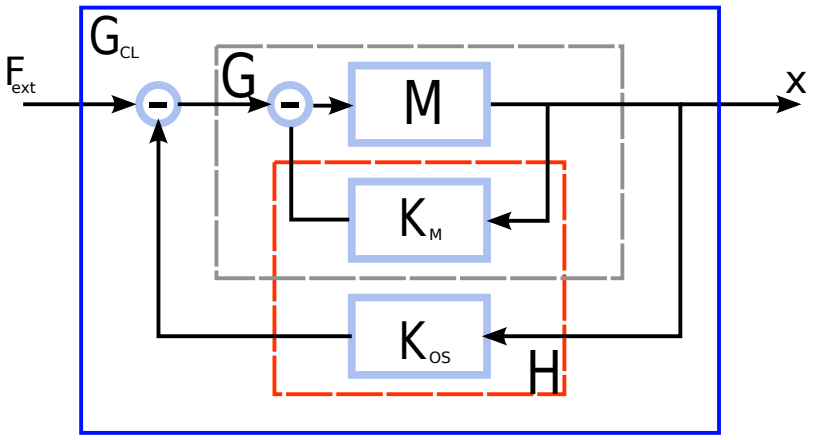

Figure 5 : Mechanical oscillator and feedback systems. The mechanical oscillator can be seen as plant (G) and the optical spring K_{OS} as feedback or alternatively as free test mass (plant M) and $H = K_{OS} + K_M$ as feedback. Both the cases lead to the same closed loop transfer function G_{CL} which describes the system as a damped mechanical oscillator in the presence of the optical spring, which is subjected to the external force F_{ext} and has the corresponding displacement x as output.

spring:

$$G_{CL} = \frac{x}{F_{ext}} = \frac{G}{1 + K_{OS}G} = \frac{M}{1 + HM} = \frac{1}{-m\Omega^2 + K_M + K_{OS}} \tag{2.8}$$

The stability of the total system can again be evaluated by either looking at the poles of the closed-loop transfer function G_{CL}, or looking at the gain and phase margin of the open loop transfer function $OL_{MH} = -H/m\Omega^2$. The latter is generally more convenient. Unless compensated by large mechanical dissipation in K_M, the positive dynamic feedback for the statically stable case ($\delta > 0$) leads to a dynamically unstable system. Intuitively this can be understood as a phase delay in the radiation pressure build-up which is caused by the cavity storage time. For $\delta < 0$ the system is statically unstable.

2.2.3 Double carrier spring

The seemingly intrinsic instability of optical springs can be overcome by a scheme proposed by Corbitt *et al.* [15]. The carrier is set at a large positive detuning ($\delta > 0$, large $|\delta|/\gamma$, where γ is the line width). This provides a static restoring force, together with a relatively small dynamic instability (antidamping). Then a subcarrier is added

at lower power and with a small negative detuning ($\delta < 0$, small $|\delta|/\gamma$). The subcarrier adds sufficient damping to stabilize the total optical spring, while leaving the sign of the static restoring force unchanged. For appropriately chosen parameters of carrier (c) and subcarrier (sc) (power P_0^c and P_0^{sc}, detuning δ_c and δ_{sc}) the resulting total system thus becomes stable.

The spring constant of the total optical spring is simply the sum of the individual spring constants of the carrier and subcarrier

$$K_{OS} = K_{OS}^c + K_{OS}^{sc} \tag{2.9}$$

where the individual springs K_{OS}^c and K_{OS}^{sc} are given by Eq. (2.8).

Conceptually we can think of the dual-carrier optical spring as a physical implementation of a feedback control filter for the mechanical system. With this tool at hand, we can start to analyze the behavior and stability of higher-dimensional mechanical systems in the next section.

2.3 Control model of longitudinal and angular degrees of freedom

We will now extend our analysis to additional degrees of freedom. Experimentally, a torsion pendulum suspension is easy to build. Therefore we will focus our attention to controlling the yaw motion of a test mirror, keeping in mind that the method can be applied to any additional degree of freedom. For actively controlling two degrees of freedom (length and yaw), we need a two-dimensional control system. In other words, we will need a second dual-carrier optical spring in a setup that for example looks like Fig. 6. We will label the two dual-carrier optical fields as beams A and B. Each beam includes a carrier and a subcarrier field, i.e.

$$\begin{aligned} \text{beam } A &= \text{carrier } A + \text{subcarrier } A \\ \text{beam } B &= \text{carrier } B + \text{subcarrier } B \end{aligned} \tag{2.10}$$

The two beams have a different optical axis, and each has its own optical spring constant, K_{OS}^A and K_{OS}^B, given by Eq. (2.9).

If we define x_A and x_B as the longitudinal displacement of the mirror at the contact points of beam A and beam B on the test mirror, and F_A and F_B as the

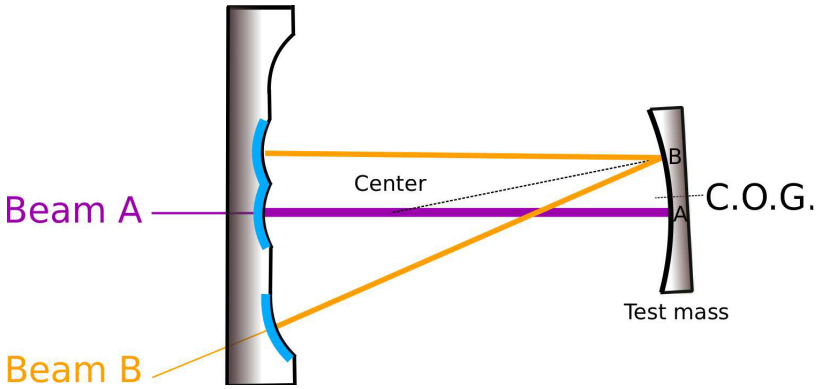

Figure 6 : In this sketch the main purple (beam A) optical axis hits the test mirror at point A, slightly displaced from the center of gravity (C.O.G.), such that it still corresponds mainly to the length degree of freedom. Thus the second orange (beam B) optical axis, which hits the test mirror closer to the edge at point B, needs much less power to balance the total DC torque. In our test setup the large input coupler is a composite mirror. It is 600 times more massive than the small mirror. The choice of a V-shaped beam B results in a more practical spot separation on the input coupler.

corresponding exerted forces, we can describe the mechanical system with a plant matrix M:

$$\begin{pmatrix} x_A \\ x_B \end{pmatrix} = M \begin{pmatrix} F_A \\ F_B \end{pmatrix} \tag{2.11}$$

The explicit expression for M for a torsion pendulum is given in Appendix 2.8.

The control is provided by the optical springs. In the x_A-x_B basis the control matrix H is diagonal and given by (also see Fig. 7)

$$\begin{pmatrix} F_A \\ F_B \end{pmatrix} = H \begin{pmatrix} x_A \\ x_B \end{pmatrix} = \begin{pmatrix} K_{OS}^A & 0 \\ 0 & K_{OS}^B \end{pmatrix} \begin{pmatrix} x_A \\ x_B \end{pmatrix} \tag{2.12}$$

For a multidimensional feedback system to be stable, it is sufficient that each individual (one-dimensional) feedback loop is stable, assuming all remaining control loops are closed. In other words, in our two-dimensional optomechanical system, we close the beam B control filter for evaluating the open loop transfer functions OL_A, and vice versa. For the open loop transfer functions OL_A and OL_B we then find:

$$\begin{aligned} OL_A &= e_A^T \left(\mathbb{1} + HM(\mathbb{1} - e_A e_A^T)\right)^{-1} HMe_A \\ OL_B &= e_B^T \left(\mathbb{1} + HM(\mathbb{1} - e_B e_B^T)\right)^{-1} HMe_B \end{aligned} \tag{2.13}$$

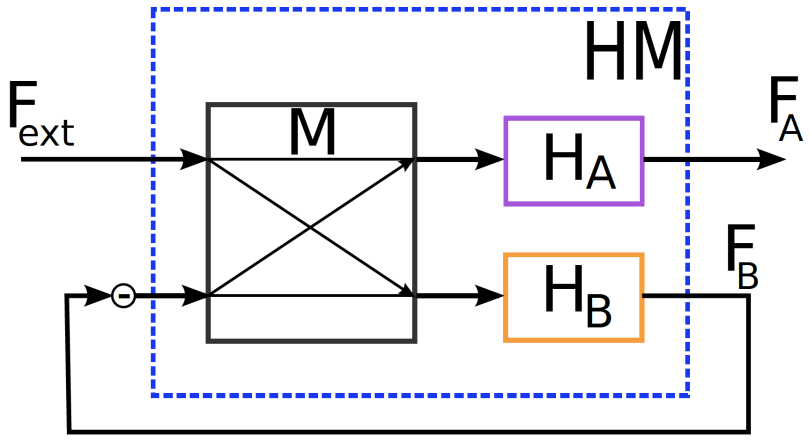

Figure 7 : Block diagram of beam A and beam B. The transfer function F_A/F_{ext} is equal to OL_A from Eq. (2.13). Each loop affects the other resulting in cross terms present in the matrix HM. M and $H_{A,B}$ are the transfer functions of the mechanical system and the optical springs of beam A and B, respectively.

with $e_A^T = (1,0)$ and $e_B^T = (0,1)$. The derivation of this expression is given in Appendix 2.9.

2.3.1 An example

It is worth considering a specific set of possible values for our model and evaluate the control of angular and longitudinal degrees of freedom of a gram-scale test mirror using the radiation pressure of the light. All the optical fields involved in our analysis are derived from the same wavelength light source through frequency shifting. The model includes two optical cavities (Fig. 6), referred to as beam A and B, both with an optical finesse of about 8500, line width $\gamma/(2\pi) = 125\,\mathrm{kHz}$ and mechanical frequency of $\backsim 1\,\mathrm{Hz}$. The main cavity (beam A) is pumped with 1 W of carrier light, detuned by $\delta/(2\pi) = 250\,\mathrm{kHz}$ (blue detuning, $\delta/\gamma = 2$), and 0.2 W of subcarrier light, detuned by $\delta/(2\pi) = 62\,\mathrm{kHz}$ (red detuning, $\delta/\gamma = -0.5$). This produces a statically and dynamically stable optical spring with a lever arm of 0.8 mm, measured from the mirror center of gravity (C.O.G.). A second optical spring (beam B) is pumped with 6 times less power of carrier light, detuned by $= 186\,\mathrm{kHz}$ (blue detuning, $\delta/\gamma = 1.5$), and 40 mW of subcarrier light, detuned by 62 kHz (red detuning, $\delta/\gamma = -0.5$). This side cavity has a lever arm of 3.3 mm on the mirror, such that the DC radiation

pressure torques of beam A and B cancel. The DC radiation pressure force can be canceled by displacing the position pendulum.

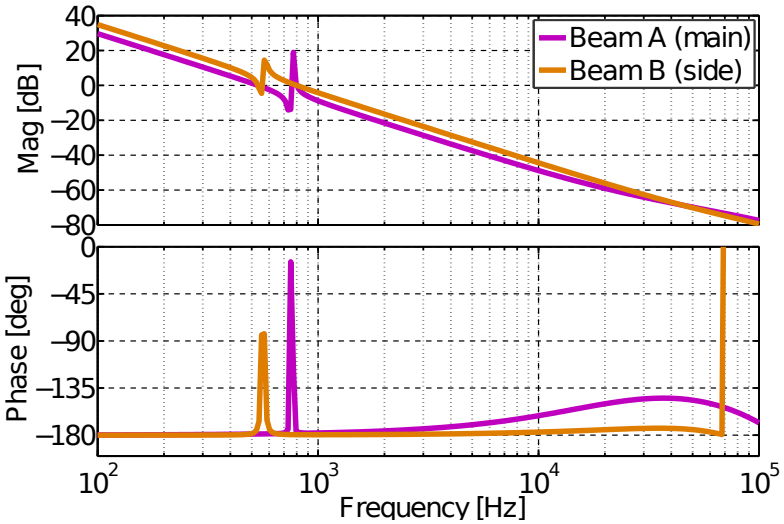

Figure 8 : Open loop gain (OLG) for the main and side cavity. The respective other loop is closed, and shows up as a resonance in the OLG. Note that, despite multiple unity gain crossings, both loops are stable because the resonances effectively implement a lead filter and the OLG avoids the critical point -1. Thus the dynamic interplay between multiple trapping beams on one payload does not introduce an instability.

The stability of the combined two-dimensional system is addressed in Fig. 8. Plotted are the open loop gain functions of the two degrees of freedom (the two optical traps) under the assumption that the other loop is closed. The presence of the second loop introduces a resonance feature in each loop at the unity gain frequency of the other loop. However the open loop gain avoids the critical point -1 (phase at zero), leading to a stable system. The model parameters were intentionally tuned for low damping / high quality factor in order to demonstrate that the system remains stable. Lower quality factors, and therefore stronger cooling is easily achievable.

2.3.2 Stability range

We can now estimate the robustness of our feedback control system by changing the microscopic length x_A and x_B of the two cavities. This changes the detuning of the optical springs for both beams. Therefore the propagators X_A and X_B for both beams change according to $X_{A,B} = r_1 r_2 e^{-i\delta_{A,B}\tau_{A,B}} \cdot e^{ikx_{A,B}}$. For each position both the

static and dynamical stability of the total optical spring system given by Eq. (2.13) is reevaluated.

In Fig. 9 the radiation pressure force due to the intracavity power of both beams versus the cavity offset is shown. The green shaded area represents the position range in which the two loops remain stable. The range is $\backsim$ 20 pm. The DC force fluctuations that the system can tolerate are given by the y-axis interval that the total radiation force spends in the green shaded area.

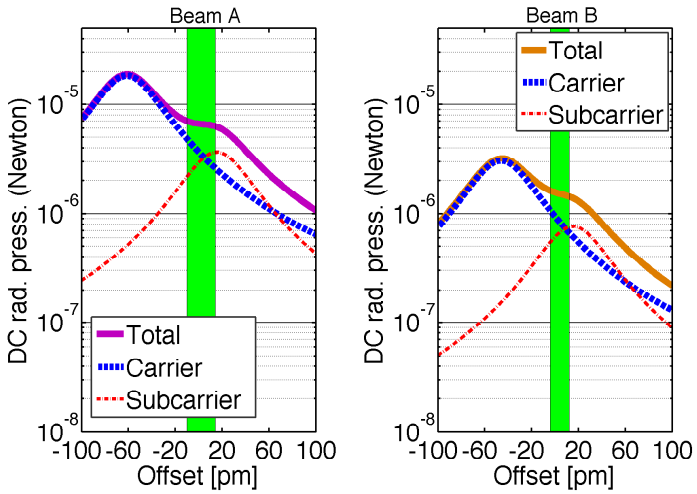

Figure 9 : Static carrier and subcarrier build-up (calibrated in radiation pressure force) as a function of the respective cavity position. Also shown in purple and orange are the total radiation pressure forces of the two cavities. Using the stability testing method from Sec. 2.3.2 we find that the trap is both statically and dynamically stable in the green shaded area. With the chosen model parameters those regions are about 20 picometers wide.

2.4 Angular instability

When operated with high intracavity laser power, suspended Fabry-Perot cavities like the arm cavities of LIGO have a well known angular instability. It arises from coupling the misalignment of the two cavity mirrors to radiation pressure torques. This is known as the Sidles-Sigg instability [17]. In this section we show that the intrinsic strength of an optical trap for alignment degrees of freedom is generally bigger, i.e. has a bigger spring constant than any associated Sidles-Sigg instability.

We start with a cavity of length L, with x_1, x_2 being the position of the beam

spots on mirrors 1 and 2. θ_1, θ_2 are the yaw angles of the two mirrors and R_1, R_2 are their radii of curvature. The corresponding g-factors are $g_{1,2} = 1 - L/R_{1,2}$. If one or both of the mirrors are slightly misaligned ($\theta_{1,2} \neq 0$), then the radiation pressure force exerts torques T_1 and T_2 on the two mirrors, given by (see for instance [17] or [31])

$$\begin{pmatrix} T_1 \\ T_2 \end{pmatrix} = \frac{F_0 L}{1 - g_1 g_2} \begin{pmatrix} g_2 & -1 \\ -1 & g_1 \end{pmatrix} \begin{pmatrix} \theta_1 \\ \theta_2 \end{pmatrix}, \tag{2.14}$$

where $F_0 = P_0 \frac{t_1^2}{(1-X)(1-\overline{X})} \frac{2r_2^2}{c}$ is the intracavity radiation pressure force. Sidles and Sigg first pointed out that, since the determinant of the matrix in this equation is negative, the two eigenvalues have opposite sign. This always leads to one stable and one unstable coupled alignment degree of freedom.

First we note that for a situation in which one mass is sufficiently heavy that we can neglect any radiation pressure effects on it (i.e. $\theta_1 = 0$), it is sufficient to choose a negative branch cavity (i.e. $g_1 < 0$ and $g_2 < 0$) to stabilize the setup. This is for instance the case for the example setup described in Fig. 6.

Next we want to compare the order of magnitude of this effect to the strength of an angular optical spring. If we call h the typical distance of the beam spot from the center of gravity of the mirror, and x the cavity length change at that spot, the order of magnitude of the optical spring torque is

$$T \approx \frac{F_0 L}{1 - g_1 g_2} \cdot \frac{x}{h} \tag{2.15}$$

We can express this as the strength of an optical spring located at position h. The corresponding spring constant $K_{SS} \approx T/(hx)$. Thus we can see that

$$K_{SS} \approx \frac{F_0}{1 - g_1 g_2} \cdot \frac{L}{h^2}. \tag{2.16}$$

We now consider the adiabatic optical spring ($\Omega = 0$) in Eq. (2.7). Expressed in terms of F_0, K_{OS} becomes

$$K_{OS} = i F_0 \frac{X - \overline{X}}{(1 - X)(1 - \overline{X})} 2k \tag{2.17}$$

Since we operate near the maximum of the optical spring, the order of magnitude of the resonance term can be estimated as

$$\frac{X - \overline{X}}{(1 - X)(1 - \overline{X})} \approx \frac{-i}{1 - |X|} \tag{2.18}$$

Thus we can estimate the magnitude of K_{OS} as

$$K_{OS} \approx F_0 \frac{4\pi}{\lambda} \frac{1}{1-|X|} \approx F_0 \frac{4}{\lambda} \mathcal{F} \tag{2.19}$$

where $\mathcal{F}$ is the cavity finesse. From Eqs. (2.16) and (2.19) we see that the optical spring K_{OS} is much larger than the Sidles-Sigg instability spring K_{SS} if

$$h^2 >> \frac{\lambda L}{\pi} \frac{1}{1-g_1 g_2} \frac{\pi}{4\mathcal{F}} \tag{2.20}$$

Now recall that the beam spot size in a Fabry-Perot cavity is given by [32]

$$w_1^2 = \frac{\lambda L}{\pi} \sqrt{\frac{g_2}{g_1(1-g_1 g_2)}} \tag{2.21}$$

Assuming a symmetric cavity ($g_1 = g_2$) for simplicity, we thus find that K_{OS} dominates over K_{SS} if

$$h^2 >> w_{1,2}^2 \frac{1}{\sqrt{1-g_1 g_2}} \frac{\pi}{4\mathcal{F}} \tag{2.22}$$

This condition is naturally fulfilled since we need to operate the angular optical spring with separate beams ($h > w_{1,2}$) and a large finesse ($\mathcal{F} >> 1$). Therefore the angular optical spring is indeed strong enough to stabilize the Sidles-Sigg instability.

2.5 Radiation pressure noise

Another advantage of radiation pressure angular control, compared to a classical approach based on photo detection and feedback, is its fundamental noise limit. The classical approach used in gravitational-wave detectors measures angular displacement of a single beam using wave-front sensors. Unlike that control method, the shot noise and other sensing noises never enter a radiation-pressure-based feedback loop. Even though technical laser noise is typically bigger in the simple cavity setup discussed in this paper, the only fundamental noise source of the scheme is quantum radiation pressure noise. In this section we give the full expression for radiation pressure noise in the case of a dual-carrier stable optical spring.

First, we note that as long as we are interested in frequencies much smaller than the any of the features in the detuned cavity transfer function, the radiation pressure

noise is relatively simple. If we also assume that the end mirror has a reflectivity of 1, the one-sided ($f \geq 0$) radiation-force amplitude spectral noise density is given by

$$S_F(f) = \frac{2}{c} G_{DC} \sqrt{2\hbar\omega P_0} \tag{2.23}$$

where G_{DC} is the power gain of a static cavity in the detuned configuration, P_0 is the power of the shot noise limited beam entering the cavity, and ω is its frequency. Equation (2.23) is valid for carrier and subcarrier separately. Note that this equation does not hold if the end mirror has a finite transmissivity, as quantum fluctuations entering from that port will also contribute to the intracavity shot noise. In the case of a critically coupled cavity, this will result in an increase of the intracavity radiation-force amplitude spectral noise density by exactly a factor of 2.

To calculate the exact expression for the radiation pressure noise induced cavity fluctuations, including behavior near the cavity pole frequency, we first realize that we can calculate the radiation-force amplitude spectral noise for a static cavity, and then compute the response of the dual-carrier optical spring system to that driving force. This yields the correct answer up to first order in the size of the quantum fluctuations. For the calculation we track the quantum vacuum fluctuations entering at both ports of the cavity. We introduce F, the amplitude build-up factor for a fluctuation at frequency $f = \frac{\Omega+\delta+\omega_{res}}{2\pi}$:

$$F(f) = \frac{1}{1 - XY^2} = \frac{1}{1 - r_1 r_2 e^{-2i\delta\tau} e^{-2i\Omega\tau}} \tag{2.24}$$

Thus, the total buildup for fluctuations entering through the input coupler (1) and the end mirror (2) are

$$t_1 F(f) \text{ and } r_1 t_2 F(f), \tag{2.25}$$

where we already dropped the one-way propagation factor because it drops out in the radiation force noise calculation below. We can now introduce the notation $F_0 = F(f_0)$, $F_+ = F(f_0 + f)$ and $F_- = F(f_0 - f)$. We then get the following expression for the one-sided radiation-force power spectral density for either carrier or subcarrier.

$$S_F(f) = \frac{2}{c} S_P(f) \text{ and } S_P(f) = G(f)\sqrt{2\hbar\omega P_0} \tag{2.26}$$

$$G^2(f) = \frac{1}{2} t_1^2 |F_0|^2 (t_1^2 + r_1^2 t_2^2)(|F_+|^2 + |F_-|^2) \tag{2.27}$$

Here P_0 is the entering carrier power, and f_0 is its frequency. We can see that we recover Eq. (2.23) in the limit $t_2 \to 0$ and $G/t_1^2 = |F_0|^2 = |F_+|^2 = |F_-|^2$. The resulting force noise from carrier and subcarrier for the cavity A in the example above (see Fig. 6) is plotted in Fig. 10 (top).

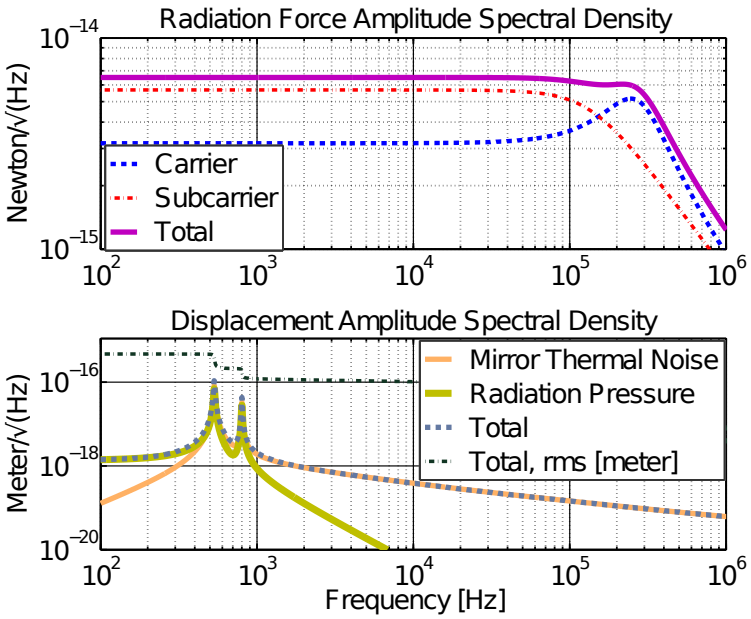

Figure 10 : (Top) Radiation force amplitude spectral density for the dual-carrier optical spring used in beam A of the above example. The subcarrier dominates the noise at low frequency, but the higher-power carrier contributes more at high frequencies. Also note that if we choose the same free spectral range for the two carriers, there would be an additional beat note at the difference frequency of 310 kHz. (Bottom) Radiation pressure and thermal noise displacement amplitude spectral density. The radiation pressure noise is calculated using the optomechanical response given in Eq. (2.28). The thermal noise is based on a theoretical calculation described in [27], [31]. Since seismic and suspension thermal noise depend on the experimental implementation, they are not shown, but they would also be suppressed by the optical spring closed loop response. The residual rms motion due to the shown noise sources is less than 10^{-3} picometers. With the total rms motion smaller than the 20 picometer stability band shown in Fig. 9, the two cavities will remain locked purely due to the radiation pressure trapping force.

Next we calculate the response of the coupled optomechanical system to this driving force, using the following closed loop transfer function obtained from Eqs. (2.11) and (2.12):

$$x = M(1 + HM)^{-1}F \tag{2.28}$$

Above the optical spring resonances this leads to a $1/f^2$ falloff of the displacement noise, as expected for radiation pressure noise. Meanwhile below the resonance, due to the closed loop suppression, we will have a flat displacement noise. Figure 10 (bottom) illustrates this in the case of the two-dimensional angular trap discussed above. The level of this flat displacement noise below the unity gain frequency, or optical spring resonance, is at

$$S_x(f) = \frac{S_F(f)}{K_{OS}} \tag{2.29}$$

$$\backsim \frac{\lambda}{\mathcal{F} P_0} \sqrt{2\hbar\omega P_0} \tag{2.30}$$

where we used Eqs. (2.19) and (2.23) for the estimate, and $\mathcal{F}$ is the cavity finesse.

To compare this noise limit with existing schemes we will consider three angular control schemes: wave front sensing with a single beam (as seen in modern gravitational-wave detectors [19, 20]), two spatially separated beams with stable optical springs, and an intermediate scheme of two spatially separated beams locked with no detuning using the Pound-Drever-Hall technique [33].

First we compare the sensitivity to a cavity locked with a Pound-Drever-Hall classical feedback scheme. For the sake of this comparison we want the same dynamics, i.e. the same unity gain frequency and roughly the same loop-shape as in the optical spring system. We can however vary the input power. In addition to radiation pressure noise we now also have sensing noise. Photo diode sensing is limited by photo diode quantum efficiency and other factors such as modulation depth, mode matching and overlap. Additionally, in gravitational-wave interferometers the available beam pick-off fraction for alignment sensing is tiny. All of these factors are typically less than or equal to one, which causes a relative increase in the sensing noise. However, we will not consider these effects for the moment so that we can simply illustrate our point. At best we can use all available power and only have shot noise to worry about. Then the sensing noise is given by

$$S_x \backsim \frac{\lambda}{\mathcal{F} P_0} \sqrt{2\hbar\omega P_0} \tag{2.31}$$

We are interested in the noise in the frequency band between the mechanical resonance frequency and the unity gain frequency of the control loop. In this band the radiation pressure noise is loop-suppressed to the level of Eq. (2.29), while the displacement

noise due to sensing noise is given by Eq. (2.31). At the nominal power P_0 the two schemes are the same. If we now vary P_0, we find that the displacement due to sensing noise scales as $P_0^{-1/2}$, while the displacement due to radiation pressure noise scales as $P_0^{1/2}$ [see Eq. (2.23)]. Note that we keep the feedback gain in Eq. (2.29) equal to the unchanged reference optical spring K_{OS} in order to maintain the same unity gain frequency. We conclude that the lowest total noise, and therefore the best classical feedback scheme, can be achieved at the same power the optical spring operates. Thus the classical scheme can achieve about the same sensitivity as the optical spring system, but in practice performs worse due to real-world sensing limitations.

Finally we want to compare the displacement noise of Eqs. (2.31) and (2.29) to a wave front sensing scheme. The approximate shot noise limited sensing noise for beam angular and transverse position mismatch, S_θ and S_w, of a wave front sensing scheme is given by

$$S_\theta \backsim \frac{\theta_0}{P_0}\sqrt{2\hbar\omega P_0} \tag{2.32}$$

$$S_w \backsim \frac{w_0}{P_0}\sqrt{2\hbar\omega P_0} \tag{2.33}$$

where the divergence angle θ_0 and waist size w_0 of the resonant beam in the cavity are related to the wave length through $\theta_0 w_0 \pi = \lambda$ [34]. We can directly compare this wave front sensing scheme to Eq. (2.29) if we divide our result by the beam separation d. As long as we choose the beam separation d to be larger than spot size w, the angular sensitivity of a two-beam system such as the optical spring system is better than the wave front sensing scheme by a factor given by the cavity finesse. Intuitively this result can be understood because having two cavity resonance conditions in the two cavities restricts the angular deviations much tighter than in a one-cavity case.

2.6 Conclusions

In conclusion, we investigated the use of the radiation pressure of laser light as an alternative to a conventional feedback system for controlling the longitudinal and angular degrees of freedom of a mirror. The method is based on a double dual-carrier scheme, using a total of four detuned laser fields in two cavities. The two dual-carrier beams hit the mirror in separate spots, forming two stable optical springs. This constrains both the longitudinal and the angular degrees of freedom of the mirror,

replacing completely the commonly used electronic feedback system. We showed that this setup allows a stable control of the two degrees of freedom, within a displacement range of the test mirror of $\sim 20\,\mathrm{pm}$. This promising idea can be extended to the other angular degree of freedom. We found that such a method creates an angular optical spring stronger than the angular Sidles-Sigg instability, which drives the requirement for angular control in the high power arm cavities of gravitational-wave detectors. We also showed that the fundamental limit of this scheme is the quantum radiation pressure noise, resulting in a reduction in control noise compared to a conventional active feedback approach. We are working towards the experimental demonstration of this effect for a gram-scale mirror and beginning to explore its extension to large-scale gravitational-wave detectors.

2.7 OPTICAL SPRING CONSTANT DERIVATION

In this section we consider the effect of light stored in a detuned Fabry-Perot cavity using a classical approach. The intracavity power generates radiation pressure that exerts on the cavity mirror a force $F_{rad} = -K_{OS} \cdot x$, where x is the mirror displacement and K_{OS} is the optical spring constant. Here we show the full derivation of the optical spring constant K_{OS}.

We consider a suspended Fabry-Perot cavity of length L_0 with an incident beam of wavelength λ and power P_0. First we calculate a general expression of the intracavity power and then its radiation pressure force exerted on the end mirror.

The field $E = A_0 e^{i\omega t}$ enters the cavity (shown in Fig. 11) through the input mirror of coefficient $t_1 = t$ and r_1 and the field inside the cavity at the input mirror can be seen as the following:

$$E_{tot} = E_0 + E_1 + E_2 + E_3 + ... + En + ... \tag{2.34}$$

We consider in our model the following definitions, with d_n being the displacement of the mirror,

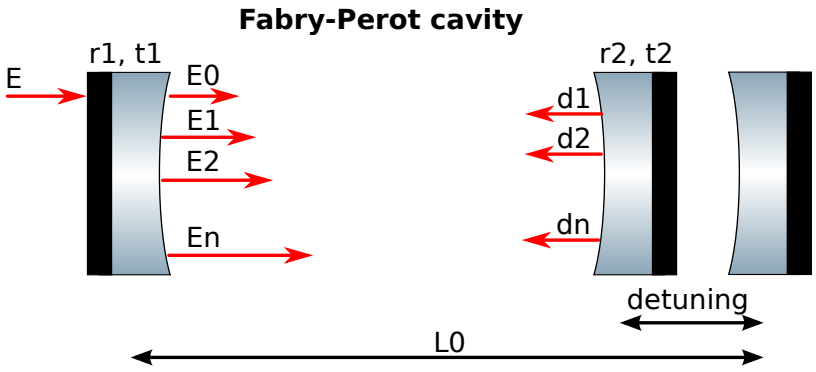

Figure 11 : A Fabry-Perot cavity of length L_0 and coefficients r_1, t_1 and r_2, t_2 for the input and end mirrors respectively. The input mirror is stationary while the end mirror is affected by harmonic motion. The incoming field E at each round-trip i adds up a phase shift due to the displacement d_i

$$\begin{aligned} L_1 &= 2(L_0 + d_1) \\ L_2 &= 2(2L_0 + d_1 + d_2) \\ L_3 &= 2(3L_0 + d_1 + d_2 + d_3) \\ &\dots \end{aligned} \tag{2.35}$$

with

$$d_n = d(t - [(2n-1)\tau + \alpha_n]) \quad \text{and} \tag{2.36}$$

$$\alpha_n = 2\sum_{l=1}^{n-1} \frac{d_l}{c} - \frac{d_n}{c} \tag{2.37}$$

where $\tau = L_0/c$. With the round trip length $L = 2L_0$ and with $X = r_1 r_2 e^{-ikL}$ we obtain

$$\begin{aligned} E_{tot} = tE(1 + Xe^{-2ikd_1} + X^2 e^{-2ik(d_1+d_2)} \\ + X^3 e^{-2ik(d_1+d_2+d_3)} \dots) \end{aligned}$$

Since by definition the optical spring K_{OS} is the linear term in the expansion $F = F_0 + K_{OS} d + O(d^2)$, we now expand the exponential in d_n and we group d_n terms

$$E_{tot} = \frac{tE}{1-X}(1 - 2ikd_1X - 2ikd_2X^2 - 2ikd_3X^3 + \cdots)$$

Given that any correction from α_n [Eq. (2.37)] is quadratic in $d(t)$, we can again neglect it by definition, and find for the harmonic mirror motion (i.e. in the Fourier domain)

$$\begin{aligned} d_n = & \quad x_0 e^{i\Omega(t-(2n-1)\tau)} = x_0 e^{i\Omega t} e^{-i\Omega(2n-1)\tau} \\ = & \quad x_0 e^{i\Omega t} \frac{Y^{2n}}{Y} \frac{Y}{Y} = Y^{2n-2} d_1 \end{aligned} \tag{2.38}$$

where $Y = e^{-i\Omega\tau}$. Thus we can write

$$E_{tot} = \quad \frac{tE}{1-X}\left[1 - \frac{2ikd_1X}{1-Y^2X}\right] \tag{2.39}$$

where d_1 is a complex number. Since we have to take its real part $Re(d_k) = \frac{d_k+\bar{d}_k}{2}$, we consider the field inside the cavity with $\bar{d}_k$ conjugate of d_k and we obtain as total field:

$$E_{tot} = tE\left[\frac{1}{1-X} - \frac{2ikX}{2(1-X)}\left(\frac{d_1}{1-Y^2X} + \frac{\bar{d}_1}{1-\overline{Y}^2X}\right)\right]$$

Using the following expression

$$d_1 = x_0 e^{i\Omega(t-\tau)} = x_0 e^{i\Omega t} e^{-i\Omega\tau} = xY \tag{2.40}$$

we can now obtain the intracavity power expression by multiplying E_{tot} by its conjugate and considering only the linear terms of x and $\bar{x}$

$$\begin{aligned} P = & \quad E_{tot} \cdot \overline{E}_{tot} = -P_0 t^2 [\frac{ikY}{(1-\overline{X})(1-X)} \\ \times & \quad \left(\frac{X}{1-Y^2X} - \frac{\overline{X}}{1-Y^2\overline{X}}\right) x + cc] \end{aligned} \tag{2.41}$$

where we have also neglected the first constant term.

Once we have calculated the power we can obtain the radiation pressure force on the end mirror by $F_{rad} = \frac{2r_2^2}{c}P$. Furthermore we can also notice the similarity of the expression with the elastic force. Thus we recall that in frequency domain and complex notation K is defined by $F = -Kx$, the real form is thus

$$F' = Re[F] = -\frac{1}{2}(Kx + \overline{K}\bar{x}) = -\frac{1}{2}(Kx + cc)$$

Taking into account that we are calculating the radiation pressure on the end mirror, we need to consider an extra delay factor Y for the calculation of the power which appears in the expression of K. The complex spring is then given by

$$K_{OS} = \frac{2r_2^2}{c} P_0 t^2 \frac{2ikY^2}{(1-\overline{X})(1-X)} \left(\frac{X}{1-Y^2X} - \frac{\overline{X}}{1-Y^2\overline{X}} \right)$$

which can be rewritten in the form of Eqs. (2.6) and (2.7).

2.7.1 Detuning

Given the frequency detuning is $\delta = \omega_0 - \omega_{res}$ and $\Omega = \omega - \omega_0$, where ω_0 is the carrier (subcarrier) frequency and $\omega_{res} = 2\pi n \cdot c/L$ is the resonant frequency, we get the following expression:

$$e^{-ikL} = e^{-i\delta 2\tau} \tag{2.42}$$

If we now replace X and Y we obtain the exact expression for K_{OS}:

$$\begin{aligned} K_{OS} = &- P_0 t^2 r_2^2 \frac{4ike^{-2i\Omega\tau}}{c(1-r_1r_2e^{i2\delta\tau})(1-r_1r_2e^{-i2\delta\tau})} \times \\ &\left(\frac{r_1r_2e^{-i\delta\tau}}{1-r_1r_2e^{-2i\Omega\tau}e^{-i2\delta\tau}} - \frac{r_1r_2e^{i2\delta\tau}}{1-r_1r_2e^{-2i\Omega\tau}e^{i2\delta\tau}} \right) \end{aligned} \tag{2.43}$$

2.7.2 Comparison

To compare to existing literature we now expand the exponentials to linear order in Ω and δ, $e^{-i\delta 2\tau} \approx 1 - i\delta 2\tau$ and $e^{-i2\Omega\tau} \approx 1 - i2\Omega\tau$:

$$
\begin{aligned}
K_{OS} = &- P_0 t^2 r_2^2 \\
&\times \frac{4ik(1-2i\Omega\tau)r_1 r_2}{c(1-r_1r_2+r_1r_2 i2\delta\tau)(1-r_1r_2-r_1r_2 i2\delta\tau)} \\
&\times \left[\frac{1-i2\delta\tau}{1-r_1r_2(1-2i\Omega\tau-i2\delta\tau)} - \frac{1+i2\delta\tau}{1-r_1r_2(1-2i\Omega\tau+i2\delta\tau)}\right]
\end{aligned}
\tag{2.44}
$$

We further simplify this equation using expressions for the $Finesse \approx \pi \frac{r_1 r_2}{1-r_1 r_2} = \pi FSR/\gamma$ and the free spectral range $FSR = 1/2\tau$, introducing the cavity bandwidth γ. We also neglect the $i\Omega\tau$, $i\delta\tau$ terms in the numerator since they correspond to a simple time delay. We obtain:

$$
K_{OS} \approx \qquad P_0 t^2 r_2^2 \frac{8k r_1 r_2}{c(1-r_1r_2)^3} \frac{\frac{\delta}{\gamma}}{(1+\frac{\delta^2}{\gamma^2})} \left[\frac{1}{1+\frac{\delta^2}{\gamma^2}-\frac{\Omega^2}{\gamma^2}+i2\frac{\Omega}{\gamma}}\right]
\tag{2.45}
$$

which is equivalent to the expression already existing in the literature [30, 15].

2.7.3 Overcoupled cavity

In the particular case of perfectly overcoupled cavity ($r_2 = 1$) $Finesse/\pi = 2/T_1$ and $(1-r_1r_2)^2 = T_1^2/2$ and the optical spring constant becomes

$$
K_{OS} \approx \qquad 128 P_0 \frac{\pi}{c\lambda T_1^2} \frac{\frac{\delta}{\gamma}}{(1+\frac{\delta^2}{\gamma^2})} \left[\frac{1}{1+\frac{\delta^2}{\gamma^2}-\frac{\Omega^2}{\gamma^2}+i2\frac{\Omega}{\gamma}}\right]
\tag{2.46}
$$

2.7.4 Matched cavity

In this case of a matched cavity ($r_1 = r_2$) $Finesse/\pi = 1/T_1$ and $(1-r_1r_2)^2 = T_1^2$ and the optical spring constant remains the same as in Eq. (2.46) except for the the factor 128 which has to be replaced with 16.

2.8 TORSION PENDULUM MECHANICAL PLANT

Here we transform the basis of coordinates $\{x_G, \Theta\}$ formed by the position of the center of gravity x_G of the mirror and its rotation angle Θ with respect to the vertical axis passing from x_G into a basis $\{x_A, x_B\}$ formed by the length of the cavities relative to beam A and beam B respectively. Thus the longitudinal and angular control of the mirror can be treated as the longitudinal control of the two above mentioned cavities. The basis can be expressed as

$$\begin{pmatrix} x_A \\ x_B \end{pmatrix} = \begin{pmatrix} 1 & r_A \\ 1 & r_B \end{pmatrix} \begin{pmatrix} x_G \\ \Theta \end{pmatrix} = \mathcal{B} \begin{pmatrix} x_G \\ \Theta \end{pmatrix} \tag{2.47}$$

where r_A and r_B are the lever arms of the two beams with respect to x_G.

The equation of motion for the mirror is

$$-\omega^2 \begin{pmatrix} m & \\ & I \end{pmatrix} \begin{pmatrix} x_G \\ \Theta \end{pmatrix} = \begin{pmatrix} F_{tot} \\ T_{tot} \end{pmatrix} \tag{2.48}$$

where I is the moment of inertia of the mirror of mass m. We now express the total force and the total torque exerted on the mirror as function of the individual forces F_A and F_B:

$$\begin{pmatrix} F_{tot} \\ T_{tot} \end{pmatrix} = \begin{pmatrix} 1 & 1 \\ r_A & r_B \end{pmatrix} \begin{pmatrix} F_A \\ F_B \end{pmatrix} = \mathcal{B}^T \begin{pmatrix} F_A \\ F_B \end{pmatrix} \tag{2.49}$$

Using Eqs. (2.49) and (2.47) in Eq. (2.48) we obtain the equation of motion in the x_A, x_B basis:

$$-\omega^2 \left[\mathcal{B}^{T-1} \begin{pmatrix} m & \\ & I \end{pmatrix} \mathcal{B}^{-1} \right] \begin{pmatrix} x_A \\ x_B \end{pmatrix} = \begin{pmatrix} F_A \\ F_B \end{pmatrix} \tag{2.50}$$

2.9 STABILITY IN TWO DIMENSIONS

The control loop stability in multiple dimensions can be evaluated by considering the one-dimensional open-loop transfer function of every control filter (i.e. optical spring) while all other loops stay closed. Here we calculate these open-loop transfer functions for the two-dimensional case.

Referring to Fig. 7, we inject a signal $F_{\rm ext}$ into the path of beam A. The output of path A is F_A. Simultaneously we close the control loop relative to beam B by feeding back the force F_B, which represents the output of path B.

We obtain the following expression:

$$HM \begin{pmatrix} 0 \\ -F_B \end{pmatrix} + HM \begin{pmatrix} F_{ext} \\ 0 \end{pmatrix} = \begin{pmatrix} F_A \\ F_B \end{pmatrix} \tag{2.51}$$

If we introduce the 2×2 matrix S,

$$S_A = \begin{pmatrix} 0 & 0 \\ 0 & 1 \end{pmatrix} \tag{2.52}$$

we can write

$$HMS_A \begin{pmatrix} -F_A \\ -F_B \end{pmatrix} + HM \begin{pmatrix} F_{ext} \\ 0 \end{pmatrix} = \begin{pmatrix} F_A \\ F_B \end{pmatrix} \tag{2.53}$$

Using the vector $e_A^T = (1, 0)$ we are able to extract the following open loop transfer function related to cavity A:

$$OL_A = \frac{F_A}{F_{ext}} = e_A^T (\mathbb{1} + HMS_A)^{-1} HMe_A \tag{2.54}$$

The same open loop transfer function can be obtained considering an external signal injected into the loop of the beam B while the loop of beam A remains closed,

$$OL_B = \frac{F_B}{F_{ext}} = e_B^T (\mathbb{1} + HMS_B)^{-1} HMe_B \tag{2.55}$$

with $e_B^T = (0, 1)$ and

$$S_B = \begin{pmatrix} 1 & 0 \\ 0 & 0 \end{pmatrix}. \tag{2.56}$$

Chapter 3

Suspensions

Suspending the optics is one of the most complicated parts of the experiment. The optics are constructed as discs with roughly 76 mm (3 inch) diameters. They are suspended from modified Small Optics Suspensions (SOSs) and controlled with Optical Sensing Electro-Magnets (OSEMs).

3.1 Input coupler

The input coupler (see fig 12) is designed to hold three mirrors at specific positions and angles. The mirrors are 0.5 inches in diameter with 7.5 cm RoC. They are mounted in an approximately 300 gram aluminum disk. The central mirror forms the straight cavity with the end mirror, while the two mirrors on the side are part of the folded cavity. The angle and, to a lesser degree, z position of the two side mirrors are adjustable using set screws.

For each of the adjustable mirrors, set screws push on the bevel of the back surface of the mirror. The mirror is held in place by a Teflon tube placed on the front side of the mirror, which is in turn clamped down with springs on screws. This gives us the flexibility to adjust for manufacturing defects and to adjust the beam separation on the end mirror after construction.

Tapped screws in the top and bottom allow for precision correction of the center of mass of the mass after suspension. The mirrors are shifted laterally to make the mirrors fit inside the 3.0 inch diameter of the aluminum mass.

The design concerns governing the placement of the holes include the separation of

the beams, the angle of the folded cavity, and the desired lengths of the two cavities.

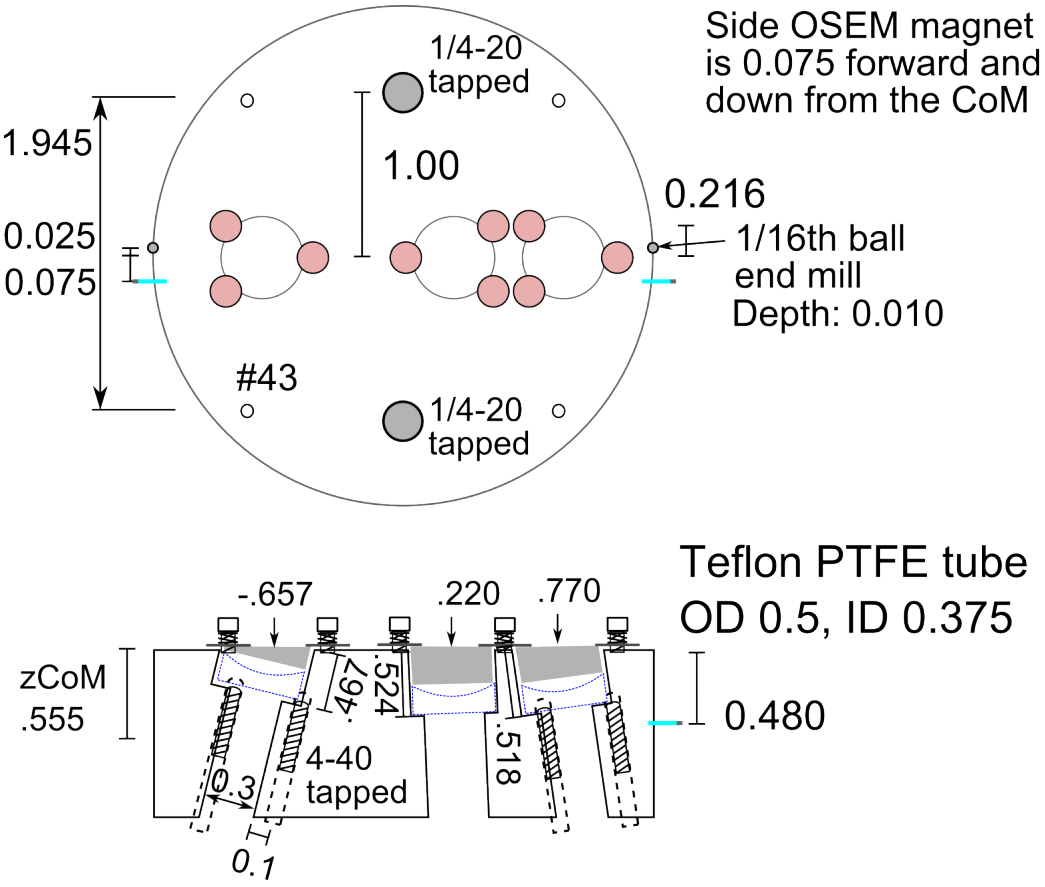

Figure 12 : The input coupler for the cavity. Three 0.5 inch diameter mirrors with 7.5 cm RoC are held at specific angles inside an aluminum disk. The two side mirrors are adjustable using set screws, while the central mirror is fixed.

3.2 End mirror

The end mirror has a diameter of 0.305 inches, a radius of curvature of 5 cm, and a mass of 0.4 grams. It is suspended by glass fibers from a steel ring, which is in turned suspended from a modified SOS. The suspension is pictured in 34.

The fibers are manufactured by cold welding a fused silica rod onto a mirror blank, creating a nub, then pulling a fiber off it, to a length of about 1 inch. Once the fiber cools, we break the cold weld. This leaves us with a nub attached to a fiber, which is in turn attached to a silica rod. The silica rod is glued into an aluminum block,

which is screwed down to the steel ring. The nubs are then glued to the actual mirror using Optocast 3553. Because the nubs were created on a mirror blank with the same diameter, the volume of glue required is minimized, reducing the thermal noise effects of the glue joint. After gluing on all three fibers, the fibers are tensioned to raise the resonance of the position mode to the desired frequency.

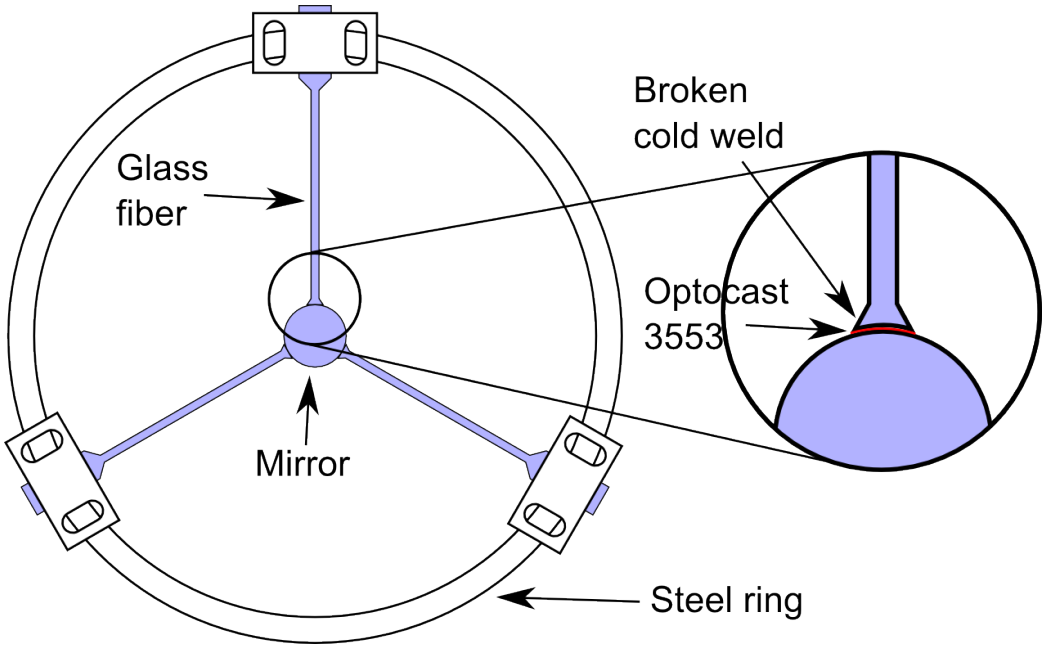

Figure 13 : End mass suspension. A 0.4 gram mirror is suspended from a steel ring using glass fibers.

3.3 Blade Springs

This is a discussion of the relevant physics to the construction of blade spring suspensions for a small optics suspension.

This theoretical parts of the paper are based primarily on the notes posted in the DCC [1].

3.3.1 A little theory

The paper gives the general formula for an elastic beam under a load (see Rourke's formulas for stress and strain, eq. 8.1-4):

[1] https://dcc.ligo.org/LIGO-T030285

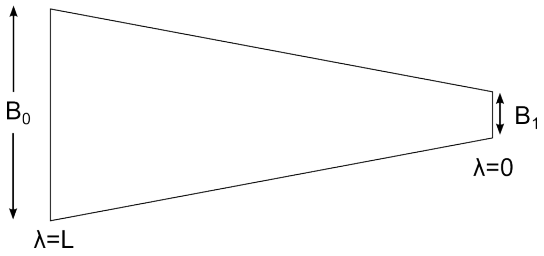

Figure 14 : Profile drawing of a deflected blade spring. R is the radius of the circle described by the blade spring when it is under stress. L is the length of the blade, b_0 is the large base and b_1 is the small base. λ is the distance along the blade

$$\frac{E}{R(\lambda)} = \frac{M(\lambda)}{I(\lambda)} \tag{3.1}$$

Here λ is the distance along the blade (with the $\lambda = 0$ at the tip), E is the Young's modulus, R is the radius of curvature at λ, I is the area moment of inertia at λ, and M is the bending moment at λ, expressed as:

$$M = mg\lambda \tag{3.2}$$

where m is mass supported, g is 9.81m/s^2.

$b = b_1 + (b_0 - b_1)\frac{\lambda}{L}$ is the width between $\lambda = 0$ ($b = b_1$) and $\lambda = L$ ($b = b_0$) (see figure 14) so

$$I = \frac{bt^3}{12} = (b_0 - b_1)\frac{t^3}{12}\frac{\lambda}{L} + b_1\frac{t^3}{12} \tag{3.3}$$

where t is the thickness of the blade and L is the blade length. If we consider the blade to be triangular ($b_1 = 0$), I becomes

$$I = \frac{b_0 t^3}{12}\frac{\lambda}{L} \tag{3.4}$$

Then we see that

$$\frac{E}{R(\lambda)} = \frac{M(\lambda)}{I(\lambda)} = \frac{mg\lambda}{b_0\frac{t^3}{12}\frac{\lambda}{L}} = \frac{12mgL}{b_0 t^3} \quad \rightarrow \quad R = constant \tag{3.5}$$

In other words, R is constant along the blade (the blade profile is circular). We can accomplish this behavior by specifying that the wire is clamped where the end of the 'triangle' should be.

Thus we can, without difficulty, treat a change in force on the spring (for instance by changing the mass) as a change in the radius of curvature of the blade.

From eq.3.5 we obtain R

$$R(\lambda) = R = \frac{Eb_0t^3}{12mgL} \tag{3.6}$$

From eq.3.6 we can obtain the bounce mode frequency f_b

$$f_b = \frac{1}{2\pi}\sqrt{\frac{Eb_0t^3}{6mL^3}} \tag{3.7}$$

and the maximum stress in the blade as:

$$\sigma = \frac{6mgL}{b_0t^2}; \tag{3.8}$$

We can use equation 3.8, solved for b_0, to simplify equation 3.7, thus

$$f_b = \frac{1}{2\pi}\sqrt{\frac{Egt}{L^2\sigma}} \tag{3.9}$$

Given a target stress σ, a target bounce frequency f_b, and a length limit L based on the chamber dimensions, we can determine the proper thickness t for the blade.

If we manipulate equations 3.9 and 3.8, we get

$$t = \frac{(2pif_bL)^2\sigma}{Eg} = \sqrt{\frac{6mgL}{b_0\sigma}} \tag{3.10}$$

This equation gives the minimum requirement to make a blade spring.

3.3.2 Materials

The LIGO-recommended material is "maraging" steel (sometimes known by the trade-name Vascomax), which is easy to machine, but becomes incredibly hard when baked.

One drawback of this material is that it can corrode over time. To combat this, LIGO recommends putting a nickel plating on the blades [2]. The hardness of the final product is the primary reason it is used. This material is difficult and expensive (best offer was $1200 for six blade's worth) to buy in small quantities.

As an alternative, we are considering "full hardened" 301 stainless steel. It is a factor of about 2.5 weaker than the maraging steel, but we have have found that workable solutions exist.

A third alternative is 17-4 precipitation hardened (PH) stainless. This material is similar to maraging steel in that it becomes harder when you bake it. Baking at 900 F for one hour results in a yield strength of 200000 psi = 1379 MPa. Baking longer or at a higher temperature makes the material a bit sorfter, but this behavior is understood and fairly error-tolerant [3]

One more alternative which LIGO uses for the small blade springs is 304 stainless (yield strength of 200 MPa) because the expected strain in the small blades is about 80 MPa.

For comparison, McMaster has details of many of the metals that are available [4]. All of the metals we are considering are on the LIGO vacuum compatible materials list[5].

When we are determining the maximum amount of stress that the blade can withstand before deforming, we typically use the yield strength. This is the amount of stress that causes the metal to deform by 0.2%. We have chosen as a target strain 60% of the yield strength.

One LIGO document [6] adds a factor related to the Poisson's Ratio to the Young's Modulus which effectively increases the strain. This is attributed to a change in the strain of the material due to bending. Our predictions seem to work better with this factor removed, but we have chosen to keep the factor for the moment because it represents the 'worst case' scenerio.

---

[2] https://dcc.ligo.org/LIGO-E0900023

[3] http://www.aksteel.com/pdf/markets_products/stainless/precipitation/17-4_PH_Data_Bulletin.pdf

[4] http://www.mcmaster.com/library/20121105/8984KAC.pdf

[5] https://dcc.ligo.org/LIGO-E960050

[6] https://dcc.ligo.org/LIGO-T0900324

Steel	E (GPa)	E (psi)	σ_{max} (MPa)	σ_{max} (PSI)
C350 Maraging	200	29×10^6	2344	34×10^4
301 Stainless	193	28×10^6	965	14×10^4
17-4 PH Stainless	196.5	28.5×10^6	1379	20×10^4
304 Stainless	193	28×10^6	207	3×10^4

Table 1 : Characteristics of proposed materials.

3.3.3 Blade spring design

Criteria for the design following the section 3.3.1:

1. Maintain safe levels $\leq 80\%$ of material stress limits: $\sigma \leq 0.8\sigma_{max}$.
2. Blades must be mounted on top of the existing suspensions; smaller is better.
3. Choose a 'small' (within reason) bounce mode frequency (This determines t).
4. Minimize vertical to horizontal coupling, looking at the effective length z_{max} as a function of different loads and angles. We could adjust the weight for a given angle or at fixed weight we adjust the angle. The latter is our way to go.

3.3.4 Small blade

At the same time, we are designing a similar suspension to be mounted on top of each SOS. These will be much smaller, but will follow the same design principles.

For the small spring system, our design is very similar to the parameters used in the HAM AUX design for ALIGO [7] We can use 304 Stainless or 17-4 Stainless with little impact on the final performance. The maximum stress of this design is only 40% of the expected yield strength of 304 and much less than that for 17-4. This gives us more leeway with the construction and reduces the chance of failure due to improper baking. The final design schematic is shown in figure 16. For the small design we have chosen to neglect the Poisson Ratio factor because the bending is much smaller. We are motivated to do this by the HAM AUX design mentioned earlier.

[7] https://dcc.ligo.org/LIGO-T1000339

Parameter	**Metric**	**Imperial**
Blade length, L	7.68 cm	3.0 in
Blade base width, b_0	3.3 cm	1.3 in
Blade thickness, t	0.51 mm	0.020 in
Mounting angle, θ	0.083 rad	4.78°
Supported mass, m	0.15 kg	0.33 lbs
Result	**Metric**	**Imperial**
Bounce Frequency, f_b	7.19 Hz	
Max height	2 mm	0.08 in
Tip height	2 mm	0.06 in
Effective length	7.7 cm	3.0 in
Maximum Stress, σ	81 MPa	11700 PSI

Table 2 : Characteristics of proposed blade design

3.3.5 Coupling

For the small spring system, we do not need to worry about this coupling because the motion will not couple to the position degree of freedom to first order. We should note that changing the effective length would result in a change in the yaw mode resonance of the suspended structure, which may be an issue.

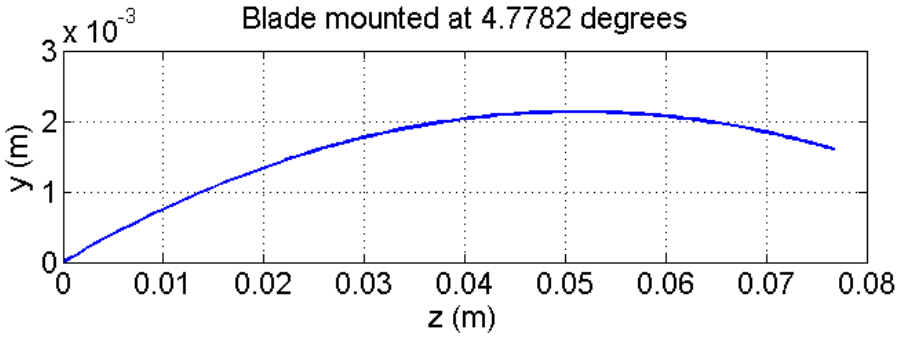

Figure 15 : Expected profile of the small blade supporting 300 grams.

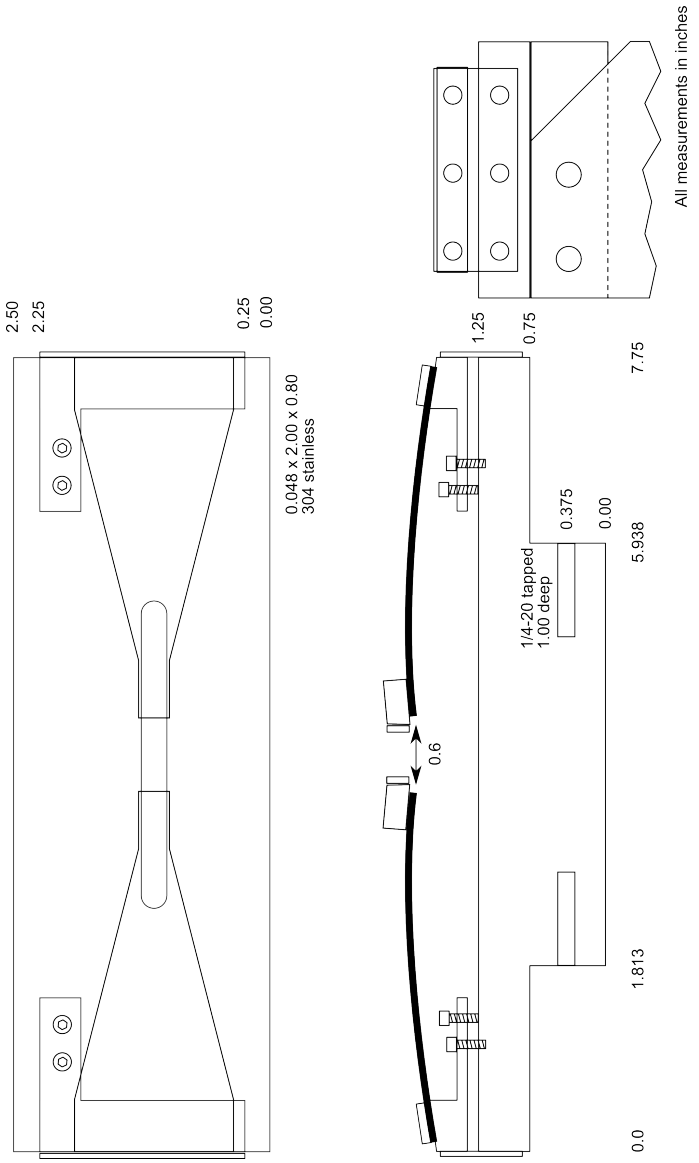

Figure 16 : Drawings for the small blade suspension modification to the SOS. The blade angle can be adjusted using the screws. This adjustment was used for fine adjustment of the optic height and rotation.

3.4 OSEM diagonalzation

To control the mass under vacuum, we use devices called OSEMs (Optical Sensing Electro-Magnets). These are devices (see fig. 17) that sense the position of an optic using magnets which are mounted on the optic. The magnet partially blocks light from an LED, so when it moves it causes changes in the voltage out from a photodiode. This signal is sent to the digital system, where it is converted into position, pitch, yaw, and side motion. Each of these degrees of freedom have specific filters applied to them, then the signals are converted back into the five sensor distances. Coils in the OSEM are driven accordingy, controlling the motion of the optic.

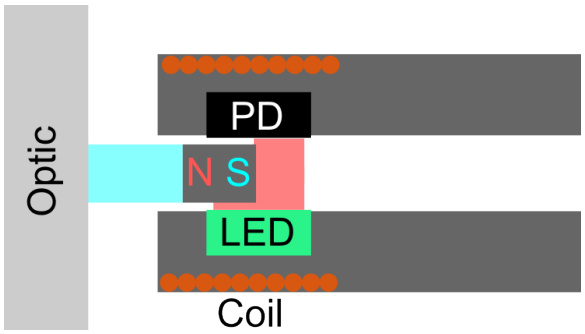

Figure 17 : Layout of an Optical Sensing Electro-Magnet (OSEM). Optic motion is sensed when the magnet changes the amount of light from the light emitting diode (LED) that gets to the photodiode (PD). The coils can be driven to move the magnet and thus the optic.

The hardest part to get right when using OSEMs is to properly diagonalize them so that you can push in the standard degrees of freedom (i.e. position, pitch, yaw, and side). This is accomplished in two steps, along with some sneaky meter-to-radian conversion.

First, we diagonalize the input matrix. An ideal input matrix should look like table 3. The input values are converted to micrometers before they get to this matrix. This matrix then converts the measurements to position and side measurements in μm and pitch and yaw measurements in μrad (the angular conversion is dependent on the fact that the magnets are mounted in a 4.94 by 4.94 cm square). Thus a change of $1\mu m$ the upper left (UL) sensor is counted as : $.25\mu m$ position, $-10.1\mu rad$ in pitch, $10.1\mu rad$ in yaw, and no change in side.

However, due to OSEM alignment, machining defects, suspension inaccuracy, etc. the ideal matrix is not the most effective. Thus, we have a method for diagonalizing

the matrices.

We drive one OSEM and look at the transfer function between that and all of the other OSEMs. We can determine from this the different modes (pos, pit, and yaw) by looking at the phase differences between the four back OSEMs (UL UR LL LR) at resonances. After this, we orthogonalize based on the coupling of each mode to the five osems. Here we have one interesting note: the position mode that we see is actually the pendulum mode, which is a combination of the pitch and position modes of the mass. The coupling scales inversely with the pendulum length.

Once we have the input matrix set, we diagonalize the output matrix. We close the loops and drive each degree of freedom with a slow signal, then measure the responses in each of the (properly diagonalized) sensors. We subtract out the drive to the not desired degrees of freedom to determine the output matrix.

UL	UR	LR	LL	SD	
.25	.25	.25	.25	0	position (μm)
-10.1	-10.1	10.1	10.1	0	pitch (μrad)
10.1	-10.1	-10.1	10.1	0	yaw (μrad)
0	0	0	0	1	side (μm)

Table 3 : Ideal input matrix. The sensor inputs (in μm) are multiplied by the coefficients to get position of the mass in two directions (position and side) and the orientation of the mass (pitch and side). The coefficient for the angular measurements is calculated from the distance (1.945 in) between the magnets mounted on the mass.

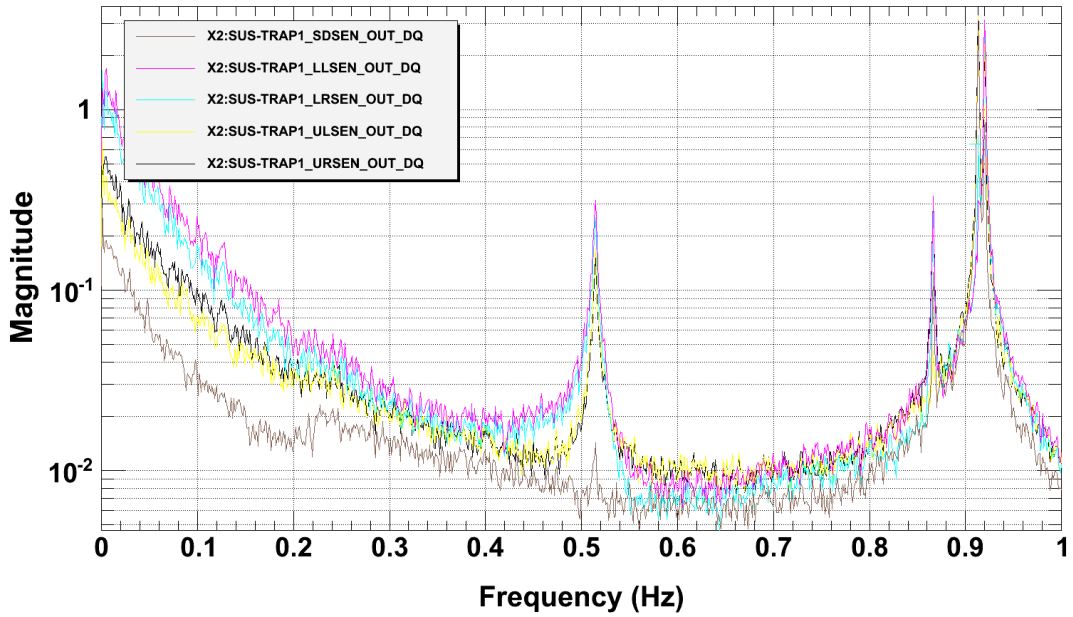

Figure 18 : Spectrum showing the modes of the input coupler. Modes from low to high are: Pitch (0.511 Hz), Yaw (0.866 Hz), Side (0.911 Hz), and Position (0.918 Hz).

Chapter 4

Control Loops

4.1 Subcarrier Servo

The subcarrier servo is designed to lock a VCO (voltage controlled oscillator) a set frequency away from a crystal oscillator. The is accomplished through two mixers and some feedback.

We use directional couplers to get the signals from both the 80 MHz crystal oscillator and the VCO so that the majority of the power is driving the AOMs, increasing the amount of optical power going into the first order mode, while only a small amount is lost to the feedback loop. The signal from the oscillator is mixed with the output of the VCO to produce a signal where the frequency is the difference between the two signals. This signal is then mixed with the desired offset frequency, set on the function generator, to give a low frequency error signal. The error signal is passed through some filters in the servo, then fed into the VCO frequency modulation input.

We typically monitor two spots in this system: The output of the fast mixer (ZMY-3) and the drive signal from the function generator (200 KHz on the diagram). When locked, the two should have the same frequency and be phase locked.

4.1.1 Method

We are going to look at the spectrum of the oscillators near 80 MHz to figure out the amount of frequency noise from these oscillators. We're mostly concerned with the frequency noise in the 1 KHz band around the peak.

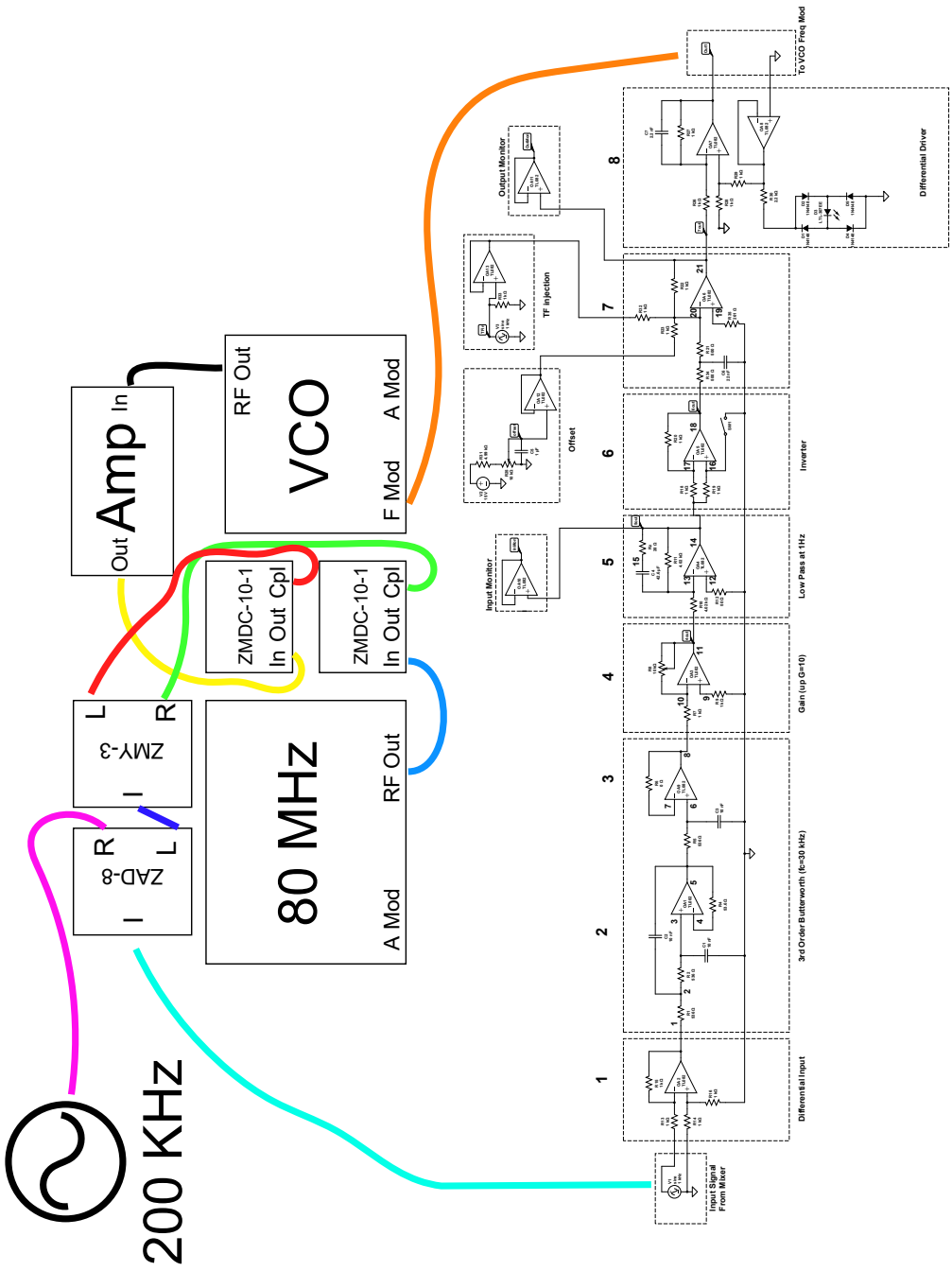

Figure 19 : Subcarrier Servo diagram. The servo locks the VCO output to the 80 MHz oscillator output, offset by the function generator. The function generator can be tuned from roughly 50 KHz to 2 MHz.

We begin by assuming that all voltage noise is phase noise (no change in the amplitude). This method gives an upper limit to the noise in the system.

ω_m is a measurement frequency. ω_c is the carrier frequency

$$V(t) = V_0 e^{i(\omega_c t + \phi(t))}$$

In the frequency domain,

$$\delta V(\omega_m) = V_0 \delta\phi(\omega_m) = \frac{2\pi V_0}{\omega_m} \delta f(\omega_m)$$

Keep in mind that to do this properly, you need to sum the effects of the noise at the carrier plus 1 KHz and the carrier minus 1 KHz.

$$\delta f(\omega_m) = \frac{\omega_m \delta V(\omega_m)}{2\pi V_0}$$

We can now calculate the effect of this frequency noisee on our optical trap cavity. f_L is the laser frequency.

$$\delta x = \frac{L}{f_L} \delta f = 2.66 \times 10^{-16} \delta f$$

The noise budget gives a noise floor of 10^{-17}, so to get in under that, we need a $\delta f << \frac{1}{26.6}$

4.1.2 Results

With the subcarrier servo locked at approximately 200 KHz, the noises we measure are:

80 MHz Oscillator: frequency noise $5.4 \times 10^{-3} \frac{Hz}{\sqrt{Hz}}$. Position noise $1.4^{-18} \frac{m}{\sqrt{Hz}}$.

VCO: frequency noise $6.7 \times 10^{-2} \frac{Hz}{\sqrt{Hz}}$. Position noise $1.7^{-17} \frac{m}{\sqrt{Hz}}$.

These noise values are OK for the 80 MHz oscillator, but not so much for the VCO. We suspect that the 200 KHz oscillator may be the culprit.

4.2 Loops

Here's a picture of the longitudinal trap as it stands. In general terms, we have a cavity with position and laser feedback, which also has optical spring behavior. Analog and digital loops are shown in figures 22 and 23.

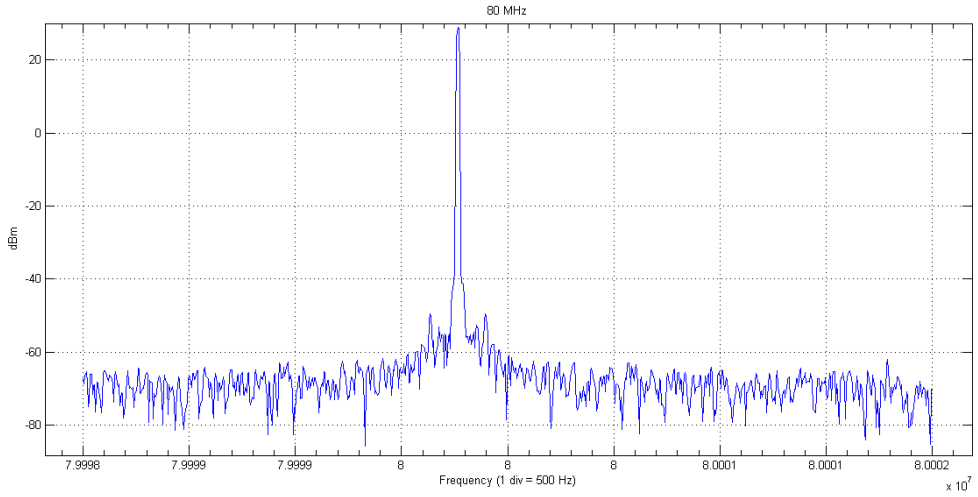

Figure 20 : Spectrum of the 80 MHz crystal oscillator around 80 MHz

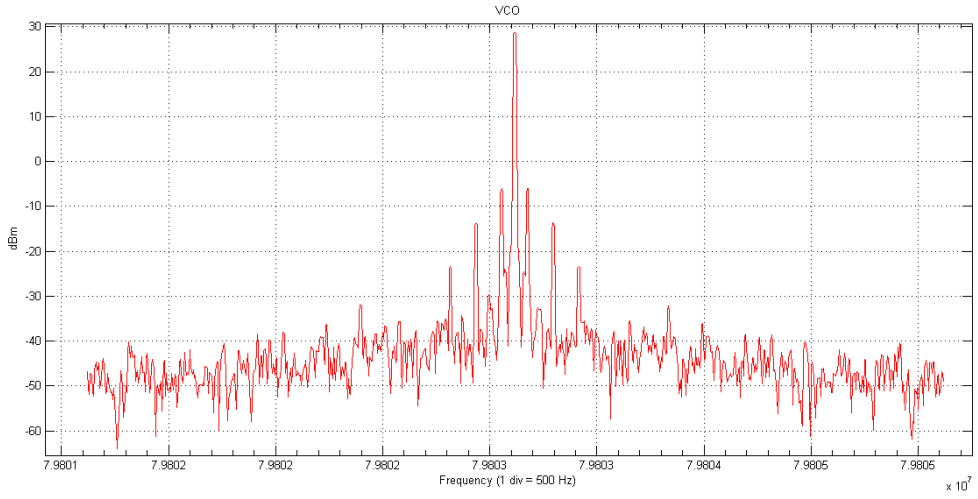

Figure 21 : Spectrum of the locked VCO. The sidebands are likely caused by the function generator.

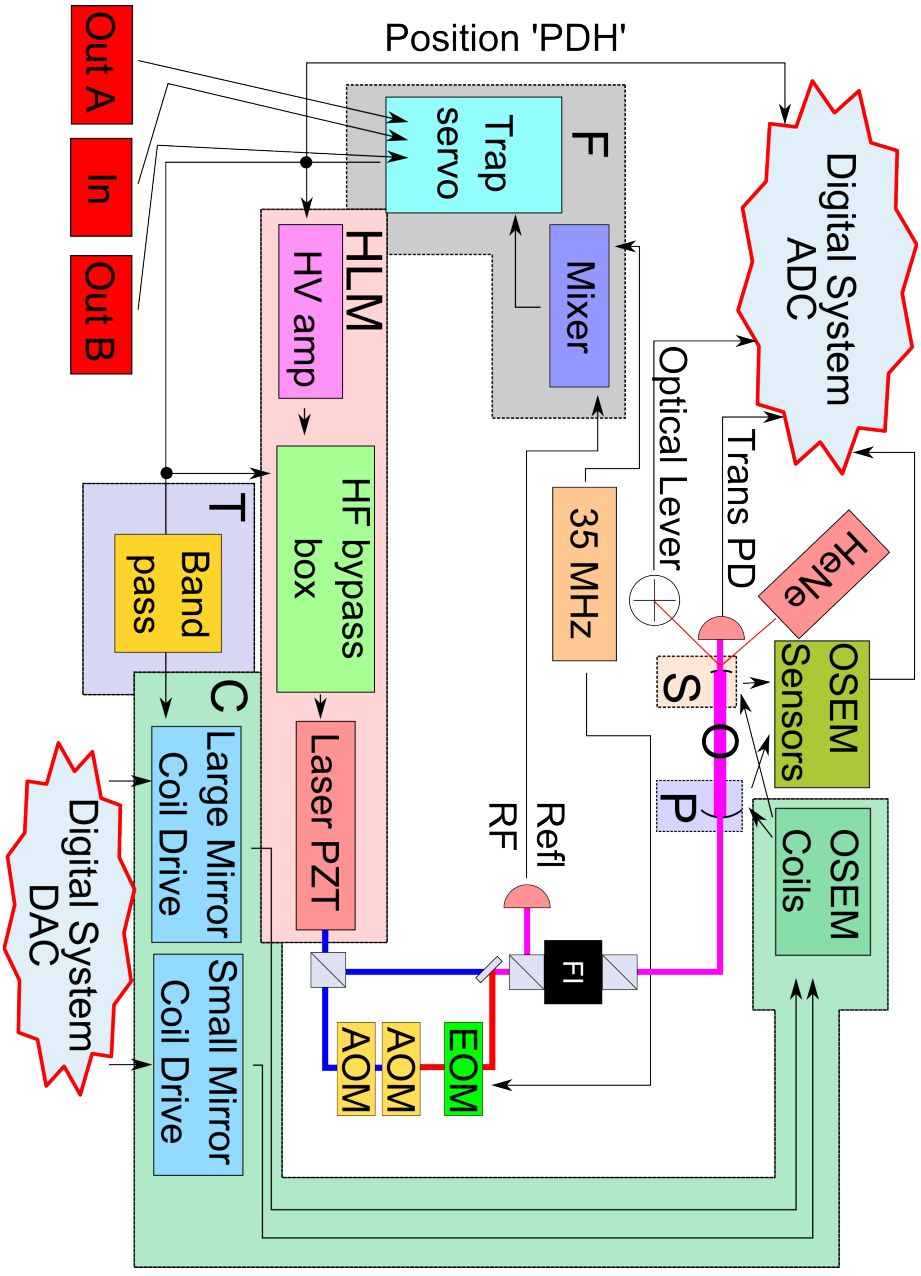

Figure 22 : Analog parts of the locking loop.

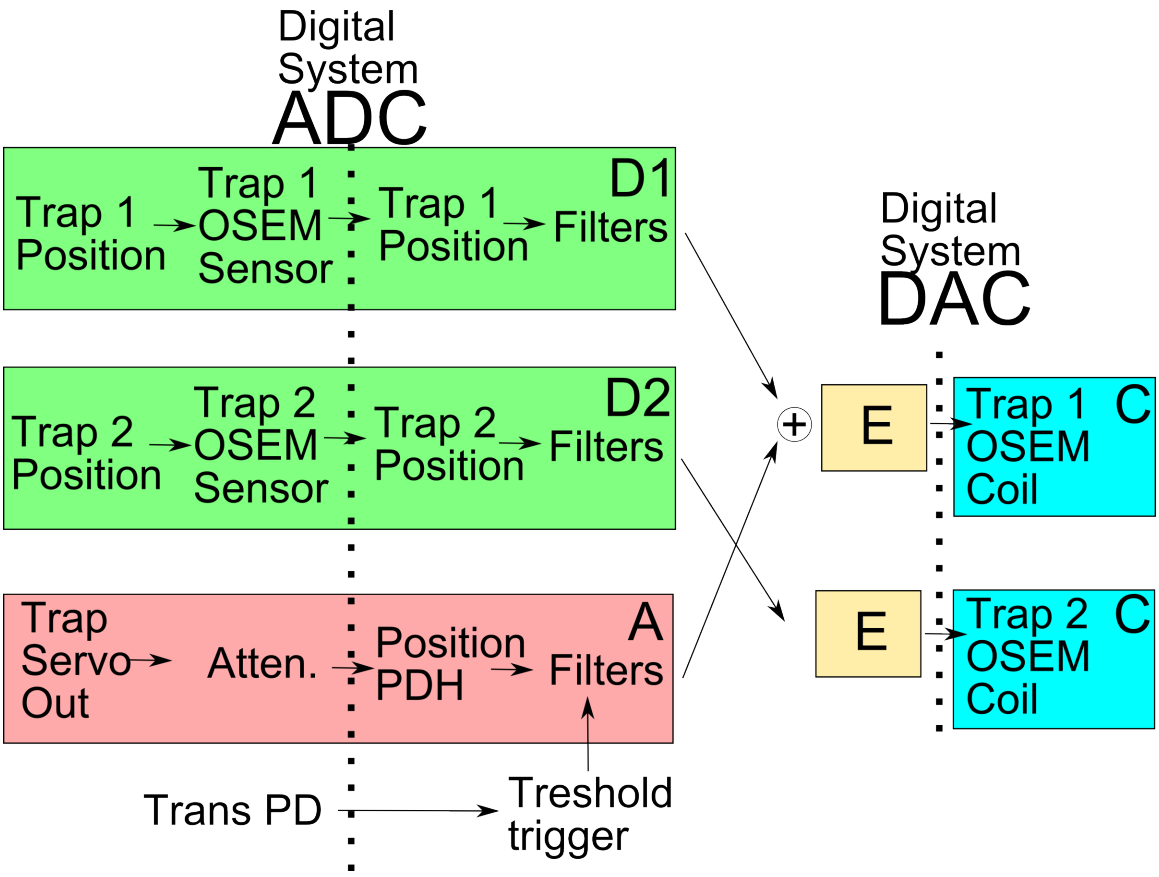

Figure 23 : Digital parts of the locking loop. The yaw and optical lever inputs are not relevant to the longitudinal trap.

You may notice that this layout drawing has an alphabet soup of sections and subsections. I will now describe in excruciating detail what each of these things are and why we care. I am leaving out the input whitening in analog land and the dewhitening in digital land. They should cancel out every time, so we just leave them off. I started drawing in angular control loops, but I won't be addressing them here.

Our goal is to be able to reconstruct the entire optical trap from the control point to the error signal. In our measurements, we are using the injection input and the two test outputs of the Trap Servo board. Test out A serves as our error signal (OUT) and Test out B serves as our control signal (IN). The injection happens between the two test outputs. The resulting open loop transfer function is (plotted in figure 25)

This is based on Jim's model of the loop, which I have updated and repackaged.

$$\left[FHLM + \frac{FAECP + FTCP}{1 + PCED}\right] \frac{1}{1 + SO} \tag{4.1}$$

There are several diffent parts to this equation, so we will take a moment to look each term. Every term in the numerator includes F, the Trap Servo. $FHLM$ is a loop involving the PZT drive of the laser. $FAECP$ and $FTCP$ both rely on pushing the large mass around using the OSEM drive, but $FAECP$ does the drive through the digital system while $FTCP$ uses an analog connection. $1 + PCED$ is the closed loop of the active suspension damping for the large mass; note that this only affects the loops that are driving the large mass. $1 + SO$ is the closed loop system of the optical spring, which is dependent on the seperation between the two mirrors, rather than the absolute position of either.

4.2.1 A

At the moment, this path has been disconnected, because it was not required. Thus we can set $A = 0$.

4.2.2 C

Converts voltage from the DAC into force on the large mirror via the OSEMs. Factor of 4 because we have 4 OSEMs. Number comes from logbook 439.

$$C = \frac{4}{4.91793 \times 10^4 \mathrm{V/N}} \tag{4.2}$$

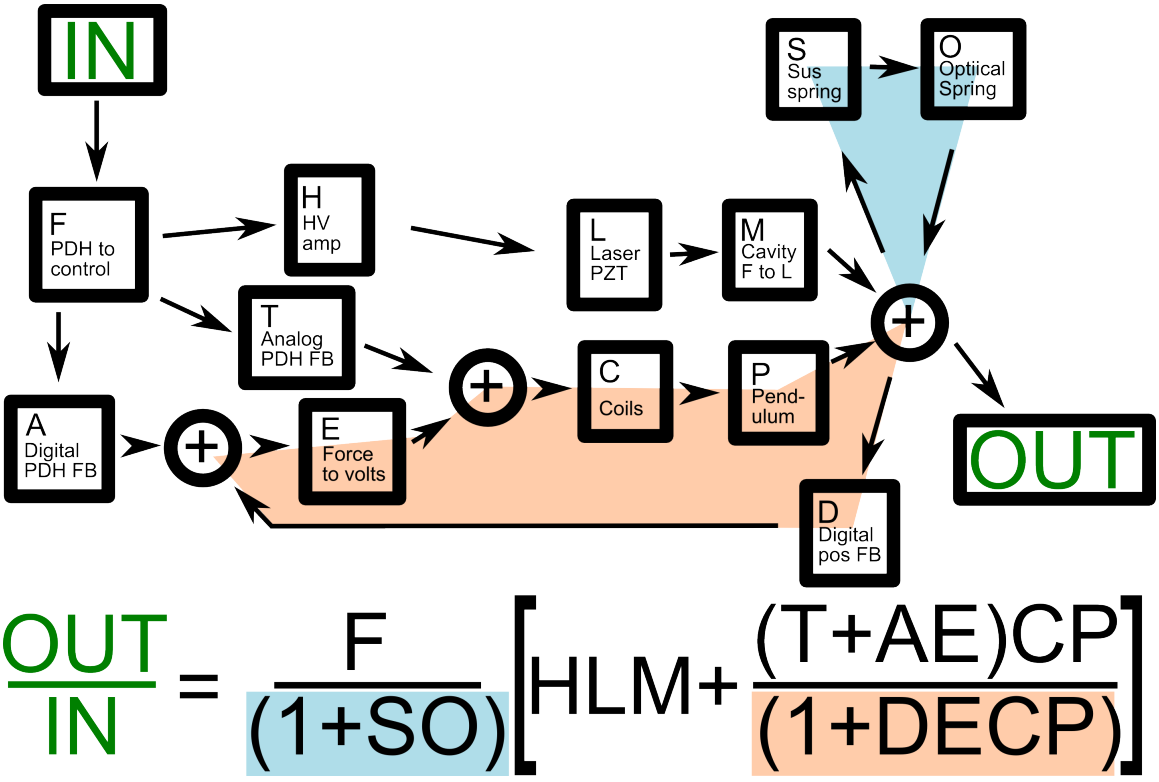

Figure 24 : Block diagram of the open loop TF

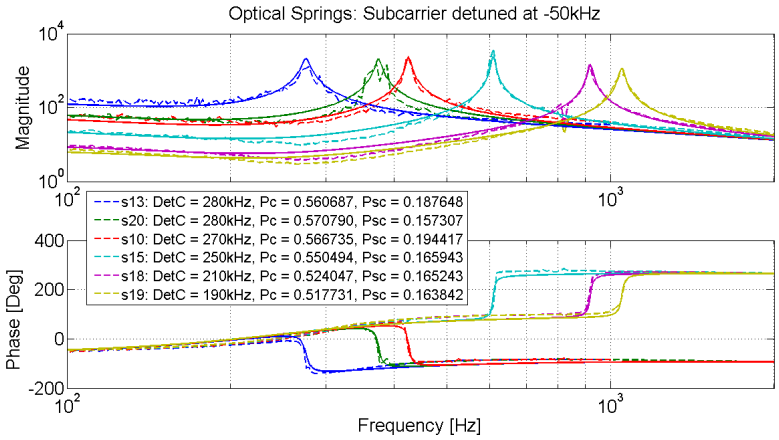

Figure 25 : Open loop TF of several springs, measured vs. modeled.

4.2.3 D1 and D2

The input to each of these blocks the motion of a single optic relative to the OSEMs. The OSEMs put out a current proportional to the position of the mass, which is digitized. The output is a drive signal which gets added into the OSEM drive of trap 1 and trap 2, respectively. The position measurements from each optic have filters applied from the TRAP1_SUSPOS and TRAP2_SUSPOS filter banks. In D1, we have an AC coupling filter(Z: 0, P: 0.5), a highpass (Z: 1, P: 100), and a fourth order Chebychev lowpass filter at 200Hz with 1dB of passband ripple (P: $67.3977 \pm \imath 81.4946$, $27.9074 \pm \imath 196.677$ G: -0.891251). There is also a gain of 10, which includes the filter gain, the conversion of position of the optics relative to the OSEMs into voltage, and the conversion from volts to meters in the digital system. See fig. 26.

From the Matlab code:

```
tf = (1i*freq - 0) .* (1i*freq - 1)...
    ./ (1 + 1i*freq / 0.5)...
    ./ (1 + 1i*freq / 100)...
    ./ (1 + 1i*freq / (67.3977+1i*81.4946))...
    ./ (1 + 1i*freq / (67.3977-1i*81.4946))...
    ./ (1 + 1i*freq / (27.9074+1i*196.677))...
    ./ (1 + 1i*freq / (27.9074-1i*196.677))...
    .* -0.891251...
    .* Dgain;
```

Why don't we consider the effects of D2? Because we are not putting any active drive through it. Thus it will not shape the loop as drastically as D1. The coupling between the mirror position and the ring position drop off drastically (f^{-2}) above the position resonance of the glass suspension ($\approx$ 18Hz). As we improve the lock, we expect that we will be able to reduce or even remove active feedback on the ring.

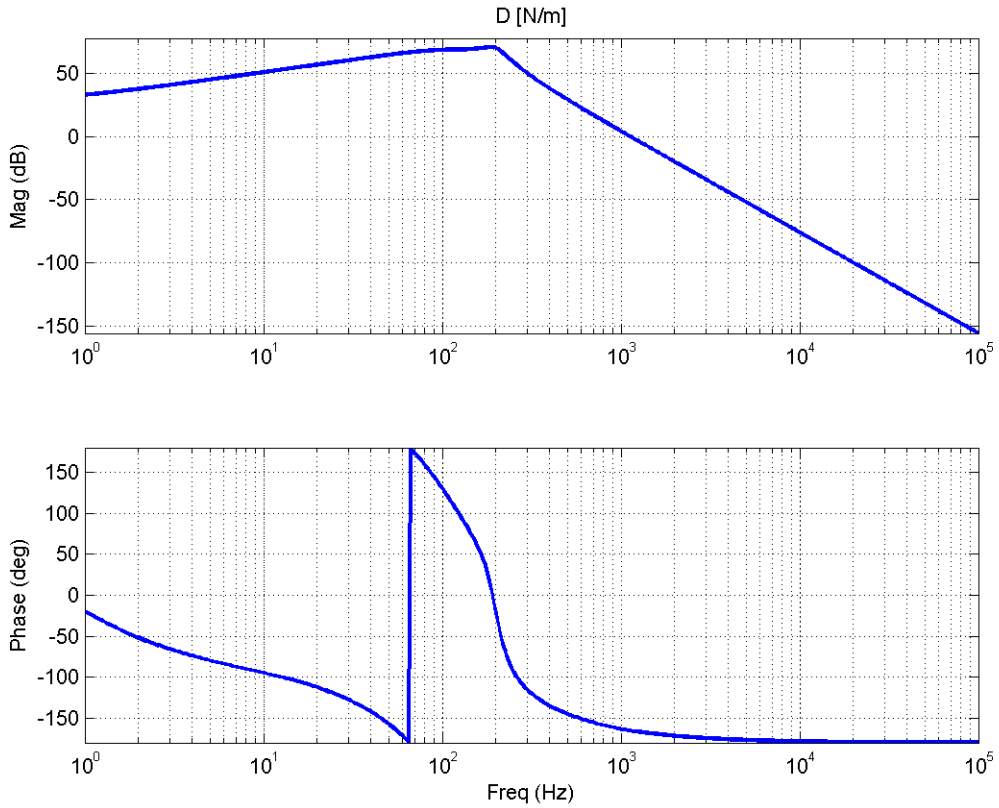

Figure 26 : D1, the transfer function from the position of optic 1, the input coupler, to a digital drive force.

4.2.4 E

Converts force output of digital filters into volts so that you can send it out of the digital system. Factor of 4 because we have 4 OSEMs. Note that $CE = 1$.

$$E = \frac{1}{4} 4.91793 \times 10^4 \text{V/N} \tag{4.3}$$

4.2.5 F

This is the transfer function of the Trap Servo, the RF photodiode, and the mixer. Input to this is the cavity length, read out through the PDH method. The output is a voltage. The variable 'mxrpd,' which is the conversion from cavity length to the voltage output of the mixer, is dependent on power, cavity mode matching, and the PDH readout at the mixer. mxrpd, measured at full power, just below the oscillation point, is about 10^9 V/m. See fig. 27. At the moment, we are only using the 100Hz integrator. This has been modeled completely with the 'Analog' library in /software/matlab/analog.

4.2.6 P

Pendulum of the large mass. Converts a force to a displacement in the position direction. Resonant frequency $f_L = 1.4$Hz. Large mass $m_L = 300$g.

$$P = \frac{1}{m_L (2\pi f_L)^2} \frac{1}{\left(1 - \left[\frac{f}{f_L}\right]^2\right)} \tag{4.4}$$

4.2.7 S

The glass suspension connects the small optic to the ring; it acts as a high-Q spring. An optical lever is used to damp oscillation modes other than the position mode. It converts a force to a displacement in the position direction. Resonant frequency $f_s = 18$Hz. Small mass $m_s = 0.5$g.

$$S = \frac{1}{m_s (2\pi f_s)^2} \frac{1}{\left(1 - \left[\frac{f}{f_s}\right]^2\right)} \tag{4.5}$$

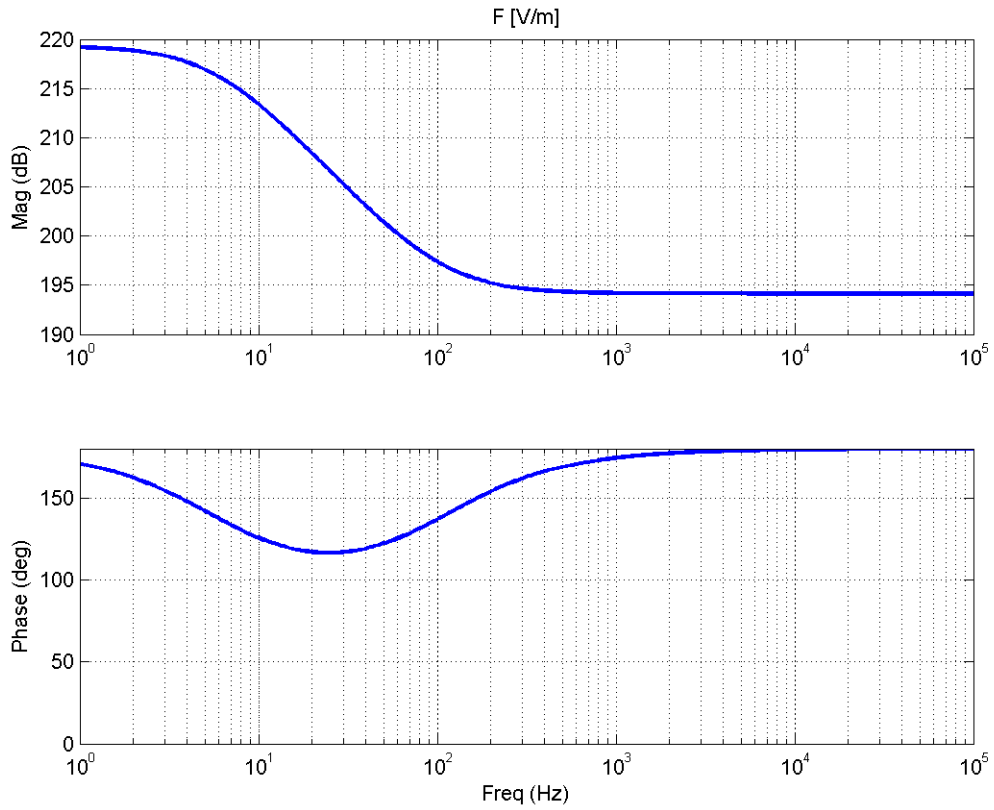

Figure 27 : Calculated trap servo TF

4.2.8 O

Optical spring! Depending on detunings and power ratio, we should get stable or unstable behavior. Plotted in figure 29. We should note that optical losses before the cavity have to be considered when determining the power in the cavity, as well as the cavity detuning and angular displacements of the mirrors. At the moment we are calculating this using Finesse.

Combining this spring constant with S in a closed loop gives us the behaviour of the optical spring on the small mass, and thus cavity length. Below, in equation 4.6, is the effect of the optical and mechanical springs on changes in the cavity length.

$$\frac{1}{1+OS} = \frac{k_m - m\omega^2}{k_m + k_{os} - m\omega^2} \tag{4.6}$$

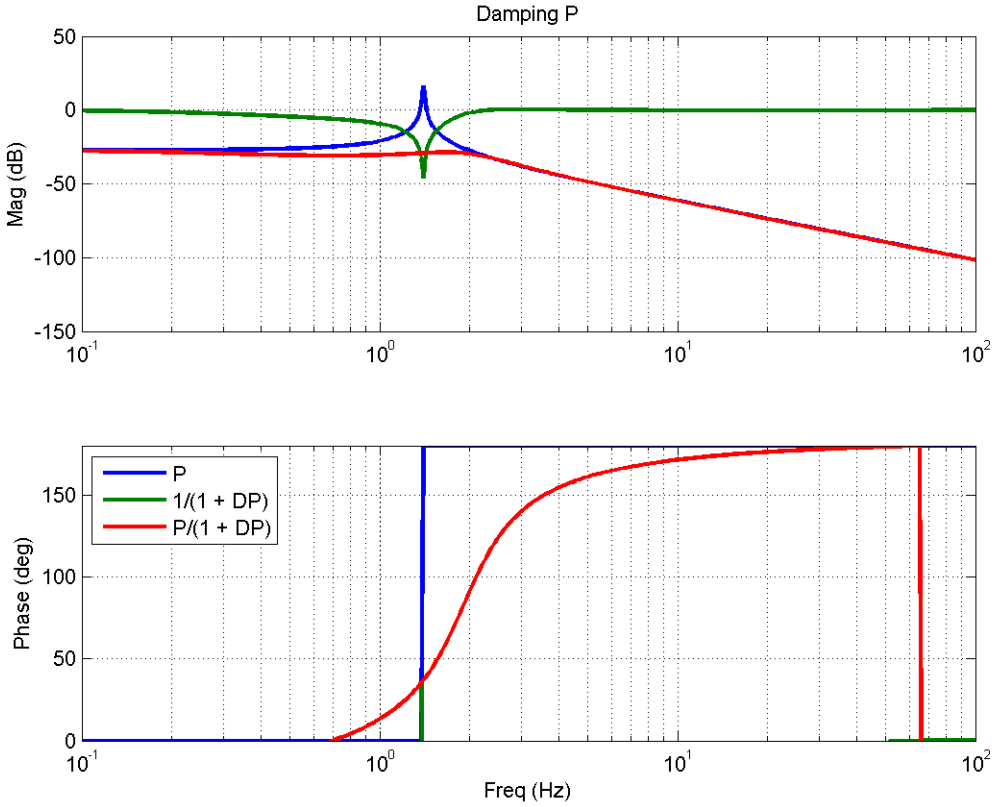

Figure 28 : Damped large mass pendulum

4.2.9 L

Laser PZT. Converts a voltage to a shift in the laser frequency. From product spec sheet.

$$L = -1.7 \times 10^{6} \text{Hz/V} \tag{4.7}$$

4.2.10 M

Cavity. Small change in laser frequency can be converted into a small change in cavity length. Cavity length $l = 0.07$m

$$M = \frac{l\lambda_0}{c} \tag{4.8}$$

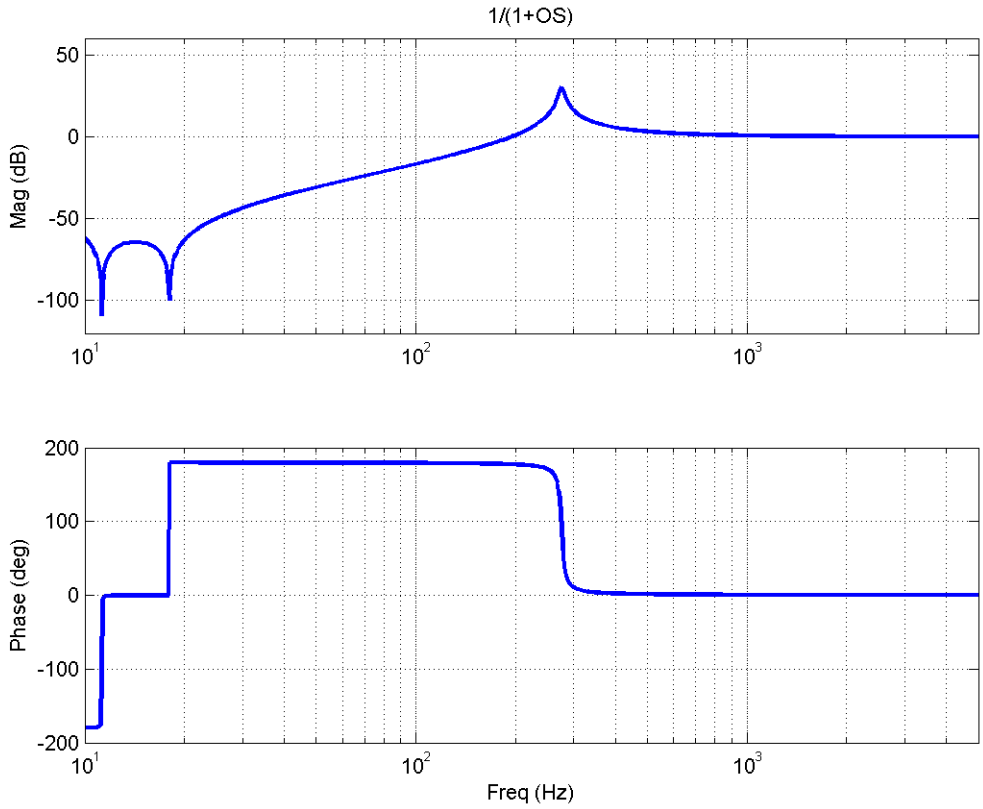

Figure 29 : Plot of the closed loop behavior of the spring doing springy things. The 1 Hz resonance should probably be suppressed by the digital system damping loop

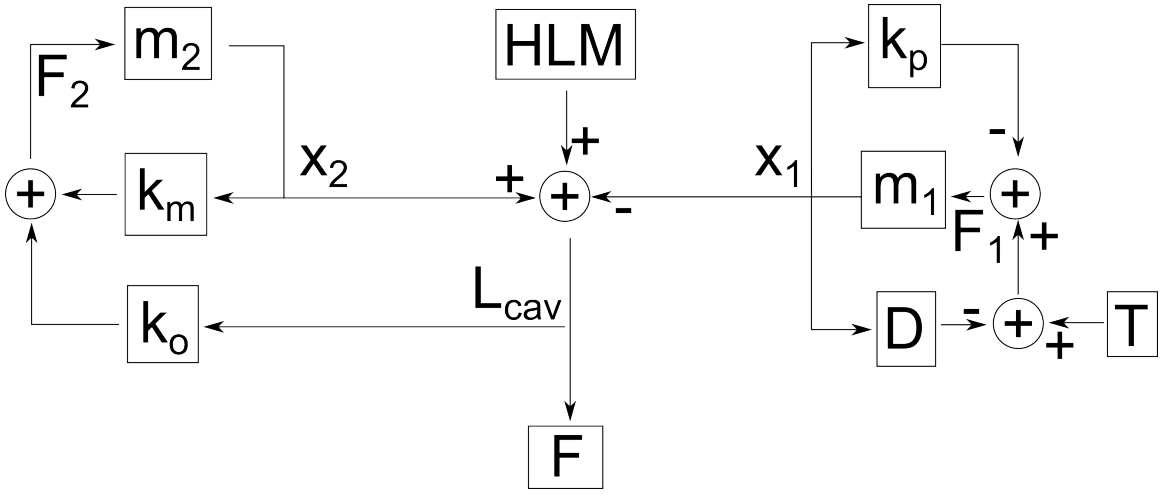

Figure 30 : Those blocks demonstrate WHY we can simply multiply the loop TF by the CLG of the optical spring

4.2.11 H

HV amplifier (with HV bypass) from measurement. See fig. 31. The HV bypass is described in ALog 412. The overall behavior of the amplifier and the bypass is designed to look like this simplified model:

$$H = \frac{70}{1 + if/146} \tag{4.9}$$

We actually interpolate the data for this block, so that we don't run into trouble in the discrepancy region.

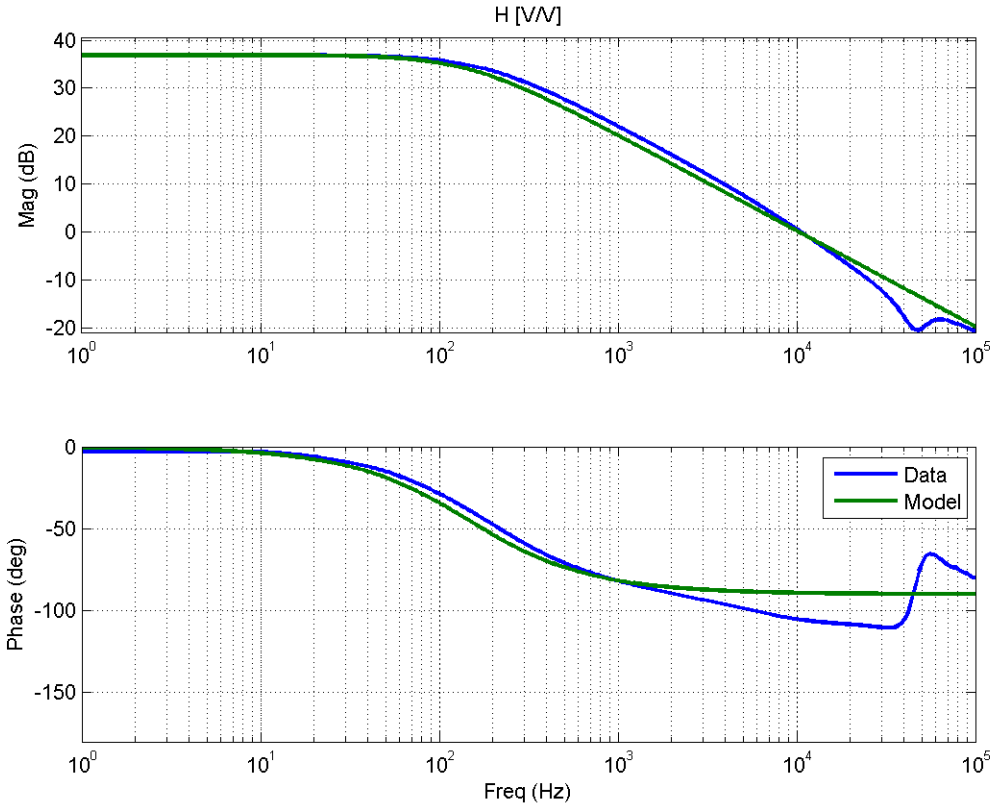

Figure 31 : H transfer function

4.2.12 T

This is a SR560 that operates between the Trap Servo control signal and the analog drive for the large optic OSEMs.

It is currently set to a 1KHz 6db lowpass with a gain of 200, so it is modeled as

$$T = \frac{200}{1 - \imath f/1\text{KHz}} \tag{4.10}$$

4.3 Photothermal effect on loops

The photothermal effect is directly related to how close the cavity is to resonance. This is affected by the total cavity length and the frequency of the light entering the cavity. In figure 32, we see that the photothermal effect (Pt) can be treated as a closed loop acting on the cavity length L_{cav}.

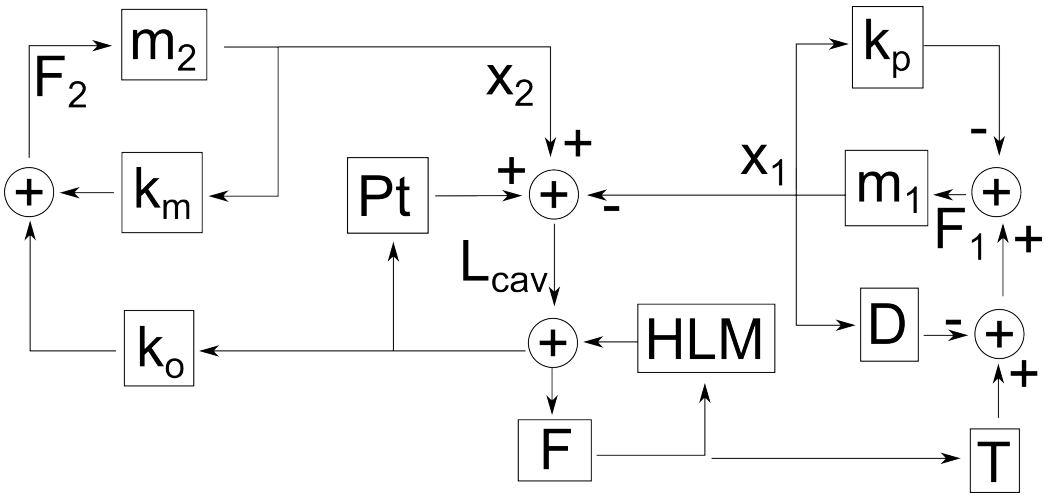

Figure 32 : Loop diagram for a single degree of freedom, including photothermal feedback, Pt.

Chapter 5

Photothermal Effect (from paper)

5.1 Introduction

The Advanced Laser Interferometer Gravitational-Wave Observatory (aLIGO) [35], together with its international partners Virgo [36] and KAGRA [37], aim to directly observe gravitational waves emitted by astrophysical sources such as coalescencing of black hole and neutron star binary systems. The installation of the Advanced LIGO detectors is completed, and commissioning towards the the first observation run is ongoing. Preliminary astrophysical data is expected in 2015. The sensitivity of those advanced gravitational-wave detectors in the observation band is limited by the quantum noise of light and the thermal noise associated with mirror coatings. A contributor to the thermal noise, expected to dominate in future cryogenic gravitational-wave detectors, is thermo-optic noise [38, 39, 40]. It is caused by dissipation through thermal diffusion.

The same physics also leads to an intensity noise coupling, known in the literature as photo-thermal effect [41]. The low frequency behaviour of the photo-thermal effect was predicted in [39] and experimentally measured in a Fabry-Perot cavity by De Rosa et. al. [42]. The physics relevant for the the high frequency behaviour, dominated by the details of the coating, was investigated in [40] in the context of studying thermo-optic noise. It was extended to a full model of the photo-thermal transfer function in [43]. Here we explore the thermo-optic effect in the context of an optical spring. The coupling acts as an additional feed-back path. The phase of the coupling becomes important and can directly affect the stability of the optical spring resonance. We can

exploit this dependence for a precision measurement of the photo-thermal coupling, even if it is driven by the residual few-ppm absorption of a high-quality optic.

The desire to lower the quantum noise in the gravitational-wave observation band has driven the power circulating in the Advanced LIGO arm cavities up to about 800 kW. The high laser power, in turn, couples the angular suspension modes of the two cavity mirrors. This Sidles-Sigg instability [17] creates a soft (unstable) and a hard mode, whose frequency increases with the intra-cavity power. The detector's angular control system must control the soft and damp the hard mode, and at the same time must not contaminate the observation band, starting at 10 Hz in the case of Advanced LIGO. Future gravitational wave detectors aim to extend the observational band to even lower frequencies, further aggravating this limitation. We previously proposed a model [44] to overcome the angular instabilities, based on a dual-carrier optical spring scheme demonstrated by Corbitt et al., in 2007 at the LIGO laboratory [15]. The proposed angular trap setup uses two dual-carrier beams to illuminate two suspended optical cavities which share a single end mirror. As first step towards the experimental demonstration of the scheme we built and operated a prototype, single-cavity optical trap, capable of controlling the cavity length only [45]. The data presented in this paper was taken with this prototype. The next version of the angular trap setup will also allow us to measure the photo-thermal effect on a folding mirror. Heinert et. al. [46] predicted excess thermal noise for folding mirrors due to transverse heat diffusion. The result has not yet been experimentally confirmed, but since the same physics will also lead to an enhanced photo-thermal transfer function, the prediction can be verified with a photo-thermal transfer function measurement.

The paper is structured as follows: Sections 5.2 and 5.3 will review the idea of a dual-carrier optical spring and the photo-thermal effect respectively. Section 5.4 describes the experimental setup and we discuss the result in section 5.5. Finally, section 5.6 suggests a coating modification to make a single-carrier optical spring feasable.

5.2 Dual-carrier optical spring

A Fabry-Perot cavity detuned from resonance couples the intra-cavity power linearly to the mirror position. The response is delayed by the cavity storage time. The

resulting optical spring constant is given by [44].

$$K_{OS}^{\text{1field}} \approx K_0 \frac{1}{1+\frac{\delta^2}{\gamma^2}-\frac{\Omega^2}{\gamma^2}+i2\frac{\Omega}{\gamma}} \tag{5.1}$$

$$K_0 = P_0 t_1^2 r_2^2 \frac{8kr_1r_2}{c(1-r_1r_2)^3} \frac{\frac{\delta}{\gamma}}{(1+\frac{\delta^2}{\gamma^2})} \tag{5.2}$$

where P_0 is the incident power, corrected for mode-matching losses, $k = 2\pi/\lambda$ is the wave vector of the light, t_i and r_i are the mirror amplitude transmissivity and reflectivity for input coupler ($i = 1$) and end mirror ($i = 2$), and γ, δ and Ω are the cavity line, cavity detuning, and mechanical frequency. The value of K_{OS} lies in either the 2nd or 4th quadrant of the complex plane, and the associated radiation pressure force creates either a anti-restoring and damping (red detuning) or a restoring and anti-damping force (blue detuning) [14].

Two spatially overlapping optical fields, the carrier and sub-carrier, with opposite detuning sign and with an opportune power ratio can be used to cancel the instability [15]. The total optical spring K_{OS} is the sum of the individual springs

$$K_{OS} = K_{OS}^{c} + K_{OS}^{sc} \tag{5.3}$$

Where K_{OS}^{c} and K_{OS}^{sc} are given by equation 5.1. The dual-carrier optical spring can be tuned to lie in the 1st quadrant for the frequency band of interest. When acting on a suspended cavity end mirror with mass m and mechanical suspension spring constant K_m the optical spring becomes a feed-back loop with a closed loop response function

$$\frac{x}{F_{ext}} = \frac{1}{-m\Omega^2 + K_m + K_{OS}} \tag{5.4}$$

The tunability of the optical spring K_{OS} in both magnitude and phase allows experimental fine-tuning of the poles of equation 5.4 to lie exactly on the real axis, resulting in an infinite Q of the optical spring (critical stablility). Experimentally this can be done up to a maximum Q, above which the measured transfer function data no longer permits distinguishing between a stable and an unstable spring. The phase of the total spring constant at resonance can then be determined with a precision given by $1/Q$. The suspension mechanical spring constant has to have a positive imaginary part, but it can be designed to be very small. Loss angles of 10^{-5} are easily

achievable, and are further diluted by the magnitude of the ratio of K_{OS}/K_m. The contribution to the phase of the total spring constant from the mechanical suspension is thus expected to be negligible. The imaginary part of the optical spring K_{OS} on the other hand is closely related to its real part through equations 5.3 and 5.1, and is very accurately predicted based on the resonance frequency, carrier to sub-carrier power ratio as well as the detuning of carrier and subcarrier, i.e. only power ratios and frequencies. As a result, any deviation in phase from the expectation of equation 5.1 around the optical spring resonance is easily and repeatably observable with a precision given by the inverse of the experimentally resolvable Q, and an accuracy determined only by frequency and power ratio measurements.

5.3 Photo-thermal effect

Power absorption on the surface of an optic leads to an increase of the surface temperature. The depth of the heated layer is given by the diffusion length $d_{\text{diff}} = \sqrt{\kappa/(\rho C \Omega)}$, where κ, C and ρ are the thermal conductivity, heat capacity and density of the material, and Ω is the observation angular frequency. In the large-spot size limit, i.e. $\mathrm{w} \gg d_{\text{diff}}$, and neglecting coating effects, the displacement of the surface is given by (e.g. [39, 43])

$$\triangle z = \bar{\alpha} \int_0^\infty T dz = \bar{\alpha} \frac{j}{i\Omega\rho C} \tag{5.5}$$

where $\bar{\alpha} = 2(1+\sigma)\alpha$ is the effective expansion coefficient under the mechanical constraint that the heated spot is part of a much larger optic [40, 47]. α and σ are the regular linear expansion coefficient and Poisson ratio. $j = P/(\pi \mathrm{w}^2)$ is the absorbed average surface intensity of the Gaussian beam with beam radius w ($1/e^2$ intensity). This simple picture needs two important refinements. First, for frequencies Ω around and below $\Omega_c = 2\kappa/(\rho C \mathrm{w}^2)$ the transverse heat diffusion leads to a multiplicative correction factor to equation 5.5 derived by Cerdonio et al. [39]:

$$I(\Omega/\Omega_c) = \frac{1}{\pi} \int_0^\infty du \int_{-\infty}^\infty dv \frac{u^2 e^{-u^2/2}}{(u^2+v^2)\left(1 + \frac{(u^2+v^2)}{i\Omega/\Omega_c}\right)} \tag{5.6}$$

As expected, for $\Omega \gg \Omega_c$, the correction factor approches 1. For a fused Silica substrate, SiO_2, and a Gaussian beam spot radius of $\mathrm{w} = 161$ μm this correction

becomes large below $\Omega_c/(2\pi) = 10$ Hz, but is measurably different from unity even at 1 kHz. (See fig 33)

Second, for high frequencies, the diffusion length becomes comparable to the coating thickness. Since the optical field is reflected by a dielectric stack, the effective mirror displacement is given by [40, 43]

$$\triangle z = \sum_i \left[\frac{\partial \phi_c}{\partial \phi_i} (\beta_i + \bar{\alpha}_i n_i) + \bar{\alpha}_i \right] \bar{T}_i d_i \tag{5.7}$$

where $\bar{\alpha}_i$, $\beta_i = dn/dT$ and n_i are the constrained effective expansion coefficient, the temperature dependence of the index of refraction, and the index of refraction itself for layer i. $\frac{\partial \phi_c}{\partial \phi_i}$, the dependence of the coating reflected phase on the round trip optical phase in layer i, is always negative, resulting in a sign change and enhancement of the bracket in equation 5.7 for the first few layers. $\bar{T}_i d_i$ is the temperature profile driven by the absorped intensity j, integrated across layer i. For a $Ta_2O_5 : SiO_2$ coating used in gravitational wave detectors we find a measureable enhancement of the photo-thermal transfer function around 1 kHz [43]. Additionally, depending on the detailed absorption profile, a sign change can occur above about 100 kHz.

For the experiment parameters discussed in this paper, i.e. a Gaussian beam spot radius of w = 161 μm and a mirror coating with about 13 doublet layers both effects are relevant in the 100 Hz to 1 kHz band. Their contributions are plotted in figure 33.

5.4 Experimental setup

5.4.1 Cavity

The optical spring cavity is composed of two suspended mirrors in a vacuum chamber, each with radius of curvature RoC = 5 cm and power transmissivity $T = 4.18 \times 10^{-4}$. The measured finesse is 7500±250 and the cavity length is $L_0 = 7.0 \pm 0.2$ cm. We chose a short cavity to minimize frequency noise coupling. The cavity has a free spectral range (FSR) of about 2.14 GHz and cavity pole $f_{pole} = \gamma/(2\pi) = 143$ kHz. The input mirror mass is 300 g, designed to be heavy to make it insensitive to radiation pressure; it is suspended as a single stage pendulum with mechanical resonances, i.e. position, pitch and yaw, close to 1 Hz. The end mirror has a mass of 0.41 ± 0.01 g and is

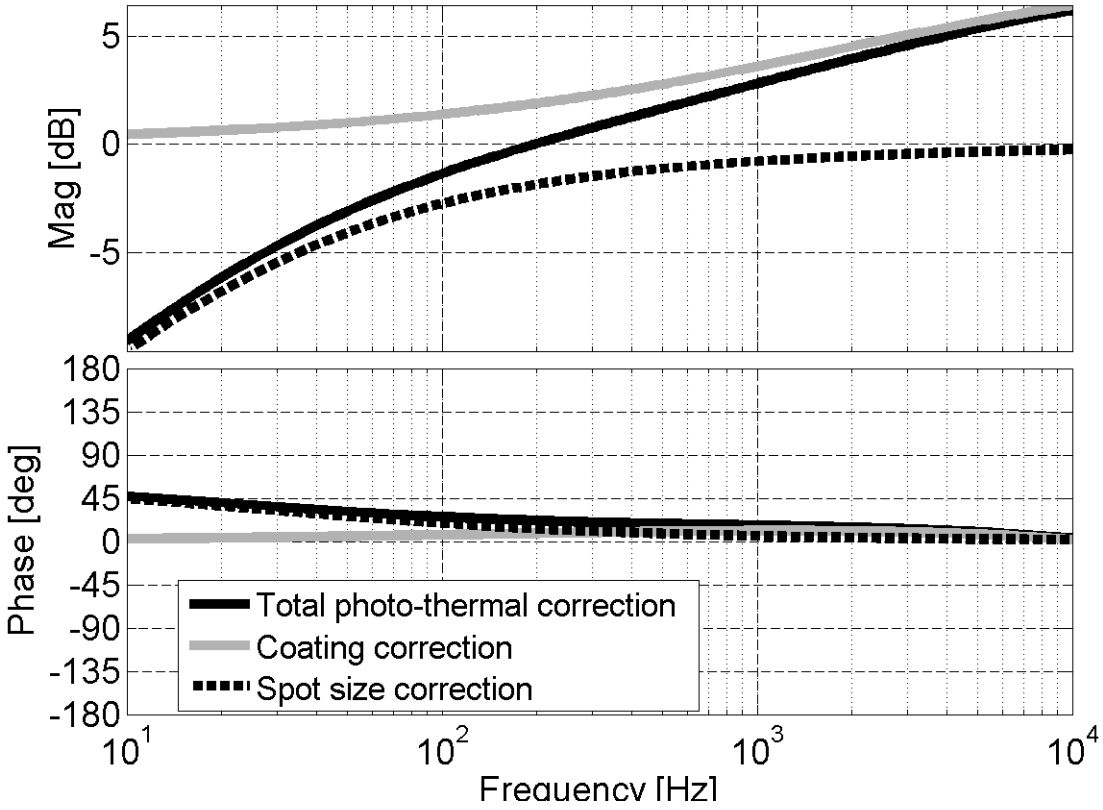

Figure 33 : Correction factors for the photo-thermal transfer function of a fused silica mirror with a dielectric coating (solid black). The solid grey trace is the coating correction for a 13-doublet $\lambda/4$ coating. The dashed black trace shows the effect of a Gaussian beam spot with w = 161 μm radius. To get the full transfer function, multiply with equation 5.5, adding an overall $1/f$ shape. The calculation is based on material parameters show in table 5.

λ_0	1064 nm
Mirror RoC	5.0 cm
L_0	7.0 cm
Spot size	161 μm
FSR	2.14 GHz
Finesse	7500
Cavity Pole	143 KHz

δf_C	213-290 KHz
δf_{SC}	27-36 KHz
P_C input	225-239 mW
P_{SC} input	65-78 mW

Table 4 : Parameters of the optical spring cavity. The range of values for the carrier and sub-carrier detuning frequency (δf_C, δf_{SC}) and input power (P_C, P_{SC}) indicate the variation between individual measurements.

7.75 mm in diameter. It is suspended with three glass fibers from a 300 g steel ring, shown in figure 34. The steel ring has diameter of 7.6 cm and is itself suspended. The input mirror is actively controlled by an electronic feedback system, while the end mirror is free to move in the glass suspension abobe its resonance frequency of 18 Hz, and is only subject to the optical spring radiation pressure.

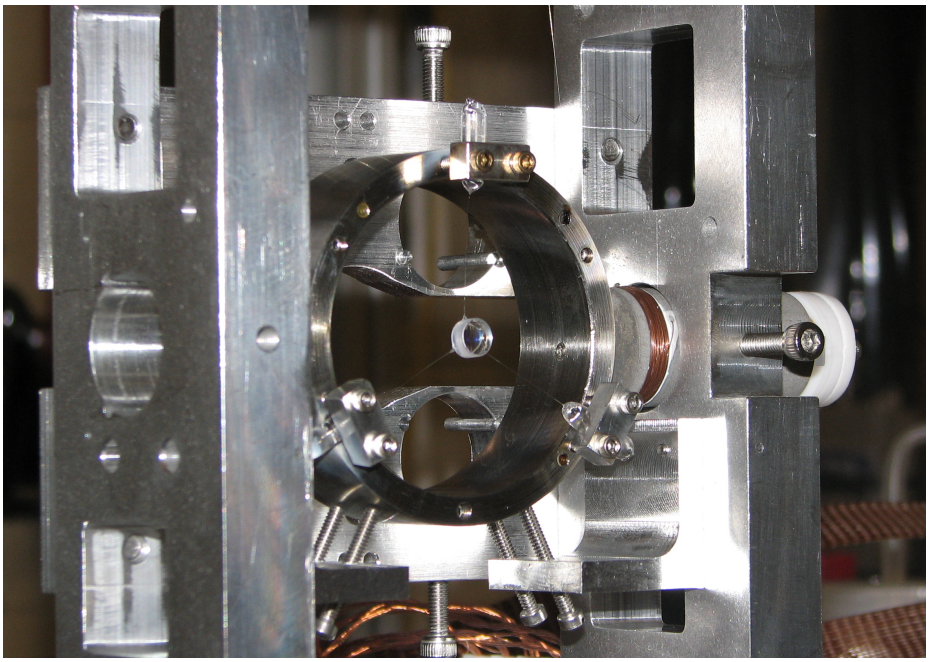

Figure 34 : A picture of the small end mirror suspended from a steel ring by glass fibers. The ring is suspended from a small optics suspension (SOS) with tungsten wire. The SOS provides DC alignment control while allowing the mirror to move freely above the 18Hz resonance of the fiber suspension. The end of the fiber is a small glass nub attached to the mirror with epoxy. This produces a fairly high suspension Q of about $5 \cdot 10^5$. The resulting contribution of damping in the opto-mechanical spring is insignificant compared to the damping from the optical field.

5.4.2 Input field preparation

The optical field incident on the optical spring cavity consists of two beams, a carrier and a subcarrier, as described in Section 5.2. As shown in figure 35, a 1064 nm laser is split into a carrier and a subcarrier beam at the polarizing beam splitter PBS1. In the subcarrier path two acoustic optic modulators (AOMs) are used to impose a relative frequency shift Δ, on the subcarrier beam, leaving it at a set detuning from the carrier beam. Δ is set using an external signal generator (see Sec. 5.4.3). The two

beams recombine at PBS2 and proceed towards the Fabry-Perot cavity with opposite polarization. The total power and the power ratio between the carrier and subcarrier beams are set by two half wave-plates $\lambda/2$.

The subcarrier beam is modulated by a 35 MHz electro-optic modulator (EOM). We measure the modulated light reflected by the cavity with a resonant radio-frequency photodiode (RFPD) and then demodulate to read out the cavity length with the Pound-Drever-Hall technique (PDH) [33]. We use the subcarrier to derive a PDH singal because the subcarrier requires less detuning than the carrier. We can use the PDH signal to actuate on the laser and the suspensions to lock the cavity, then turn down the gain and use the PDH signal for readout.

A small offset added to the PDH error signal shifts the locking point of the cavity to the side of the resonance, setting the subcarrier detuning δ_{sc}. We choose to introduce an offset that corresponds to a negative frequency ("red") detuning. Consequently the carrier is positively ("blue") detuned at $\delta_c = \Delta + \delta_{sc}$. An electronic locking servo can be used to process the error signal and feed back to coils, actuating on magnets mounted on the large cavity mirror, and to the laser frequency.

5.4.3 Subcarrier Servo

The high FSR of our cavity (2.14 GHz) meant that available AOMs, with much lower operating frequency ranges (65 to 95 MHz), were not suitable to lock the carrier and subcarrier on adjacent resonances. However, this same operating range prevents a single AOM from locking the two beams on the same resonance, due to the small cavity linewidth. Thus, we set the subcarrier on the same resonance fringe as the carrier using two AOMs, each one shifting the laser frequency by about 80MHz in opposite directions. One is driven by an 80 MHz crystal oscillator, while the other is driven by a servo-locked Voltage controlled oscillator (VCO) running slightly offset from 80 MHz (see figure 35). To control the offset frequency the 80 MHz signal from the crystal oscillator is mixed with the VCO output, producing a signal at the frequency difference. This difference signal is then mixed with the drive from a function generator, creating the error signal for the servo. The servo drives the frequency modulation input of the VCO, closing the loop and locking the subcarrier beam to a fixed frequency offset from the carrier beam.

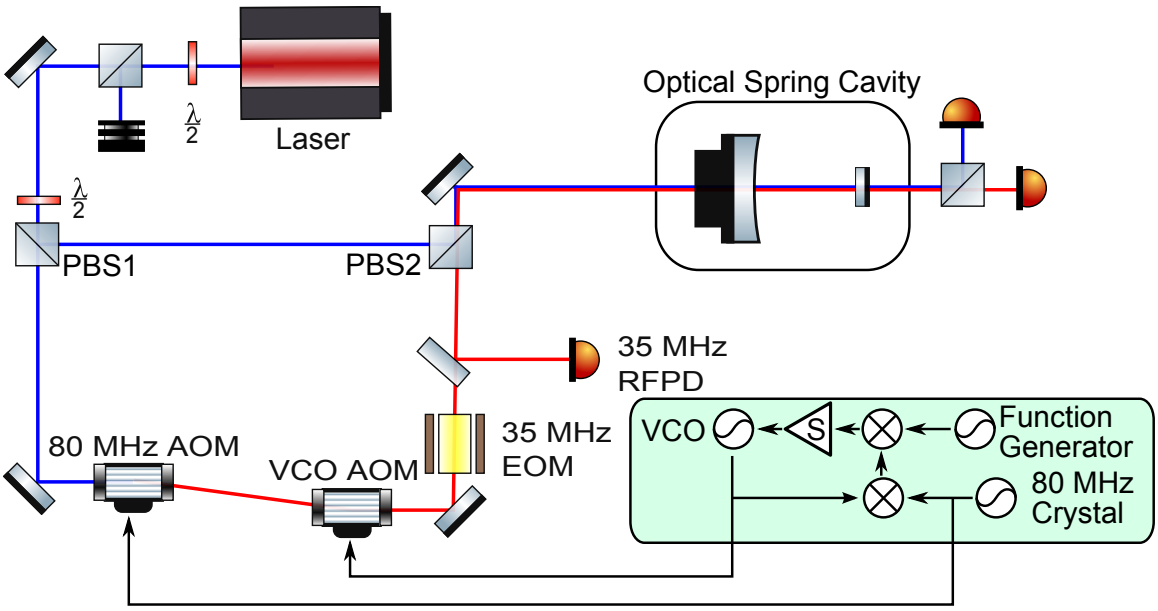

Figure 35 : A schematic layout of the optical trap experiment. The light from the laser is split into the carrier and subcarrier paths at PBS1, with a ratio determined by the $\lambda/2$ plate. The subcarrier path is frequency shifted by two AOMs under the control of the subcarrier servo (described in detail in Section 5.4.3), then recombined with the carrier at PBS2. The co-aligned mode-matched beams enter the cavity, then are individually monitored at the output. We can use the 35 MHz EOM and RFPD in a PDH scheme to read out the cavity length or lock the cavity.

This setup significantly suppresses the frequency noise from the VCO. The remaining subcarrier frequency noise (relative to the carrier) is dominated by fluctuations in the path length difference between carrier and sub-carrier, see figure 35.

5.5 Results

Using the setup described in the previous section, we locked the cavity using a PDH error signal from the sub-carrier, feeding back to the laser frequency actuator and, at low frequencies, the heavy input coupler position. In this configuration we fine-tuned the optical spring parameters (carrier and sub-carrier offset and power) and measured the PDH control loop open loop transfer function. Dividing out the known PDH loop sensing and actuation function gives us the closed loop transfer functions of the optical springs (figure 36). While we demonstrated stable and unstable dual-carrier optical springs, these measurements revealed a significantly smaller phase margin of the optical spring than expected based on equation 5.4, suggesting the presence of a

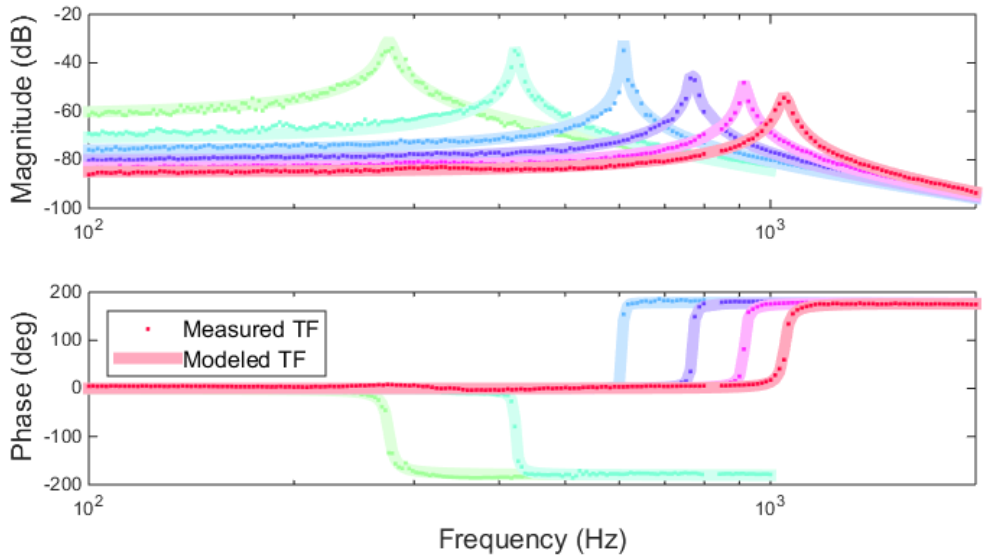

Figure 36 : Data and modeled transfer function for a series of stable and unstable springs. The modeled transfer functions include the full coating and spot size correction, computed with the measured average absorption. Stable springs show a phase drop of 180 degrees at resonance, while unstable springs show a rise of 180 degrees.

non-radiation-pressure feed-back path.

At a few ppm, the absorption A of the mirrors has a very small effect on the cavity finesse and no significant impact on the total transmitted power. However, this small amount of absorption still causes local heating of the optic, driving fluctuations in the surface position of the optic, and thus the cavity length, via the photo-thermal effect. If this is the dominant effect, we should be able to include the photo-thermal effect in our model and fit the model to the data, using the absorption as the free parameter. Given a set of optical spring measurements done under similar conditions, we would then expect to find a consistent absorption coefficient across measurements.

5.5.1 Analysis

For each measured optical spring transfer function we record the carrier and subcarrier transmitted powers, P_{tc} and P_{ts}, the optical spring resonance frequency f_{res}, and the difference between the carrier and subcarrier detunings $df_c - df_s$, which is set by the function generator frequency.

We can then fit the data d using a model m, which includes the photo-thermal

effect. In particular we fit the ratio d/m using a least-squares fit to minimize E, the error.

$$E = \Sigma \left| \frac{d}{m} - 1 \right|^2 \tag{5.8}$$

We fit for a small magnitude offset, the subcarrier detuning df_s, and the absorption A. We assess the fitting errors by modeling the noise in each frequency bin of the transfer function measurement, and propagating this noise through the fit. Four of the optical spring transfer functions had a measurement noise of a little less than 1 dB, while the optical springs at 276 Hz and 422 Hz had a significantly higher noise of about 3 dB. We think this noise is dominated by intra-cavity power fluctuations, most likely due to angular fluctuations.

The remaining parameters (cavity transmitted powers and carrier-sub-carrier frequency spacing) we treat as systematic errors. We propagated their measurment errors through the fit. We used a 2% measurement error for the power measurements and a 1 kHz error for the frequency separation.

After determining the absorption A for each optical spring transfer function measurement, we can take a statistical-error-weighted average to arrive at the most probable absorption coefficient for the mirror. For the full photo-thermal model we measure a consistent absorption of 2.60 ± 0.08 ppm (± 0.06 ppm statistical, ± 0.05 ppm systematic) (see figure 37). The naive $1/f$ model yields an absorption of 3.27 ± 0.10 ppm (± 0.08 ppm statistical, ± 0.06 ppm systematic). The detailed model with coating and spot size corrections is slightly preferred by the data over the naive $1/f$ model, i.e. the result is more consistent with the same absorption at all frequencies. However the errors in our mesurement are too large to make this statement with any sigificant certainty.

Since this measurement is based on the missing optical spring phase on resonance, we can also express the result as extra phase. Near the resonance the optical spring constant is close to real, while the photo-thermal effect is almost purely imaginary. Thus we approximately find for the extra phase ϕ

$$\phi = 2m\Omega^2 \frac{c}{2} \frac{\bar{\alpha}}{\Omega \rho C \mathrm{w}^2 \pi} A I_{\mathrm{corr}} \approx 0.4^\circ \frac{A I_{\mathrm{corr}}}{1 \text{ ppm}} \frac{f}{1 \text{ kHz}} \tag{5.9}$$

Here the leading factor of two accounts for the two mirrors, I_{corr} is the real part of the total correction factor plotted in figure 33, and we used the material parameters

for fused silica (see table 5). Figure 38 shows the measured extra phase on resonance, together with the prediction from the photo-thermal feed-back with the best-fit absorption. The figure also shows the expected phase due to the dual-carrier optical spring, as well as the total phase of the complete model. Finally it is worth mentioning that this is a remarkably precise way to measure the phase of the open loop transfer function - the error bars in figure 38 are as small as 0.04°.

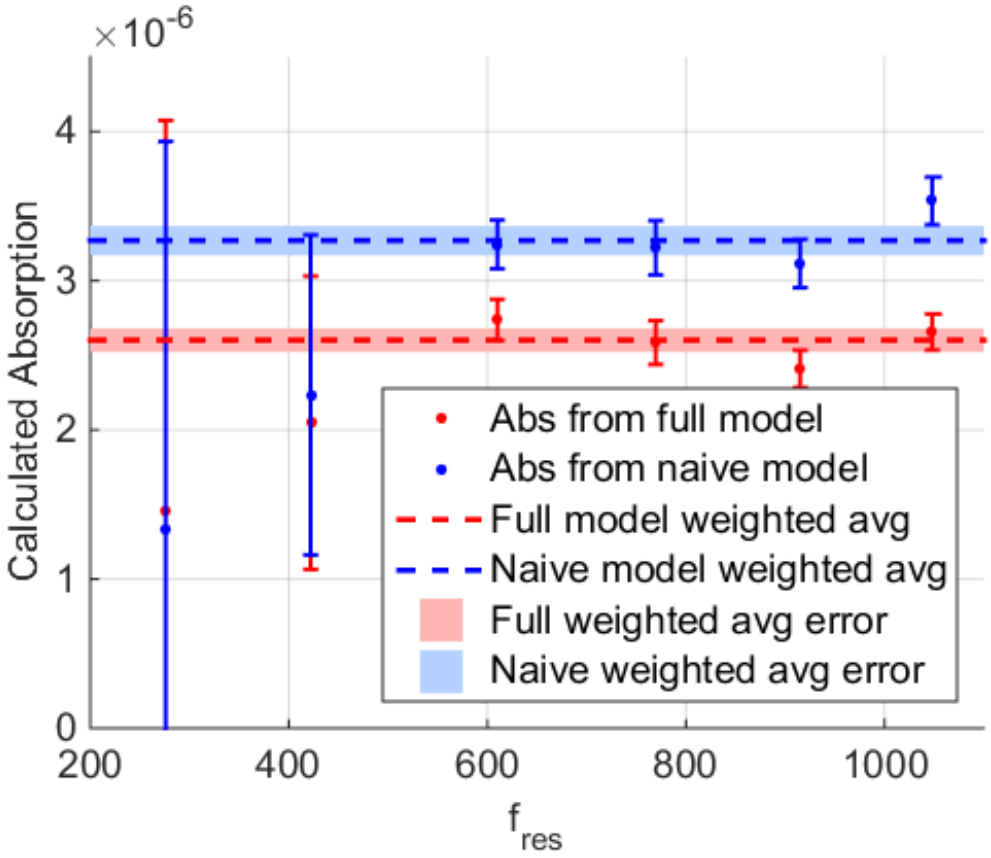

Figure 37 : Absorption fit for naive and full models. The full model absorption is consistent with a constant absorption of 2.60 ± 0.08 ppm. The naive $1/f$ model predicts 3.27 ± 0.10 ppm. The transfer function data for the lowest two resonant frequencies was significantly noisier. Also, at lower frequencies the photo-thermal effect has a smaller effect on the total optical spring. Both effects result in the larger error bars at low frequencies.

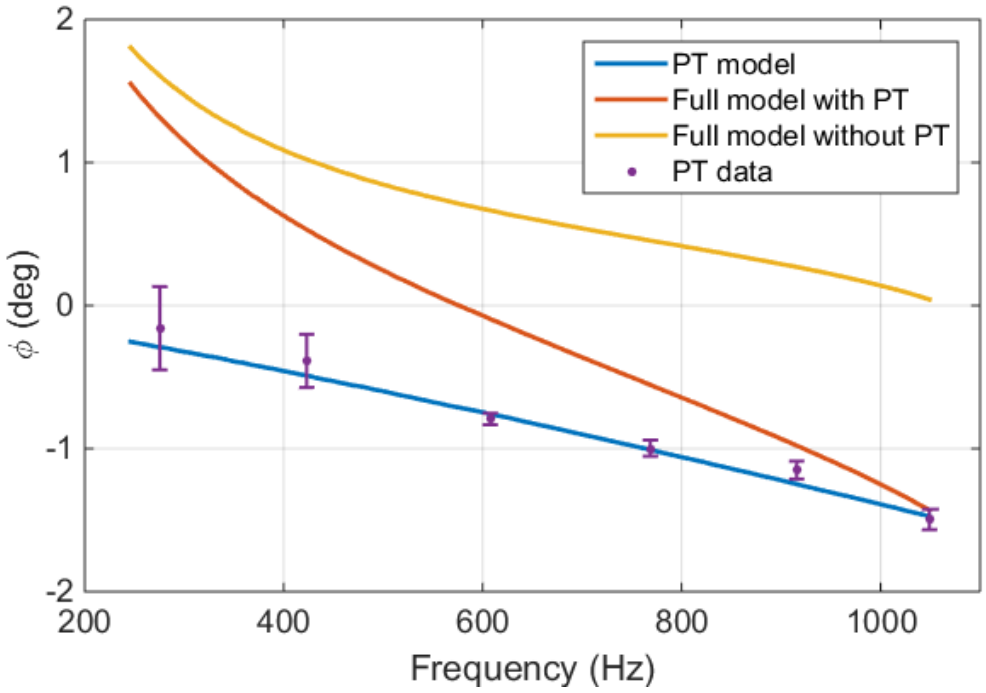

Figure 38 : Feedback phase in the system due to the optical spring and photo-thermal effect. The measured extra phase is consistent with 2.60 ppm of absorption. The error bars are as small as $\pm 0.04°$, a remarkable precision for an open loop transfer function phase measurement.

5.6 Stable single-carrier optical spring

In the experiment at hand the photo-thermal feed-back always pushed the optical spring resonance closer to instability. Perhaps the most interesting question is whether we can change the sign of this feed-back path and exploit it to stabilize an otherwise unstable optical spring. It was pointed out in [43] that this naturally occurs above about 100 kHz for a regular dielectric coating. At those frequencies the thermal diffusion length only affects the first few layers of the coating, which affect the overall coating reflected phase differently than the rest of the coating. However it is actually quite simple to get this sign inversion to occur at a much lower frequency. Increasing the thickness of the inital half-wavelength SiO_2 layer - but keeping it an odd multiple of half the wavelength - will boost the effect from the first layer, thus lowering the frequency at which this sign inversion occurs. Indeed this effect can be strong enough that the damping effect from the sub-carrier is not needed to generate a stable optical spring. To illustrate this, figure 39 shows a set of six optical springs with parameters

identical to the ones shown in figure 36, except that we set the sub-carrier power to zero (i.e. they are single-carrier optical springs), and we increased the first SiO_2 coating layer from 0.5 wavelength to 20.5 wavelength.

Such a modified coating would thus allow detuned self-locking of an optical cavity, using just one laser frequency. It does rely on a small amount (order 1 ppm) of optical absorption in the coating, but this level of absorption is often unavoidable anyway, and does not prevent high-finesse cavities.

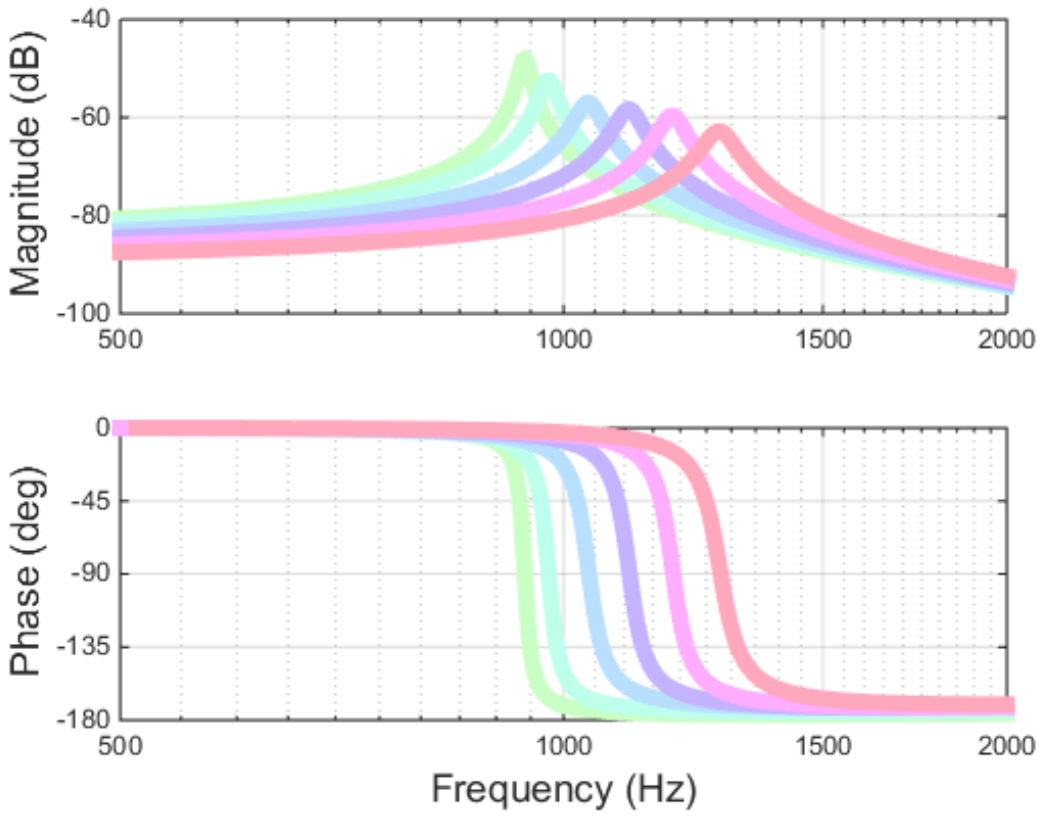

Figure 39 : Stable single-carrier optical springs (no sub-carrier) with modified coating - the first coating layer is 20.5 wavelength thick. See text for details. The six traces otherwise have the same parameters as the best-fit optical springs in figure 36.

5.7 Conclusions

We observed photo-thermal feedback in an experimental optical spring setup for a 0.4 gram mirror. We made measurements for a range of optical spring resonant

frequencies, and used a least squares fit to calculate the absorption. The data is consistent with the predictions of the complete model presented in Section 5.3, but only sligthly prefers it over a simple model that ignores any heat diffusion in the coating and transverse to the optical axis. We also show that a small modification of the first layer of the high-reflectivity coating would be enough to reverse the sign of the photo-thermal feed-back, to the extent that a single-carrier, dynamically and statically stable optical spring becomes feasable.

Repeating the presented measurement with a folding mirror in a cavity should also allow us to confirm the predicted enhancement of thermal noise for folding mirrors [46] . This noise will affect any gravitational-wave interferometer design making use of folding mirrors in the arm cavities [31].

Parameters Ta_2O_5:SiO_2	Symbol	SiO_2	Ta_2O_5	Unit
Refractive Index (@1064 nm)	n	1.45	2.06	-
Specific Heat	C	746	306	J/kg/K
Density	ρ	2200	6850	kg/m^3
Thermal Conductivity	κ	1.38	33	W/m/K
Thermal expansion coef.	α	0.51	3.6	ppm/K
Thermo-Optic coef. (1μm)	$\beta = \frac{dn}{dT}$	8	14	ppm/K
Poisson ratio	σ	0.17	0.23	-
Youngs Modulus	E	72.80	140	GPa

Table 5 : Parameters for fused silica (SiO_2) and tantulum-pentoxide (Ta_2O_5). The values are taken from [40] and [47].

Chapter 6

Angular

6.1 Introduction

The Laser Interferometer Gravitational-wave Observatory (LIGO) is part of a worldwide effort to detect gravitational waves and use them to study the universe [1]. Construction of LIGO's advanced detectors has finished and the first science runs will begin soon. The goal of Advanced LIGO (aLIGO) is the first direct detection of gravitational-waves from astrophysical sources such as coalescing compact binaries and core-collapse supernovae. These detections will open a new spectrum for observing the universe and establish the field of gravitational-wave astronomy. These initial observations will also show the potential science gain of further increasing the state-of-the-art sensitivity of gravitational wave detectors [2, 3, 4]. Such detectors operate near the Standard Quantum Limit, meaning that the contributions from quantum radiation pressure and shot noise are about equal in the observation band [5, 6].

To design a successor to aLIGO, techniques to operate gravitational-wave interferometers below the Standard Quantum Limit need to be developed [7, 8]. Dual carrier control systems and angular control using stable optical springs are promising methods for evading quantum-mechanical limitations on detector sensitivity [9, 10, 11, 12, 13, 14]. In 2007 Corbitt et al. at the LIGO Laboratory at the Massachusetts Institute of Technology demonstrated a one-dimensional optical trap of a one gram mirror using a novel two-carrier scheme [15]. Their work clearly demonstrated the potential of this technique. Extended to angular degrees of freedom, it has the prospect of opening a completely new approach to the angular control problem in future generation

gravitational-wave detectors [16]. Sidles and Sigg have shown that, for a Fabry-Perot cavity with a single resonating laser field, the radiation pressure force will couple the two end mirrors, always creating one soft (unstable) and one hard (stable) mode [17]. This sets a lower limit on the required angular control bandwidth, which inevitably results in higher noise contamination by angular control noise and limits the angular control performance in the first and second generation gravitational-wave interferometers [9, 18, 19, 20]. Angular optical trapping can bypass the Sidles-Sigg instability. Its fundamental noise limit is quantum radiation pressure noise, making it a promising candidate for low-noise angular control.

6.2 Optical Springs

In this paper, we will discuss the control of a mirror using two pairs of optical springs, creating two stable degrees of freedom in a single mirror. One pair will be a executed in a straight cavity and one will be in a folded cavity. In a previous paper, we have derived the behavior of a single optical spring in a straight cavity:

$$K_{OS} \approx P_0 t_1^2 \frac{8k}{c(1-r_1r_2)^3} \frac{\frac{\delta}{\gamma}}{(1+\frac{\delta^2}{\gamma^2})} \frac{1}{1+\frac{\delta^2}{\gamma^2}-\frac{\Omega^2}{\gamma^2}+i2\frac{\Omega}{\gamma}} \tag{6.1}$$

In the appendix, we demonstrate the optical spring behavior of a folded cavity optical spring.

$$K_{OS} \approx P_0 t_1^2 \frac{32k}{c(1-(r_1r_2)^2)^3} \frac{\frac{\delta}{\gamma}}{(1+\frac{\delta^2}{\gamma^2})} \frac{1}{1+\frac{\delta^2}{\gamma^2}-\frac{\Omega^2}{\gamma^2}+i2\frac{\Omega}{\gamma}} \tag{6.2}$$

We note that the only differences between the two equations are a factor of four in the numerator and the change of r_1r_2 to $(r_1r_2)^2$ in the denominator.

Because these beams are exerting force on a single mirror, we expect some crosstalk between the straight optical spring pair and the folded optical spring pair. We have attempted to minimize this though our choice of spot locations on the mirror (see appendix A).

6.3 Setup

Our experiment (see fig. 40) uses a 2 Watt 1064 nm Nd:YAG laser. The laser beam is split into a carrier beam and a subcarrier beam, then the subcarrier is frequency shifted by a tunable amount, described in more detail in section IV of our previous paper [48]. The two beams are mode matched and spatially recombined (in opposite linear polarizations) in a Mach-Zehnder-style setup. The recombined beam is then split using an unpolarized beamsplitter into main and side beams. The main beam enters the straight cavity, while the side beam enters the folded cavity. Both polarizations of both beams are monitored in transmission and reflection.

Parameter	Straight	Folded
λ_0	1064 nm	1064 nm
Mirror1,3,4 RoC	7.5 cm	7.5 cm
Mirror2 RoC	5.0 cm	5.0 cm
L_0	10.0 cm	20.0 cm
M1,3,4 Spot size	268 μm	268 μm
M2 Spot size	155 μm	155 μm
FSR	1.50 GHz	0.75 GHz
Finesse	7500	3750
Cavity Pole	98.6 KHz	98.6 KHz
Folded cavity angle, θ	11 deg	

δf_C	213-290 KHz
δf_{SC}	27-36 KHz
P_C input	225-239 mW
P_{SC} input	65-78 mW

Table 6 : Optical setup for the angular trap. The straight and folded cavities have different parameters due to the difference in total length and number of mirrors. RIGHT TABLE IS NONSENSE.

6.4 Appendix

To determine the behavior of a folded optical spring, we can compare it to the standard optical spring derivation [44].

We begin with a folded cavity with three mirrors, shown in fig. 41. We assume that M3 and M4 have the same amplitude reflectivity as M1, r_1, while we allow the end mirror to have a different reflectivity, r_2. The incoming field is $E = e^{\frac{i2\pi ct}{\lambda}}$. The average round-trip path length is $L = 2L_0$, where L_0 is the optical patch length

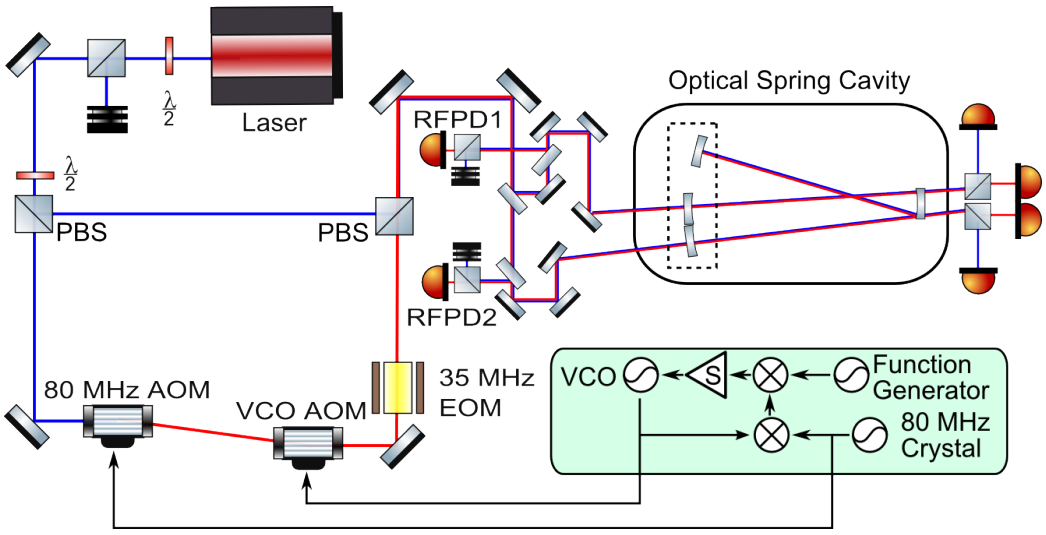

Figure 40 : Layout of the angular trap cavity experiment. The light from the laser is split into the carrier and subcarrier paths with a polarizing beam splitter (PBS), with a ratio determined by the $\lambda/2$ plate. The subcarrier path is frequency shifted by two AOMs under the control of the subcarrier servo then recombined with the carrier with another PBS. The co-aligned mode-matched beams are then split into main and side paths, which enter the trap cavity. The main beam has a straight optical path and is read out in transmission by broadband photodiodes and in reflection by RFPD1. The side beam has a folded optical path and is read out in transmission by broadband photodiodes and in reflection by RFPD2. We can use the 35 MHz modulation from the EOM with the two RFPDs in a PDH scheme to read out the cavity lengths or lock the cavities.

between mirrors M3 and M4. We consider microscopic changes in cavity length d_n, which are discreet samples of a harmonic oscillation $d(t) = x_0 e^{i\Omega t}$. The light travel time between M3 and M4 is $\tau = \frac{L_0}{c}$. It is important to note that the cavity length L_0 of the folded cavity is twice that of the straight cavity in our experiment.

We can use the same X and Y notation as the original derivation with one small change. $Y = e^{-i\Omega 2\tau}$ is the same, but now $X = (r_1 r_2)^2 e^{\frac{-i2\pi L}{\lambda}}$ because the optical path touches M3 and M4 once and M2 twice.

We consider a set of displacements d_n, discretely sampled from a continuously oscilating function. This is equivelent to driving the cavity length at angular frequency Ω.

$$d(t) = x_0 e^{i\Omega(t-(2n-1)\tau)} \tag{6.3}$$

$$d_1 = x_0 e^{i\Omega(t-\tau)} \tag{6.4}$$

$$d_n = Y^{2n-2} d_1 \tag{6.5}$$

Following [44], we get an equation for the electric field in the cavity, which we must change to reflect that we can only have real values for d_1.

$$E_{tot} = \frac{t_1 E}{1-X}\left[1 - \frac{4i\pi d_1}{\lambda}\frac{X}{1-Y^2X}\right]$$

$$E_{tot} = \frac{t_1 E}{1-X}\left[1 - \frac{4i\pi}{\lambda}\left(\frac{d_1}{1-Y^2X} + \frac{\overline{d}_1}{1-\overline{Y}^2X}\right)\right] \tag{6.6}$$

Then we get the cavity power:

$$P = E_{tot}\cdot\overline{E}_{tot} = P_0 t^2\left[\frac{i2\pi Y}{\lambda(1-X)(1-\overline{X})}\left(\frac{X}{1-Y^2X} - \frac{\overline{X}}{1-Y^2\overline{X}}\right)\delta L + cc\right] \tag{6.7}$$

We add an extra $Y^{1/2}$ term to get to the other side of the cavity. It is important to note that the change in cavity length δL used here is strictly that: the cavity length. If we want to transpose that into longitudinal change, we need to multiply by a geometric factor (see fig. 41):

$$\delta L = \frac{2\delta z}{\mathrm{Cos}(\theta)} \tag{6.8}$$

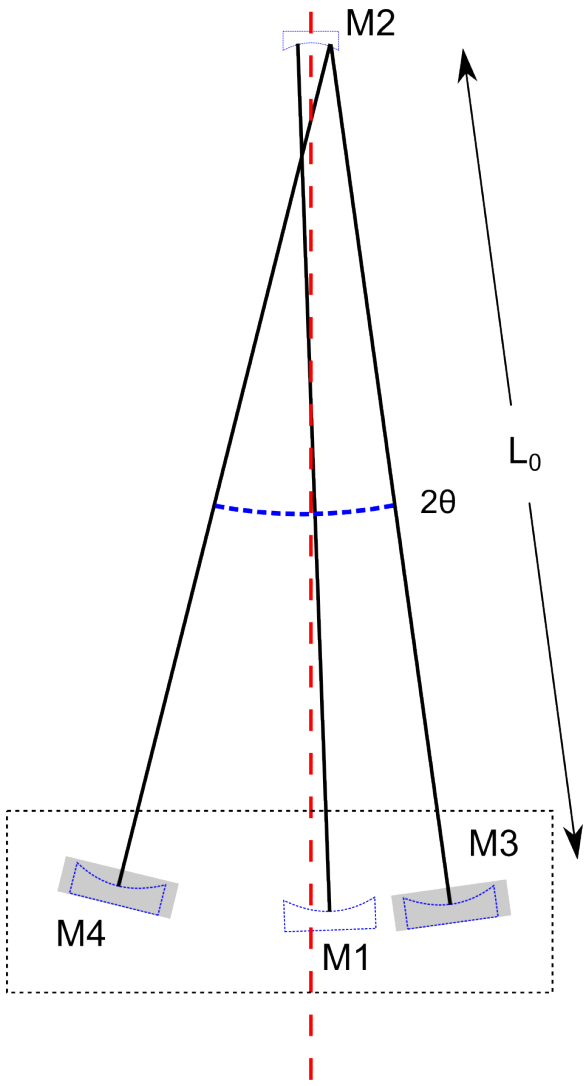

Figure 41 : Layout of the angular trap cavity. Light enters through mirrors M1 and M3. The angle θ of the folded cavity is measured from the normal of M1.

There is similarly a geometric correction when calculating the radiation pressure force F_{rad}

$$F_{rad} = \frac{2r_2^2}{c}P(2\mathrm{Cos}(\theta)) = K_z\delta z \tag{6.9}$$

$$= \frac{2r_2^2}{c}(2\mathrm{Cos}(\theta))P_0t^2\left[\frac{i2\pi Y^{3/2}}{\lambda(1-X)(1-\overline{X})}\left(\frac{X}{1-Y^2X}-\frac{\overline{X}}{1-Y^2\overline{X}}\right)\frac{2\delta z}{\mathrm{Cos}(\theta)}\right] \tag{6.10}$$

thus

$$K_z = \frac{4r_2^2}{c}P_0t^2\frac{i4\pi Y^{3/2}}{\lambda(1-X)(1-\overline{X})}\left(\frac{X}{1-Y^2X}-\frac{\overline{X}}{1-Y^2\overline{X}}\right) \tag{6.11}$$

With detuning:

$$X \to X = (r_1r_2)^2e^{-i2\delta\tau} \tag{6.12}$$

Here $\delta = \omega_0 - \omega_{res}$, the angular frequency detuning from the cavity resonance, $\omega_{res} = 2\pi nc/L$, and ω_0 is the frequency of the laser.

$$K_{OS} = -P_0t^2r_2^2\frac{16i\pi e^{-\frac{3}{2}i\Omega\tau}}{\lambda c(1-(r_1r_2)^2e^{i2\delta\tau})(1-(r_1r_2)^2e^{-i2\delta\tau})}\times \left(\frac{(r_1r_2)^2e^{-i\delta\tau}}{1-(r_1r_2)^2e^{-2i\Omega\tau}e^{-i2\delta\tau}}-\frac{(r_1r_2)^2e^{i2\delta\tau}}{1-(r_1r_2)^2e^{-2i\Omega\tau}e^{i2\delta\tau}}\right) \tag{6.13}$$

Considering the finesse for the folded cavity to be $F = \pi\frac{FSR}{\gamma} \approx \frac{\pi}{1-(r_1r_2)^2}$

keep in mind that we have half the FSR of a non-folded cavity and half the finesse, so γ is the same here as it is for the longitudinal trap.

$$K_{OS} \approx P_0t_1^2\frac{32k}{c(1-(r_1r_2)^2)^3}\frac{\frac{\delta}{\gamma}}{(1+\frac{\delta^2}{\gamma^2})}\frac{1}{1+\frac{\delta^2}{\gamma^2}-\frac{\Omega^2}{\gamma^2}+i2\frac{\Omega}{\gamma}} \tag{6.14}$$

This is important because it means that a folded cavity angular spring will behave differently. Namely, the folded cavity spring constant is four times larger in magnitude than a similar straight cavity, and there is a change of r_1r_2 to $(r_1r_2)^2$.

6.4.1 angular issues

worried about the change in beam shape not an issue (but did lock on TEM01)

shape of power distribution on end mirror.

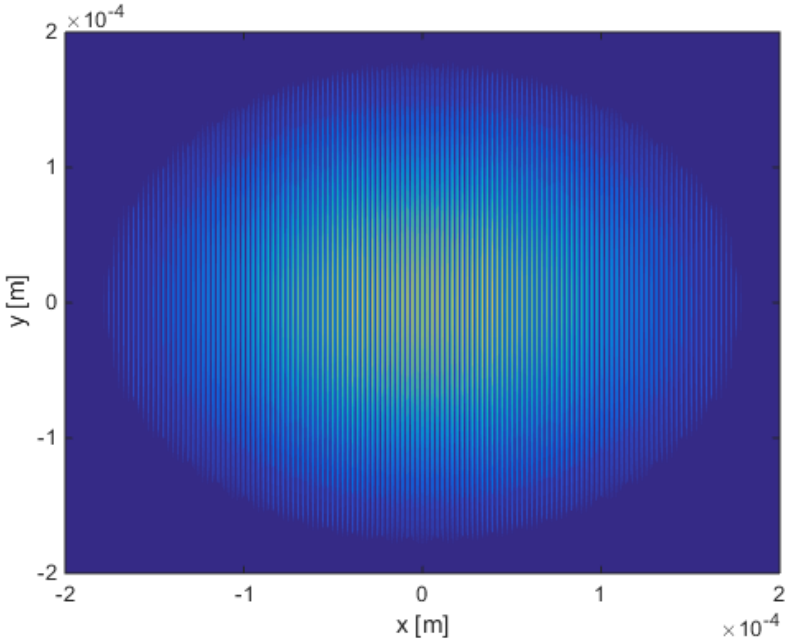

Figure 42 : Simulated folded cavity interference pattern on the surface of M2. This corresponds to the power deposited into the mirror and thus the amplitude of the photothermal effect. Using this and the diffusion length as a function of frequency, we showed that there would be no significant amplification of the photothermal effect due to this distribution of absorbed power.

Chapter 7

Application

7.1 What we're dealing with

Angular control in LIGO is an important contribution to the noise budget at the frequencies of highest sensitivity. (T0900511)

There are four different angular modes for the two Fabry-Perot arms in the LIGO interferometer, shown in figure 43. The two Hard modes are stable as the power increases, which means that the radiation pressure will push the mirrors back to an equilibrium position. The two Soft modes are unstable as the power increases, pushing the mirrors away from equilibrium.

Angular noise can couple in to differential arm length (DARM) though the interaction between beam spot motion (BSM) and angular motion (θ) on mirrors. This happens in two ways: both a static offset in the BSM with mirror angular noise and a static angular offset with BSM noise can create DARM noise.

$$\hat{\Delta L}(f) = \hat{d}_{spot}(f) * \hat{\theta}_{Mirror}(f) \approx \hat{d}_{spot}(f) * \theta^{RMS}_{Mirror}(f) + d^{RMS}_{spot}(f) * \hat{\theta}_{Mirror}(f) \quad (7.1)$$

Barsotti and Evans showed that, in Science Mode, angular noise from Common Soft and Differential Soft (the two modes of the arms that are unstable at high power) contribute the most to DARM noise. They also showed that in the final design of aLIGO, the soft mode is unstable with frequencies of -.17 and -.21 Hz for pitch and yaw, respectively. The optical trap will need to provide enough phase at that frequency to stabilize the mode.

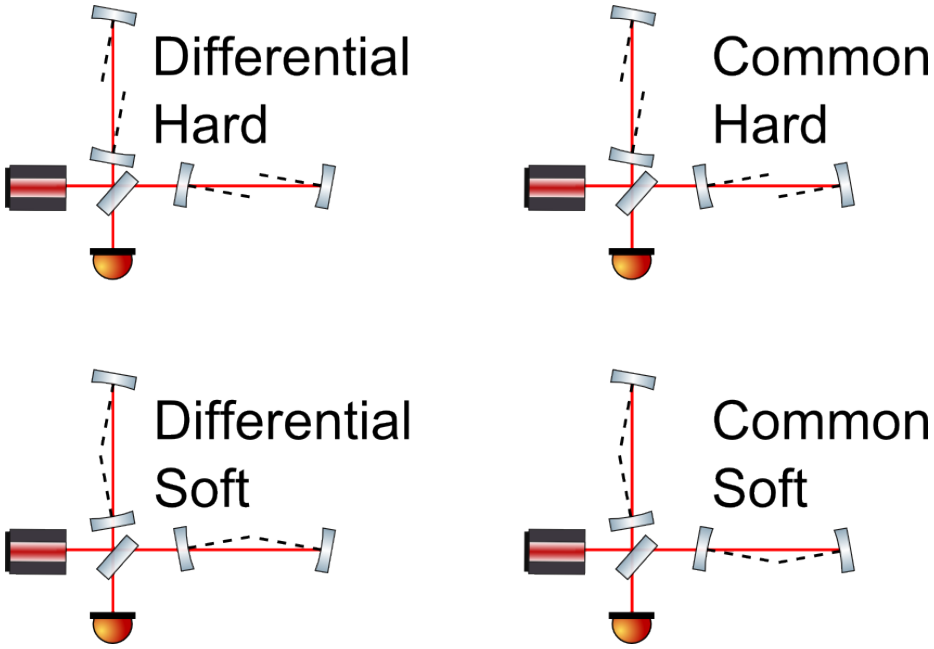

Figure 43 : The four Sidles-sigg modes of the Fabry-Perot cavities in LIGO. The two hard modes are stable and the two soft modes are unstable.

Using angular trapping methods, we can reduce part of this noise contribution by damping the angular motion $\hat{\theta}_{Mirror}(f)$.

7.2 Applying angular control

For our discussion, we will disregard the distinction between common and differential modes of the interferometer.

I have considered two possible options that could (with some effort) be implemented in a LIGO-style interferometer.

7.2.1 Local damping

Damping relative to something very heavy in the end station

BSC4 layout: D0901154

Pros:

- Can keep the same ETM/ITM suspensions
- Modular: easy to modify and/or disable

- Easier to build, align and lock
- Affects Soft and Hard modes equally.

Cons:

- Different parameters for ETM and ITM
- Folded Cavities
- worry about ISI weight limit

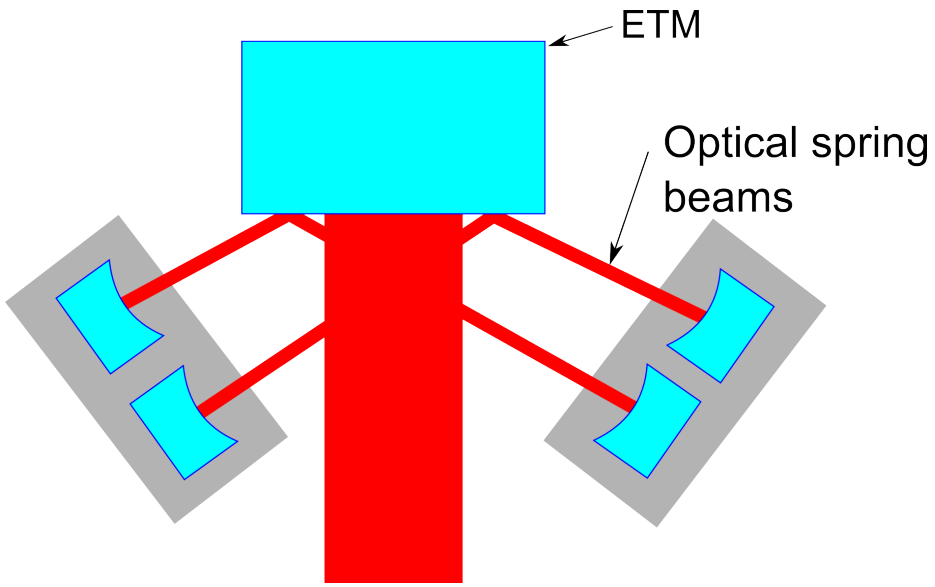

Figure 44 : Diagram of a local angular control scheme. This relies on the small mirrors being mounted in something heavier than the test mass.

In this design, we use radiation pressure to couple e.g. the ETM (about 40 kg) to two much larger masses (about 400 kg each) made out of stainless steel. In this fashion, we can damp the angular motion of the test mass relative to the hopefully much more stable masses on the side.

With the control beams at $\tilde{4}5$ degrees to the optical axis, we expect that the coating will be significantly lower reflectivity. Er-glass lasers at 1540 nm

Parameter	**Metric**
Cavity length, L	2 m
ETM power transmission, $T2$	5 ppm
ETM $r2$	0.9999975
ETM Diameter D	34 cm
ETM Thickness t	20 cm
Side diameter D_s	48 cm
Side thickness t_s	30 cm
Side ROC	1.5 m
Cavity FSR	75 MHz

Table 7 : Characteristics of proposed local angular design

Parameter	**Metric**
Carrier Power P_c	10 W
Subcarrier Power P_s	2 W
Carrier Detuning df_c	9000 Hz
Subcarrier Detuning df_s	-2500 Hz
OS Angle θ	45 deg

Table 8 : Characteristics of proposed local angular optical spring

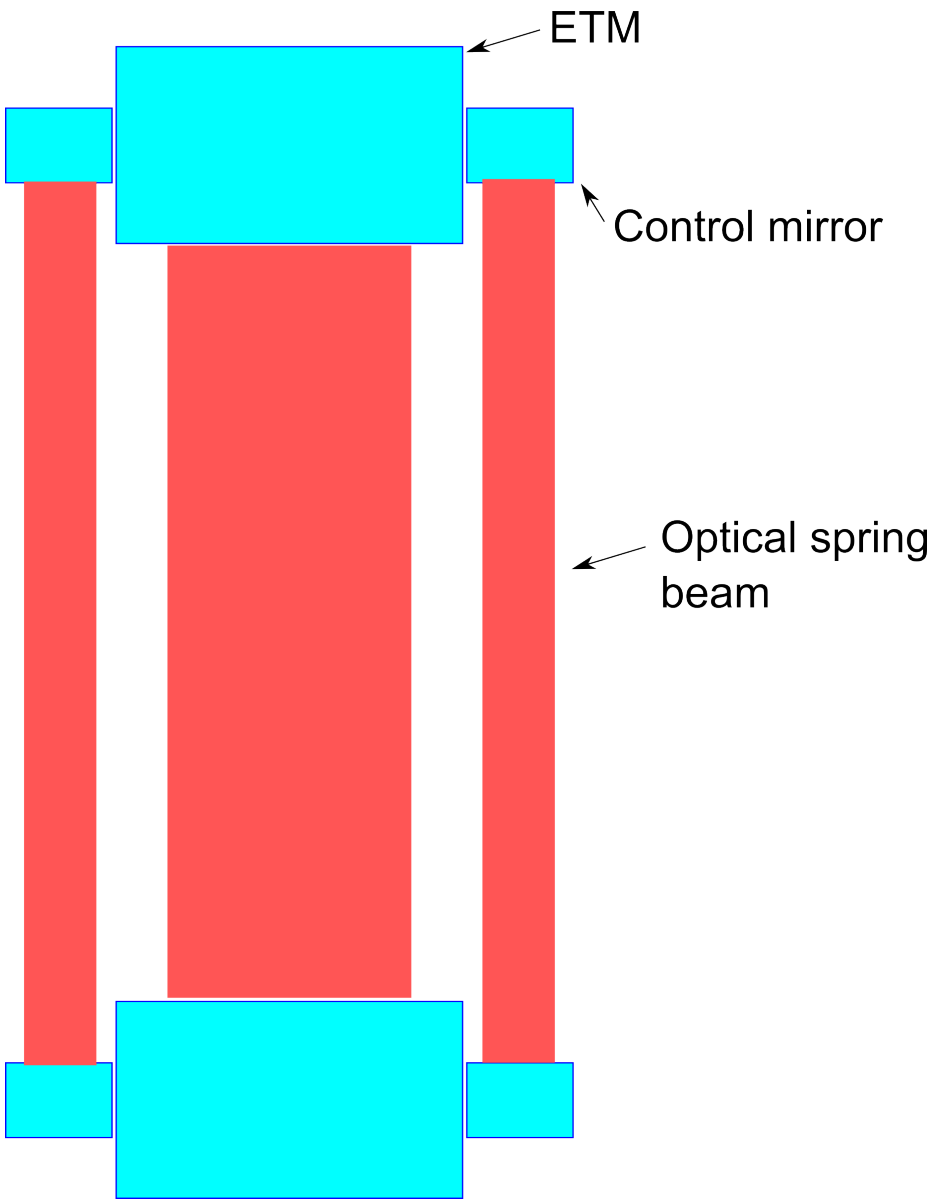

Figure 45 : Diagram of a 4km angular control scheme. This relies on control mirrors attached to the side of the test mass.

7.2.2 4 km damping

Damping ETM relative to ITM. This will have significant changes because the masses of the ETM and ITM are currently the same. The angular trap we have damps the motion of one mirror by pushing on the other. In a system with equal masses, this just couples the mirrors, it doesn't damp.

Pros:

- Straight cavities
- Lower vacuum chamber volume
- Damp only Soft mode

Cons:

- Does not see Hard mode motion of cavity
- Modify test masses and probably suspensions
- Hard/risky to adjust

Parameter	**Metric**
Cavity length, L	3994.5 m
ITM power transmission, $T1$	1.4%
ETM power transmission, $T2$	5 ppm
ITM $r1$	0.99298
ETM $r2$	0.9999975
Cavity FSR	37.52 KHz

Table 9 : Characteristics of proposed long angular design

7.3 noise benefits

The cool thing about this method is that it can work independently and in tandem with existing control systems.

7.4 path to angular damping with optical springs in aLIGO

I think we might want to get rid of this section.

Chapter 8

Conclusion

I hope to have found something by this point in the thesis.

Appendix A

Beam Separation

A.1 Definitions

- P_m Input power of the main beam
- P_s Input power of the side beam
- f_m Main cavity finesse
- f_s Side cavity finesse
- R_c Radius of curvature of payload mirror (5 cm)
- θ_m Main beam angle from optical axis. Origin is at center of curvature.
- θ_s Side beam angle from optical axis. Origin is at center of curvature.
- c Speed of light
- R Payload mirror radius
- h Payload mirror thickness
- m Payload mirror mass
- $I = \frac{m}{12}(3R^2 + h^2)$ Payload mirror moment of inertia
- $G = \frac{P_m f_m}{P_s f_s}$ Handy constant
- $d = \theta_m R_c - \theta_s R_c$ Beam spot seperation

A.2 Balancing torques

We want the mirror to be stationary, so the net torque on the mirror should be zero.

Force on payload mirror due to radiation pressure of the two beams:

$$F_m = \frac{2P_m f_m}{c} \qquad F_s = \frac{2P_s f_s}{c}$$

$$\tau = F_m \theta_m R_c + F_s \theta_s R_c = 0$$

substituting in d,

$$\theta_m = \frac{d}{R_c(1+G)}$$

A.3 Eliminating beam coupling

We propose that there is a spot somewhere on the surface of the payload mirror where the sum of torque and force due to one beam makes the net force zero. We place one beam spot at r_1. We'd like to put the other beam in the null spot r_2 so that there is no force coupling between the two.

$$Fs = \frac{2P_s f_s}{c} = m\omega^2 x \qquad x = \frac{F_s}{m\omega^2}$$
$$\tau_s = F_s r_1 = I\omega^2 \phi \qquad \phi = \frac{F_s r_1}{I\omega^2}$$

Let's find a point these effects cancel:

$$r_2\phi - x = 0 \qquad r_2 = \frac{x}{\phi} = \frac{I}{mr_1}$$

It should be noted that the previously used d can also be expressed as $d = r_2 - r_1$.

$$r_2 = \theta_2 R_c = \theta_m R_c$$

$$r_2 = \frac{d}{1+G}$$

$$\frac{I}{m} = \frac{(r_2 - r_1)r_1}{1+G} = \frac{\left(\frac{I}{mr_1} + r_1\right) r_1}{1+G}$$

$$r_1 = \sqrt{\frac{I}{mG}} \qquad r_2 = \sqrt{\frac{IG}{m}}$$

These radii are the ideal horizontal distances from the payload mirror optical axis to the beam spots.

Bibliography

[1] B. P. Abbott, R. Abbott, R. Adhikari, P. Ajith, B. Allen, G. Allen, R. S. Amin, S. B. Anderson, W. G. Anderson, M. A. Arain, and et al. LIGO: the Laser Interferometer Gravitational-Wave Observatory. *Rep. Prog. Phys.*, 72(7):076901, 2009.

[2] J. R. Smith and LIGO Scientific Collaboration. The path to the enhanced and advanced LIGO gravitational-wave detectors. *Classical Quantum Gravity*, 26(11):114013, 2009.

[3] G. M. Harry and LIGO Scientific Collaboration. Advanced LIGO: the next generation of gravitational wave detectors. *Classical and Quantum Gravity*, 27(8):084006, April 2010.

[4] Giovanni Losurdo. Ground-based gravitational wave interferometric detectors of the first and second generation: an overview. *Classical Quantum Gravity*, 29(12):124005, 2012.

[5] C. M. Caves. Quantum-Mechanical Radiation-Pressure Fluctuations in an Interferometer. *Phys. Rev. Lett.*, 45:75–79, 1980.

[6] W.-T. Ni. Quantum measurements and the standard quantum limit. *Phys. Rev. A*, 33:2225–2229, 1986.

[7] S. L. Danilishin and F. Y. Khalili. Quantum Measurement Theory in Gravitational-Wave Detectors. *Living Rev. Relativity*, 15:5, 2012.

[8] Y. Chen. Macroscopic quantum mechanics: theory and experimental concepts of optomechanics. *J. Phys. B*, 46(10):104001, 2013.

[9] LIGO Document. Report No LIGO-T1000416-v3, 2010.

[10] V. B. Braginsky, S. E. Strigin, and S. P. Vyatchanin. Analysis of parametric oscillatory instability in power recycled LIGO interferometer. *Phys. Lett. A*, 305:111–124, 2002.

[11] O. Arcizet, T. Briant, A. Heidmann, and M. Pinard. Beating quantum limits in an optomechanical sensor by cavity detuning. *Phys. Rev. A*, 73(3):033819, 2006.

[12] T. Corbitt, D. Ottaway, E. Innerhofer, J. Pelc, and N. Mavalvala. Measurement of radiation-pressure-induced optomechanical dynamics in a suspended Fabry-Perot cavity. *Phys. Rev. A*, 74(2):021802, 2006.

[13] T. J. Kippenberg, H. Rokhsari, T. Carmon, A. Scherer, and K. J. Vahala. Analysis of Radiation-Pressure Induced Mechanical Oscillation of an Optical Microcavity. *Phys. Rev. Lett.*, 95(3):033901, 2005.

[14] B. S. Sheard, M. B. Gray, C. M. Mow-Lowry, D. E. McClelland, and S. E. Whitcomb. Observation and characterization of an optical spring. *Phys. Rev. A*, 69(5):051801, 2004.

[15] Thomas Corbitt, Yanbei Chen, Edith Innerhofer, Helge Müller-Ebhardt, David Ottaway, Henning Rehbein, Daniel Sigg, Stanley Whitcomb, Christopher Wipf, and Nergis Mavalvala. An all-optical trap for a gram-scale mirror. *Phys. Rev. Lett.*, 98:150802, 2007.

[16] M. Punturo and et al. The third generation of gravitational wave observatories and their science reach. *Classical Quantum Gravity*, 27(8):084007, 2010.

[17] J.A. Sidles and D. Sigg. Optical torques in suspended fabryperot interferometers. *Phys. Lett. A*, 354(3):167 – 172, 2006.

[18] V.B. Braginsky, S.E. Strigin, and S.P. Vyatchanin. Parametric oscillatory instability in FabryPerot interferometer. *Phys. Lett. A*, 287(56):331 – 338, 2001.

[19] Katherine L. Dooley, Lisa Barsotti, Rana X. Adhikari, Matthew Evans, Tobin T. Fricke, Peter Fritschel, Valera Frolov, Keita Kawabe, and Nicolás Smith-Lefebvre. Angular control of optical cavities in a radiation-pressure-dominated regime: the enhanced ligo case. *J. Opt. Soc. Am. A*, 30(12):2618–2626, 2013.

[20] Eiichi Hirose, Keita Kawabe, Daniel Sigg, Rana Adhikari, and Peter R. Saulson. Angular instability due to radiation pressure in the ligo gravitational-wave detector. *Appl. Opt.*, 49(18):3474–3484, 2010.

[21] C. Genes, D. Vitali, P. Tombesi, S. Gigan, and M. Aspelmeyer. Ground-state cooling of a micromechanical oscillator: Comparing cold damping and cavity-assisted cooling schemes. *Phys. Rev. A*, 77(3):033804, 2008.

[22] J. D. Teufel, T. Donner, D. Li, J. W. Harlow, M. S. Allman, K. Cicak, A. J. Sirois, J. D. Whittaker, K. W. Lehnert, and R. W. Simmonds. Sideband cooling of micromechanical motion to the quantum ground state. *Nature*, 475:359–363, 2011.

[23] A. D. O'Connell, M. Hofheinz, M. Ansmann, R. C. Bialczak, M. Lenander, E. Lucero, M. Neeley, D. Sank, H. Wang, M. Weides, J. Wenner, J. M. Martinis, and A. N. Cleland. Quantum ground state and single-phonon control of a mechanical resonator. *Nature*, 464:697–703, 2010.

[24] J. Chan, T. P. M. Alegre, A. H. Safavi-Naeini, J. T. Hill, A. Krause, S. Gröblacher, M. Aspelmeyer, and O. Painter. Laser cooling of a nanomechanical oscillator into its quantum ground state. *Nature*, 478:89–92, 2011.

[25] Thomas Corbitt, Christopher Wipf, Timothy Bodiya, David Ottaway, Daniel Sigg, Nicolas Smith, Stanley Whitcomb, and Nergis Mavalvala. Optical dilution and feedback cooling of a gram-scale oscillator to 6.9 mk. *Phys. Rev. Lett.*, 99:160801, 2007.

[26] N. Matsumoto, Y. Michimura, G. Hayase, Y. Aso, and K. Tsubono. Classical pendulum feels quantum back-action. *ArXiv Quantum Physics e-prints*, 2013.

[27] P. R. Saulson. Thermal noise in mechanical experiments. *Phys. Rev. D*, 42:2437–2445, 1990.

[28] A. L. Greensite. *Elements of modern control theory.* Spartan Books, New York, 1970.

[29] G. F. Franklin and A Powell, J. D. Emami-Naeini. *Elements of modern control theory.* Addison-Wesley, Reading, MA, 1994.

[30] V. B. Braginsky and S. P. Vyatchanin. Low quantum noise tranquilizer for Fabry-Perot interferometer. *Phys. Lett. A*, 293:228–234, 2002.

[31] S. W. Ballmer and D. J. Ottaway. New class of optical beams for large baseline interferometric gravitational wave detectors. *Phys. Rev. D*, 88(6):062004, 2013.

[32] A. E. Siegman. *Lasers*. University Science Books, Herndon, VA, 1986.

[33] E. D. Black. An introduction to Pound-Drever-Hall laser frequency stabilization. *Am. J. Phys.*, 69:79–87, 2001.

[34] N. Mavalvala. *Alignment Issues in Laser Interferometric Gravitational-Wave Detectors*. PhD thesis, Massachusetts Institute of Technology, 1997.

[35] Gregory M Harry and the LIGO Scientific Collaboration. Advanced ligo: the next generation of gravitational wave detectors. *Classical and Quantum Gravity*, 27(8):084006, 2010.

[36] J. Degallaix, T. Accadia, F. Acernese, M. Agathos, A. Allocca, P. Astone, G. Ballardin, F. Barone, M. Bejger, M. G. Beker, M. Bitossi, M. A. Bizouard, M. Blom, F. Bondu, L. Bonelli, R. Bonnand, V. Boschi, L. Bosi, B. Bouhou, C. Bradaschia, M. Branchesi, T. Briant, A. Brillet, V. Brisson, T. Bulik, H. J. Bulten, D. Buskulic, C. Buy, G. Cagnoli, E. Calloni, B. Canuel, F. Carbognani, F. Cavalier, R. Cavalieri, G. Cella, E. Cesarini, E. Chassande-Mottin, A. Chincarini, A. Chiummo, F. Cleva, E. Coccia, P.-F. Cohadon, C. N. Colacino, A. Colla, M. Colombini, A. Conte, J.-P. Coulon, E. Cuoco, S. D'Antonio, V. Dattilo, M. Davier, R. Day, R. De Rosa, G. Debreczeni, W. Del Pozzo, L. Di Fiore, A. Di Lieto, A. Di Virgilio, A. Dietz, M. Drago, G. Endroczi, V. Fafone, I. Ferrante, F. Ferrini, F. Fidecaro, I. Fiori, R. Flaminio, L. A. Forte, J.-D. Fournier, J. Franc, S. Franco, S. Frasca, F. Frasconi, M. Galimberti, L. Gammaitoni, F. Garufi, M. E. Gáspár, G. Gemme, E. Genin, A. Gennai, A. Giazotto, R. Gouaty, M. Granata, G. M. Guidi, A. Heidmann, H. Heitmann, P. Hello, G. Hemming, P. Jaranowski, R. J. G. Jonker, M. Kasprzack, I. Kowalska, A. Królak, N. Leroy, N. Letendre, T. G. F. Li, M. Lorenzini, V. Loriette, G. Losurdo, E. Majorana, I. Maksimovic, V. Malvezzi, N. Man, M. Mantovani, F. Marchesoni, F. Marion, J. Marque, F. Martelli, A. Masserot, J. Meidam, C. Michel, L. Milano, Y. Minenkov,

M. Mohan, N. Morgado, S. Mosca, B. Mours, L. Naticchioni, I. Neri, F. Nocera, L. Palladino, C. Palomba, F. Paoletti, R. Paoletti, M. Parisi, A. Pasqualetti, R. Passaquieti, D. Passuello, M. Pichot, F. Piergiovanni, L. Pinard, R. Poggiani, G. A. Prodi, M. Punturo, P. Puppo, D. S. Rabeling, I. Rácz, P. Rapagnani, V. Re, T. Regimbau, F. Ricci, F. Robinet, A. Rocchi, L. Rolland, R. Romano, Rosiń, D. ska, P. Ruggi, E. Saracco, B. Sassolas, D. Sentenac, L. Sperandio, R. Sturani, B. Swinkels, M. Tacca, L. Taffarello, A. P. M. ter Braack, A. Toncelli, M. Tonelli, O. Torre, E. Tournefier, F. Travasso, G. Vajente, J. F. J. van den Brand, C. Van Den Broeck, S. van der Putten, M. Vasuth, M. Vavoulidis, G. Vedovato, D. Verkindt, F. Vetrano, A. Viceré, J.-Y. Vinet, S. Vitale, H. Vocca, R. L. Ward, M. Was, M. Yvert, A. Zadrożny, and J.-P. Zendri. Advanced Virgo Status. In G. Auger, P. Binétruy, and E. Plagnol, editors, *9th LISA Symposium*, volume 467 of *Astronomical Society of the Pacific Conference Series*, page 151, January 2013.

[37] Kentaro Somiya. Detector configuration of KAGRA: The Japanese cryogenic gravitational-wave detector. *Class.Quant.Grav.*, 29:124007, 2012.

[38] V.B. Braginsky, M.L. Gorodetsky, and S.P. Vyatchanin. Thermo-refractive noise in gravitational wave antennae. *Physics Letters A*, 271(56):303 – 307, 2000.

[39] M. Cerdonio, L. Conti, A. Heidmann, and M. Pinard. Thermoelastic effects at low temperatures and quantum limits in displacement measurements. *Phys. Rev. D*, 63:082003, Mar 2001.

[40] M. Evans, S. Ballmer, M. Fejer, P. Fritschel, G. Harry, and G. Ogin. Thermo-optic noise in coated mirrors for high-precision optical measurements. *Phys. Rev. D*, 78:102003, Nov 2008.

[41] V.B. Braginsky, M.L. Gorodetsky, and S.P. Vyatchanin. Thermodynamical fluctuations and photo-thermal shot noise in gravitational wave antennae. *Physics Letters A*, 264(1):1 – 10, 1999.

[42] M. De Rosa, L. Conti, M. Cerdonio, M. Pinard, and F. Marin. Experimental measurement of the dynamic photothermal effect in fabry-perot cavities for gravitational wave detectors. *Phys. Rev. Lett.*, 89:237402, Nov 2002.

[43] Stefan W. Ballmer. Photothermal transfer function of dielectric mirrors for precision measurements. *Phys. Rev. D*, 91:023010, Jan 2015.

[44] A. Perreca, J. Lough, D. Kelley, and S. W. Ballmer. Multidimensional optical trapping of a mirror. *Phys. Rev. D*, 89(12):122002, June 2014.

[45] James Lough. *Optical Spring Stabilization*. PhD thesis, Syracuse University, 2014. Dissertations - ALL. Paper 172.

[46] D. Heinert, K. Craig, H. Grote, S. Hild, H. Lück, R. Nawrodt, A. Simakov, D. V. Vasilyev, D. P. Vyatchanin, S. and H. Wittel. Thermal noise of folding mirrors. *Phys. Rev. D*, 90:042001, Aug 2014.

[47] M. M. Fejer, S. Rowan, G. Cagnoli, D. R. M. Crooks, A. Gretarsson, G. M. Harry, J. Hough, S. D. Penn, P. H. Sneddon, and S. P. Vyatchanin. Thermoelastic dissipation in inhomogeneous media: loss measurements and displacement noise in coated test masses for interferometric gravitational wave detectors. *Phys. Rev. D*, 70:082003, Oct 2004.

[48] David Kelley, James Lough, Fabian Mangaña Sandoval, Antonio Perreca, and Stefan W. Ballmer. Observation of photothermal feedback in a stable dual-carrier optical spring. *Phys. Rev. D*, 92:062003, Sep 2015.

Curriculum Vitae

Title of Dissertation

Angular trapping of a mirror using radiation pressure

Full Name

David B. Kelley

Place and Date of Birth

Poughkeepsie, New York December 3, 1987

Colleges and Universities,	Years attended and degrees
Massachusetts Institute of Technology	2006–2010, B.S.
Syracuse University	2010–2015, Ph.D.

Publications

1. Duncan A Brown, Stanislav Babak, Patrick R Brady, Nelson Christensen, Thomas Cokelaer, Jolien D E Creighton, Stephen Fairhurst, Gabriela Gonzalez, Eirini Messaritaki, B S Sathyaprakash, Peter Shawhan, and Natalia Zotov, *Searching for gravitational waves from binary inspirals with LIGO*, Classical and Quantum Gravity **21** S1625–S1633 (2004)

2. Abbott B et al., *First upper limits from LIGO on gravitational wave bursts*, Phys Rev **D69** 102001 (2004)

3. Abbott B et al., *Analysis of first LIGO science data for stochastic gravitational waves*, Phys Rev **D69** 122004 (2004)

4. Abbott B et al., *Analysis of LIGO data for gravitational waves from binary neutron stars*, Phys Rev **D69** 122001 (2004)

5. Brown Duncan A, *Testing the LIGO inspiral analysis with hardware injections*, Class Quant Grav **21** S797–S800 (2004)

6. Abbott B et al., *Setting upper limits on the strength of periodic gravitational waves using the first science data from the GEO 600 and LIGO detectors*, Phys Rev **D69** 082004 (2004)

7. Abbott B et al., *Detector description and performance for the first coincidence observations between LIGO and GEO*, Nucl Instrum Meth **A517** 154–179 (2004)

Awards and Fellowships

2010 Fellowship??

Major Department

Physics